ANALYSIS AND OPTIMISATION OF WINDOW LAYERS FOR THIN FILM CDTE SOLAR CELLS

Francesco Bittau

A Doctoral Thesis

Submitted in partial fulfilment of the requirements for the award of Doctor of Philosophy, Loughborough University

August 2017

Abstract

The work presented in this thesis focuses on the investigation and improvement of the window stack of layers for thin film CdTe solar cells fabricated in the Center for Renewable Energy Systems Technology (CREST) laboratories. In particular the aim was to change the standard structure including TCO, high resistive transparent (HRT)layer and CdS which is limited by the low transparency of the CdS layer, to a better performing one.

The first result chapter of the thesis describes the study of ZnO HRT layers. ZnO thin films were deposited by radio frequency (RF) magnetron sputtering with different structural, optical and electrical properties which were characterized by X-ray diffraction, electron microscopy, spectrophotometry, Hall Effect method and 4-point probe. ZnO films were then incorporated in CdTe solar cells with the structure: FTO/ZnO/CdS/CdTe/Au back contact and the performance of these devices were compared with the film properties to single out trends and identify optimal film characteristics. By varying the deposition pressure of ZnO films, it was possible to increase their transparency and significantly increase their resistivity. While better transparency positively affected the solar cell current density output and efficiency, the resistivity of ZnO films did not show any clear impact on device efficiency. By increasing the deposition temperature the ZnO film grain size was increased. Increased FF was observed in devices incorporating ZnO layers with bigger grains, although this gain was partially counterbalanced by the Voc degradation, leading to a limited efficiency improvement. Finally the addition of oxygen had the main effect of increasing the resistivity of ZnO films, similarly to what happened with the increase of the sputtering pressure. In this case however, an improvement of FF, Jsc and efficiency was observed, especially at an O_2/Ar ratio of 1%. By simulating the solar cells behaviour with SCAPS-1D, it was found that these performance change can be explained by the

variation of interface properties, precisely the amount of interface defects, rather than by bulk properties.

The study presented in the second result chapter focuses on magnesium-doped zinc oxide (MZO) and the variation of its energy band structure. MZO was initially used as the HRT layer within a solar cell structure: FTO/MZO/CdS/CdTe/Au back contact. Sputtering MZO films with a target containing MgO 11 weight% and ZnO 89 weight% allowed for and increased band gap from 3.3 eV of intrinsic ZnO to 3.65 eV for MZO deposited at room temperature. Increasing the superstrate deposition temperature allowed for a further band gap increase up to 3.95 eV at 400 ℃ due mainly to an conduction band minimum upward shift. It was highlighted the importance to create a positive conduction band offset with the MZO layer conduction band slightly above the CdS conduction band, with an optimum found in this case to be 0.3 eV (efficiency 10.6 %). By creating a positive conduction band offset all the performance parameters (Voc, FF, Jsc, efficiency) significantly increased. One of the reasons for this improvement was found to be a diminished interface recombination due to a more ideal MZO/CdS band alignment. In the second part of this investigation the MZO was used as a replacement for the CdS in a simplified structure: FTO/MZO/CdTe/Au back contact. The concepts used to optimise the performance of these devices also involved tuning the conduction band alignment between MZO/CdTe and efficiencies of 12.5 % were achieved with a flat conduction band offset. The efficiency increase was achieved mainly thanks to a better transparency of the MZO layer and a higher Jsc output, compared to devices using a CdS buffer layer.

The MZO buffers have been tested in combination with different TCOs. Results are presented in the third result chapter and showed that AZO is a good alternative to FTO working effectively in combination with MZO. AZO/MZO bilayer yielded the highest overall efficiency thin film CdTe solar cells (12.6%, compared to 12.5% with FTO). It was found that increasing the IR transparency of the TCOs leads to a potentially higher Jsc. Achieving a better transparency was obtained by using TCOs with high mobility and lower carrier concentration (AZO and ITiO) and also by using a boro-aluminosilicate glass with low iron content. ITiO yielded the best opto-electrical properties among all the TCO materials. Devices incorporating ITiO however, showed lower performance then those

using FTO and AZO. ITO/MZO windows also yielded poor performance. In addition, the ITO films deposited had a high carrier concentration leading to a high NIR absorption by plasma resonance and resulted not ideal for application in thin film CdTe PV.

Keywords: CdTe solar cells, thin film, high resistance layer, transparent conducting oxide, magnesium doped zinc oxide, aluminium doped zinc oxide, titanium doped indium oxide, band alignment, high mobility, sputtering.

Acknowledgements

I would like to thank Dr. Jake Bowers and Prof. Michael Walls for giving me the opportunity to carry out my Ph.D. at the Center for Renewable Energy Systems Technology CREST) of Loughborough University.

I would like to thank the Engineering and Physical Science Research Council (EPSRC) (EP/J017361/1) for financial support under the EPSRC Supergen SuperSolar Hub and the Wolfson School of Mechanical, Electrical and Manufacturing Engineering for the help of the administration and technical assistance.

I would like to thank the members of the Photovoltaic Material and Devices (PV-MAD) group. First and foremost I have been delighted to be part of the "Power Rangers" research team, a team composed of friends. Bianca, Fabiana and Christos thanks for your valuable help, availability, sympathy and for the many work and extra-work hours spent together. Bianca also needs to be thanked for being my personal carer at work reminding me that if I wanted to evaporate gold I should not forget to load the gold in the evaporator. Special thanks to Fabiana for sharing the cigarette breaks with me because one entire cigarette was too much for only one of us. I would like to thank Patrick, my favourite colleague for scientific discussions, for the significant help provided with the correction of this thesis. Alex and Mustafa who helped me with the electrical characterization of samples. Ali for the support on the electron microscopy; Nayia, Sona, Sibel, Lewis, Rachael and Piotr, it was a pleasure sharing the Lab life with you. Kevin thanks for your patience and availability.

The work environment in CREST has been great throughout and for that I must thank also many others colleagues and friends: Farhad thanks for being Farhad; Kenan, George and James, I wish I had let you win more ping pong matches, I am sorry. Michael Bellini and Michael Gona, Elena, Francesco, Philip I am thankful that you have been part of this

great group. I would like to also mention all the RAs and Lecturers for working hard to make CREST a great place to work day by day.

I must thank also the people outside CREST that made my life in Loughborough so great: Matteo, Daniele, Alessandro, Andrea, Sara, Francesco Gneo, Tiziano, Giovanni, Claudia.

A very special thanks to my entire family that I am so proud to be part of. To my grandparents Lamberto, Tea and Paola and their unconditional love; to my aunt Silvia and to Riccardo, Donatella and Matilde who make my time at home very more special. And finally to my parents Maurizio and Giovanna and my little sister Chiara for giving me the strength in everything I do. I have been missing all of you very much here in England.

List of publications

D. Menossi, E. Artegiani, **F. Bittau**, M. Barbato, M. Meneghini, G. Meneghesso, J.W. Bowers, J.M. Walls, F. Piccinelli, A. Romeo, "High Efficiency CdTe Solar Cells by Low Temperature Deposition with MgZnO HRT Layer" in 33rd European Photovoltaic Solar Energy Conference and Exhibition, 2017, pp. 1027–1030. DOI: 10.4229/EUPVSEC20172017-3BO.9.5

P. M. Kaminsky, S. Yilmaz, A. Abbas, **F.Bittau**, J. W. Bowers, R. C. Greenhalgh, J. M. Walls, "Blistering of magnetron sputtered thin film CdTe devices" in 2017 44th IEEE Photovoltaics Specialist Conference (PVSC)

F. Bittau, E. Artegiani, A. Abbas, D. Menossi, A. Romeo, J. W. Bowers, J. M. Walls, "Magnesium-doped zinc oxide as a high resistance transparent layer for thin film CdS/CdTe solar cells" in 2017 44th IEEE Photovoltaics Specialist Conference (PVSC)

F. Bittau, A. Abbas, K. L. Barth, J. W. Bowers, and J. M. Walls, "The effect of temperature on resistive ZnO layers and the performance of thin film CdTe solar cells" Thin Solid Films, vol. 633, pp. 92–96, Jul. 2017. DOI: 10.1016/j.tsf.2016.10.068

P. M. Kaminski, A. Abbas, C. Chen, S. Yilmaz, **F. Bittau**, J. W. Bowers, and J. M. Walls, "Internal strain analysis of CdTe thin films deposited by pulsed DC magnetron sputtering," in 2015 IEEE 42nd Photovoltaic Specialist Conference (PVSC), 2015, pp. 1–6. DOI: 10.1109/PVSC.2015.7356093

Contents

Chapter 1

Introduction

The introduction chapter of this thesis is divided into three sections. The first section emphasises the huge potential of converting sun light into electrical power to address the increasing needs of humanity for energy, and aims to provide some information on the solar resource. To be able to exploit the potential of solar power, the production of electricity from the sun must be economically competitive compared to the other available energy sources. The second section addresses the economic aspects of photovoltaic (PV) deployment. Then a focus is provided on the potential for CdTe thin film PV technology to provide cost-competitive electricity. Finally emphasis is placed on the strong impact that research can have on achieving cost reductions. The third and final section provides a fundamental description of semiconductors and the use of p-n junctions to extract power from sunlight.

1.1 The solar resource

The sun radiates an electromagnetic spectrum very similar to a black body at a temperature of around 5762 K. This translates to a mean solar irradiance of 1360 Wm^{-2} at the top of the atmosphere (accounting for the diurnal cycle). Atmospheric gases and particles absorb and scatter this radiation leaving an average global annual irradiance of 200 Wm^{-2}. This provides three orders of magnitude more power than the current global energy demand [1]. Solar is by far the most abundant form of energy available on our planet compared to other renewable energy sources, and also other sources such as nu-

clear power and fossil fuels (Fig. 1.1). It is in our global interest to fully exploit the solar resource.

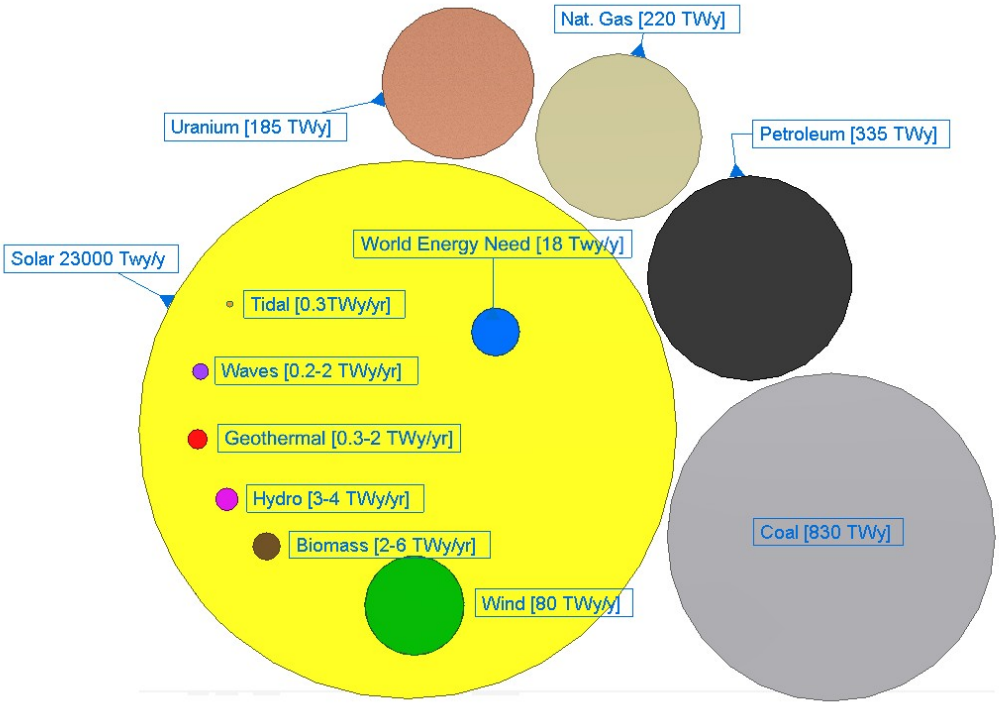

Figure 1.1: A graphical representation of the estimated global energy potential for the main renewable and non-renewable energy sources. The area of the each circle is proportional to the energy availability in one year for renewable energy sources, while for fossil fuels and nuclear the area is the estimated energy corresponding to the finite material reserves [2].

When the sun is at its zenith, the radiation travels the shortest distance within the atmosphere to reach the earth's surface. With the sun at high solar zenith angles, the effect of the atmosphere further attenuates the radiation, decreasing the number of photons reaching the ground. The Air Mass (AM) is the measure of the ratio between the actual path length through the atmosphere and the shortest path possible. AM1 refers to the sun directly overhead (Zenith) while AM1.5G (48.19° zenith angle) is considered by the American Society for Testing and Material as the standard sun electromagnetic spectra representative of mid-latitudes. The AM1.5G spectrum is the standard used to measure the performance solar cells [3] is compared in Fig. 1.2 to the AM0 spectrum representative of the solar radiation at the edge the earth's atmosphere.

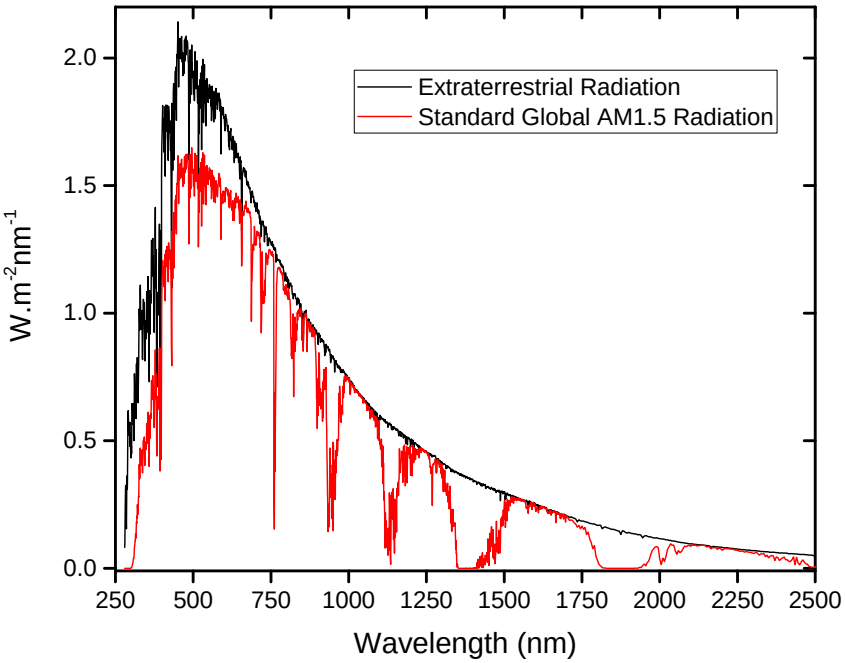

Figure 1.2: Extra-terrestrial radiation spectrum and AM1.5G global radiation spectrum provided by the American Society for Testing and Materials (ASTM)[4].

1.2 Techno-economical aspects of PV

The levelised cost of electricity (LCOE) is an important parameter used by investors and policy makers to assess the economic feasibility of power plants. It consists of the ratio between the total costs required to build and operate the power plant and the total energy output over its lifetime. The costs taken into account to create and operate a solar power plant are several:

- costs of the module;
- costs of the inverter and other electrical components;
- costs of the design and the management;
- costs of the installation;
- costs of the operation and maintenance;
- costs of the land;

- costs of the batteries.

The improvement of module efficiency, if achieved with a cost effective processes, not only enhances the energy yield per module area, but decreases some of the other operational costs. This makes the research to increase solar cell efficiency one of the main drivers for a lower LCOE. The photovoltaic (PV) market is currently dominated by silicon based solar modules. Silicon technologies account for approximately 94% of the annual production of modules by peak power (GWp), 70% of which is multi-crystalline Silicon (multi-Si) and the reminder is mono-crystalline Silicon (mono-Si) [5]. Mono-Si and multi-Si technologies are highly performing and mature technologies having been heavily developed in past decades. These characteristics of silicon technology combined with an aggressive policy in China where PV manufacturers are allegedly subsidised, are leading to reduced costs and rapidly increasing competitiveness of PV LCOE with conventional energy resources. These reduced costs have been brought about through heavy investment and improvement in the fabrication and manufacturing processes. However, limitations of these technologies do exist. Mono-crystalline silicon solar cells are made using expensive high purity single crystals of silicon. Thick wafers (150 to 300 μm) are needed to absorb all the energy due to the indirect band gap of silicon. Multi-crystalline silicon solar cells require lower cost processing than mono-crystalline however, their efficiency is relatively poor due to the reduced quality of the material. Thin film solar cells (mainly CdTe and CIGS) have the potential to lower the fabrication costs of high efficient modules. Thin film CdTe solar modules are competitive on the utility-scale LCOE ($\approx$4\$/kWh [6]) compared to Si-based modules as well as conventional energy sources. First Solar Inc. has successfully industrialised this technology and it is leading the way for high-efficiency, low-cost modules. The manufacturing process adopted by First Solar is simpler, faster and has the shortest energy payback time for all PV technologies [5]. CdTe is a direct band gap material and 100 times less material is required to absorb all the light compared to crystalline silicon. These characteristics make CdTe thin film technology less capital intensive than crystalline silicon technologies. Utility scale CdTe solar plants are also demonstrating, especially in warmer climates, better field performance because less sensitive to high temperatures (due to a smaller temperature coefficienct) and high humidity conditions [7]. A key factor for further improvement of this technology is laboratory research to improve

conversion efficiency and the transfer of these improvements to commercial and module scale manufacturing.

1.3 Solar cell basics

1.3.1 Semiconductors

Solar cells have the function of converting electromagnetic radiation from the sun into electrical power. Multiple technologies and concepts are being developed to convert sunlight into electricity however, this thesis focuses on thin film CdTe solar cells. All semiconductor-based solar cells follow similar physical mechanisms which will be summarised in the following sections.

1.3.2 The energy band gap and the optical properties of a semiconductor

Every semiconductor material has a characteristic set of electron energy levels which form distinct energy bands. The valence band (E_V) of a semiconductor corresponds to the highest range of electron energies at which electrons are present at 0K, while the conduction band (E_C) is defined as the lowest range of possible electron energies which is empty. In a semiconductor an energetic gap occurs between the valence and conduction band in which no electronic states are populated by free carriers (electrons or holes); this is called the energy band gap (E_g). The energy band gap is crucial in the choice of a semiconductor for photovoltaic purposes because it determines the energy of photons that can be absorbed. Only photons with an energy equal to or greater than E_g are absorbed, and their energy imparted to electrons that as a result can "cross" the band gap to reach the conduction band energy state. This creates an electron-hole pair since the promoted electrons leave an empty energy level in the valence band, called the hole. The optimal E_g for a photovoltaic absorber for a single junction solar cell can be estimated using the Shockley-Queisser limit [8]. The limit considers the most basic thermodynamic losses that are unavoidable in a photovoltaic device for the calculation of the efficiency with which a solar cell extracts energy from the incident radiation. The limiting factors taken into

account are:

(1) the black body radiation that any body which is not at absolute zero (0K) emits and can not be captured by the cell;

(2) the radiative recombination which occurs when an electron that encounters a hole and recombines resulting in the emission of a photon. This is the opposite phenomena of the creation of an electron hole-pair by an incident photon and it is inevitable;

(3) the spectrum losses, which consider the energy loss of photons which have lower energy than E_g and cannot be absorbed as well as the energy loss of photons with energy superior than E_g; in fact this excess energy is lost as thermal energy.

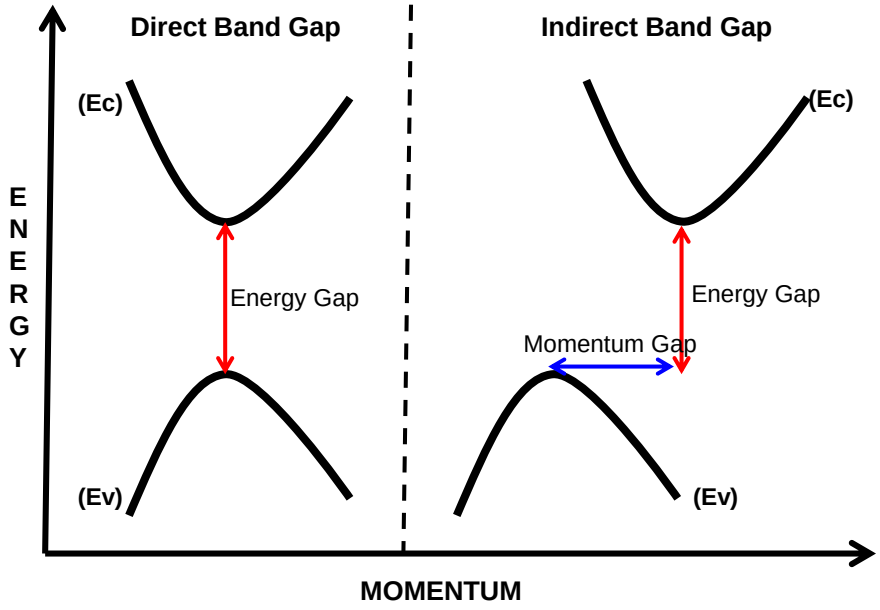

Figure 1.3: The graph visually simplifies the concept of direct and indirect band gap. On the left side of the graph, the conduction band minimum and the valence band maximum of an direct band gap semiconductor, occurring at the same momentum level. On the right-hand side the conduction band minimum and valence band maximum of an indirect band gap semiconductor, occurring at a different momentum level. In this second case momentum gap and energy gap need to be simultaneously filled by a phonon and a photon respectively in order for the electron to be promoted to the conduction band.

The optimal band gap for the absorber semiconductor layer of a solar cell for a standard

AM1.5G spectrum is between 1.3 eV and 1.4 eV [9]. For a material with direct band gap, the conduction band minimum and the valence band maximum occur at the same wave number value k whereas they do not for an indirect band gap material they. This means that in the second case, to excite an electron a source of momentum (phonon) is required in combination with a photon (Fig. 1.3). In practice, this means that for materials with a direct band gap it is statistically more likely to absorb a photon than an indirect band gap semiconductors and, as a consequence, light travels shorter distances through the material before being completely absorbed. A CdTe (direct E_g) absorber is typically a few μm thick whilst a silicon (indirect E_g) absorber thickness is usually hundreds of μm.

1.3.3 The energy band structure of a semiconductor

In order to reproduce the energy band structure of a semiconductor, other fundamental parameters are required. The Fermi level (E_F) in a semiconductor is defined as an energy level at which states have a 50% probability of being filled with an electron and is calculated using the Fermi-Dirac distribution.

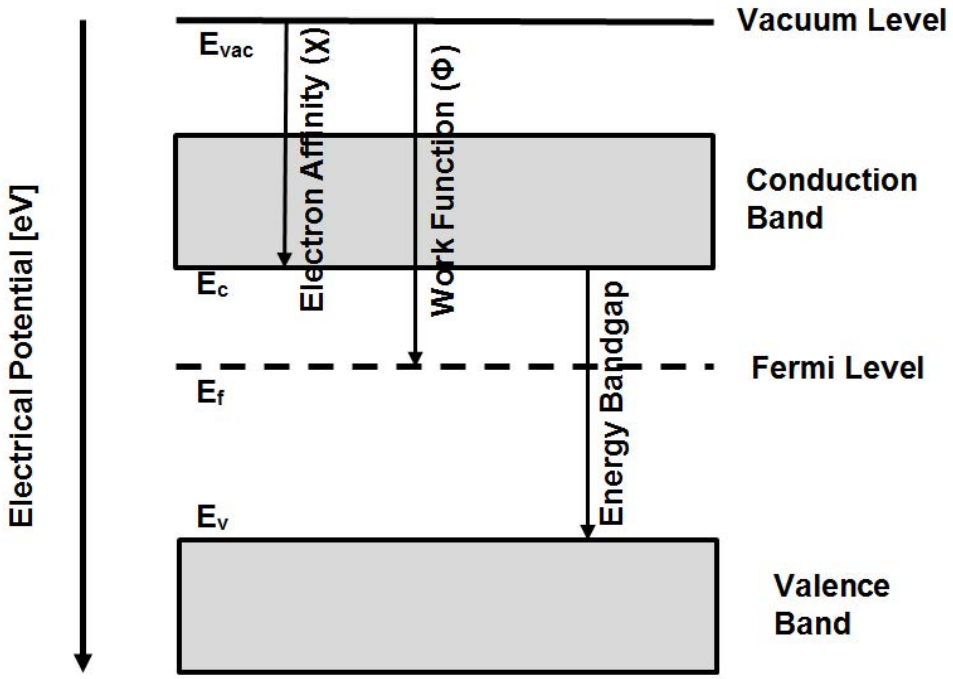

Figure 1.4: The simplified energy band structure diagram defining the vacuum level (Evac), the conduction band (Ec), the Fermi level (E_f), the valence band (Ev), the band gap (Eg), the work function (ϕ) and the electron affinity (χ) of a semiconductor.

The vacuum level (E_{vac}) is the energy level at which an electron is considered free, outside of any material. Knowing these parameters makes it possible to form the energy band structure of a semiconductor as illustrated in Figure 1.4. From the vacuum level it is possible to define the electron affinity, χ, as the minimum energy required to extract an electron from a semiconductor conduction band to the vacuum level and the work function ϕ as the average energy required to extract an electron from the semiconductor to vacuum, i.e. from its Fermi level. Taking into account the alignment of the transport levels of different semiconductors and the position of the Fermi level throughout the device, it is possible to optimise the design of a CdTe solar cell. This topic will be addressed in Chapter 2.

1.3.4 The electrical properties of a semiconductor

The electrical properties of a semiconductor depend on its composition and morphology, and they are strongly correlated with its energy band structure. The ability of a material to conduct a current can be expressed by the electrical conductivity σ of the material or by its reciprocal, the electrical resistivity ρ. For convenience resistivity will be used in this thesis. In a semiconductor the resistivity is inversely proportional to the carrier concentration n, the elementary charge e, and carrier mobility μ as shown in Equation 1.1.

$$\rho = 1/ne\mu \tag{1.1}$$

While the elementary charge is a constant, the carrier concentration and the mobility are properties of a semiconductor that can be altered. For example, impurities, or dopants, can be added to the material to enhance the number of free carriers. These impurities can be either shallow donors or acceptors depending on the type of conductivity required. Shallow means that the electronic state of the dopant is relatively close in energy to the conduction (donor) or valence (acceptor) band (Figure 1.5). A donor atom becomes positively charged when it releases an electron to the conduction band; conversely an acceptor atom is charged negatively when it accepts an electron leaving a hole in the valence band. The electronic state relative to a donor or to an acceptor must be shallow

enough such that the thermal energy kT at room temperature provides enough energy (meV) to easily free the carrier to the conduction or valence band [10]. Intrinsic defects in a material not grown perfectly stoichiometric can add shallow states also without adding any extrinsic dopant.

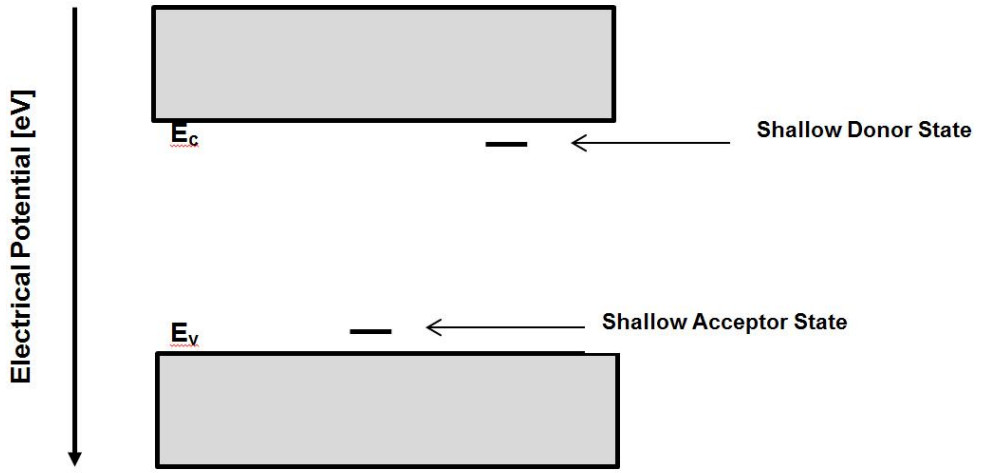

Figure 1.5: An energy band diagram showing shallow energy state positions in relation to the valence band maxima and conduction band minima of a semiconductor.

In thermodynamic equilibrium, the relative concentration of carriers is described by the Fermi level. The relationship between carrier concentration and Fermi level is given by equation 1.2

$$n = N_C \exp(\frac{E_F - E_C}{kT}); p = N_V \exp(\frac{E_V - E_F}{kT}) \tag{1.2}$$

Where n is the electron concentration, p the hole concentration, N_C and N_V are the density of states for the conduction and valence band respectively. In an intrinsic semiconductor, each electron that leaves the valence band generates a hole. Thus the concentration of electrons in the conduction band is equal to that of holes in the valence band. As a consequence the Fermi level for an intrinsic semiconductor lies in the mid-gap. Doping the material has the effect of shifting the Fermi level towards the conduction or valence band, depending on the type of dopant. For a semiconductor doped with shallow donors, the Fermi level will shift closer to the conduction band. In this case, the semiconductor has a n-type conductivity. The opposite occurs for a p-type semiconductor that is doped with shallow acceptors.

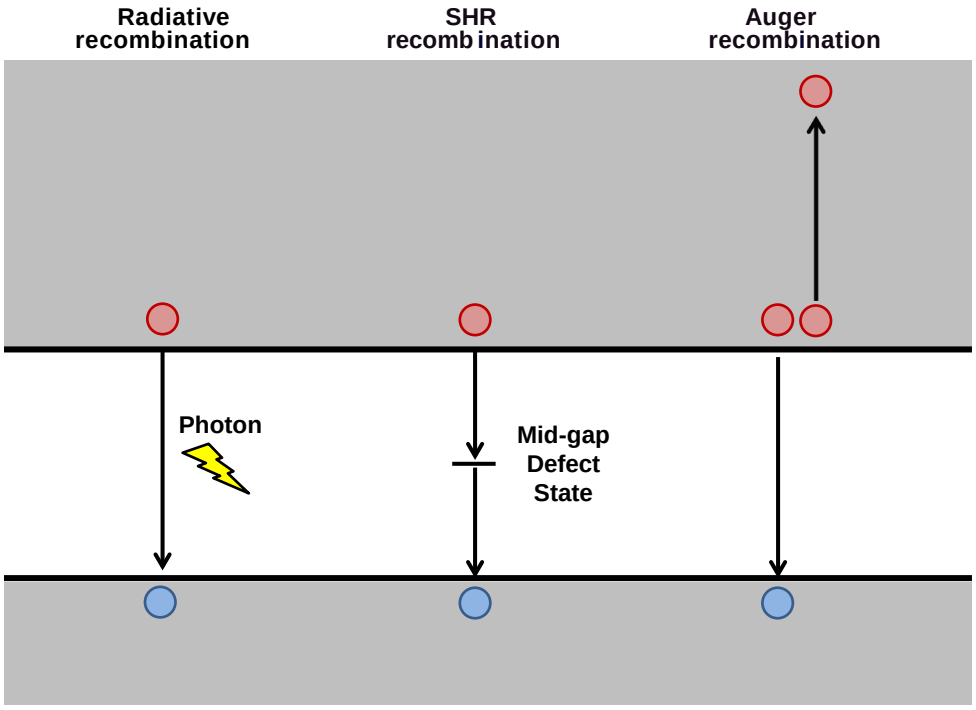

Figure 1.6: A energy band diagram showing simplified radiative, SHR and Auger recombination processes.

1.3.5 Recombination processes

When light shines on a semiconductor it generates electron-hole pairs (section 1.3.2). To generate power, a photovoltaic device must extract the light-generated free carriers to an external circuit. However, electrons (in p-type materials) and holes (in n-type materials) are meta-stable and they can recombine before extraction. An electron (hole) in a p-doped (n-doped) material is a minority carrier and will have the opportunity to recombine with a large number of holes (electrons) from the valence band (conduction band). There are several different possible recombination processes discussed in the following sections [11].

1.3.5.1 Bulk recombination

Radiative recombination is the unavoidable recombination mechanism that causes an electron in the conduction band to recombine with a hole in the valence band, emitting a photon (figure 1.6). It is the reverse mechanism of the photo-generation of electron-hole pairs. The photon emitted has an energy similar to the band gap but has a low probability of re-absorption. Radiative recombination is more frequent in direct band gap semicon-

ductors such as CdTe and CIGS. While in indirect band gap semiconductors, it is a less likely phenomenon because free carriers require simultaneously a free state and momentum source (section 1.3.2). Shockley-Read-Hall (SHR) recombination is a non-radiative, two-step process that involves defect states lying energetically within the energy band gap of a semiconductor. The crystal lattice of a semiconductor, particularly if polycrystalline, often contains detrimental impurities and defects. These can introduce localized states close to the mid-gap (figure 1.6). The two step mechanism involves an electron (or hole) recombining via one of these levels, firstly moving to a mid-gap level and secondly recombining with a hole in the valence band. Auger recombination involves a radiative recombination process and a third carrier. The energy radiated by the recombination process is given to a third carrier which is excited to a higher energy level (figure 1.6). Normally the energy gained by the third carrier is lost through thermal vibrations. This mechanism becomes significant only at high carrier concentrations, either by doping or light excitation.

1.3.5.2 Surface and interface recombination

The recombination mechanisms described so far are characteristic of the material bulk. Surface recombination involves the surface of semiconductors, where the crystal structure is disrupted abruptly. Surfaces are typically rich in dangling bonds and create defects which cause high localised recombination rates. In order to decrease the amount of surface dangling bonds the surface can be passivated either by the deposition of a passivating layer or by a passivation surface treatment [12]. Similarly, the interface between two different semiconductors with a lattice miss-match generates a high concentration of recombination states. The interface recombination of CdTe solar cells will be discussed in chapter 3, chapter 4 and chapter 5 and is an important aspect of thin film solar cell technology.

1.3.6 The p-n junction

Solar cells require a built-in electrical field to produce power. Solar cells based on semiconductors take advantage of p-n junctions that form when a p-type semiconductor and an n-type semiconductor are joined together.

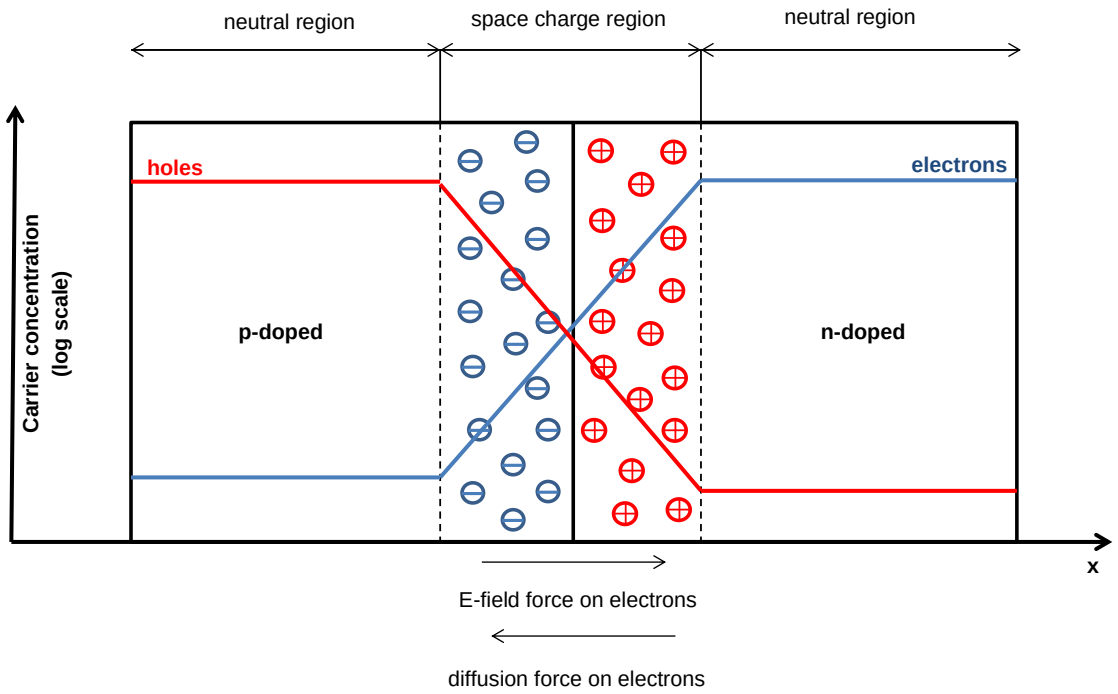

Figure 1.7: Schematic diagram showing a simplified junction between equally doped p-doped semiconductor and an n-type semiconductor. The small circles represent negatively (blue) charged and positively (red) charged ions. The red and blue lines represent the concentration of holes and electrons in the diode.

When this occurs, the electrons (holes) in excess of the n-type (p-type) material diffuse to the other side of the junction to balance out the concentration gradient. The same occurs to holes diffusing from the p-type side accross the junction. The diffusion of carriers from one material to the other leaves positively charged ions in the n-type semiconductor, close to the interface, and negative charged ions on the p-type side of the junction. As a consequence a charged region, depleted of free carriers, forms at the interface, having positive charge on the n-type side and negative charge on the p-type side. This dipole forms an electric field at the interface that opposes the diffusion current and induces a drift current. In equilibrium, i.e. in the dark at constant temperature and bias, drift and diffusion current balance out and the net current is zero. These are the basic principles of a diode. The high resistivity of the depletion region, due to the limited number of carriers, creates a barrier to current flow. If reverse biased (positive voltage applied to the n-type side and negative to p-type side) this barrier increases, the depletion region widens and no current can flow through the diode. However, if forward biased, the applied electric

field opposes the electric field created by the p-n junction which diminishes the barrier to diffusion current. The behavior of a junction is summarized in this equation [13]:

$$J = J_0(\exp(\frac{qV}{kT}) - 1) \tag{1.3}$$

Where J is the current density (mA/cm^2), J_0 is the dark saturation current density, V is the voltage applied across the terminals of the diode, q the electron charge and kT is the thermal energy of the semiconductor. When an electron-hole pair is generated, electrons and holes drift in opposite directions by the electric field and they separate. The spatial separation of electrons and holes prevents recombination and adds to the built-in bias. Equation (1.4) summarizes the behavior of a solar cell under illumination conditions:

$$J = J_0(\exp(\frac{qV}{kT}) - 1) - J_L \tag{1.4}$$

Where J_L is the illumination-induced current. There are multiple choices among p-doped and n-doped semiconductors to obtain a p-n junction. In the case of CdTe based solar cells the CdTe p-type active layer is usually coupled with a n-type CdS layer. Chapter 2 provides an overview of CdTe thin film solar cells technology and the research challenges which need to be addressed.

Chapter 2

Thin Film CdTe Solar Cells

Cadmium telluride is a $II^B - VI^A$ compound semiconductor with a direct band gap of approximately 1.45 eV, which is nearly optimum for photo-conversion of the solar spectrum. It has a high absorption coefficient α > 5 x 10^5 cm^{-1} that makes it possible to absorb almost all available photons within a 2 μm thick layer [14]. CdTe thin films for PV applications are fabricated in the zinc blende structure and can be formed stoichiometrically , Cd rich or Te rich depending on the deposition conditions [14]. High efficiency CdTe solar cells, to date, have the same superstrate configuration (Fig. 2.1), which was first proposed by Bonnet and Rabenhorst in 1972 [15]. The thin film solar cell heterostructure involves the deposition of multiple n-type window layers onto a superstrate, usually glass. The superstratess are initially coated with a transparent conducting oxide (TCO) that forms the front contact of the solar cell. The TCO is often followed by a high resistive transparent (HRT) layer that has been found to increase device efficiency. A more detailed description of the role of HRT layers is given in the section 2.2. A thin film of CdS often completes the n-type side of the device and interfaces with the CdTe. The CdS layer and the CdTe layer are regarded as being the primary p-n junction. The cell is completed with a back contact that provides the second electrical terminal of the device. Best efficiency obtained with laboratory scale cells by this technology is 22.1 %, achieved by First Solar, an American PV modules manufacturer and energy retailer. The high efficiency has been allegedly achieved through different steps. By replacing the CdS layer with a more transparent buffer layer, reducing then the optical losses at the front of the solar cell. By including Se in the CdTe absorber to form a CdSeTe ternary compound. This has

the effect of reducing the absorber band gap and extending its photo-active range in the infra-red wavelength range. By optimising the back contact by using a Cu-doped ZnTe layer deposited at the back of the absorber layer, to decrease the contact resistance and limit performance degradation due to Cu diffusion within the solar cell. By comparing the performance parameters of the best performing thin film CdTe solar cells with the ideal limits calculated using the Shockley-Queisser limit, it appears that it is Voc the parameter mostly far off its ideal limit (876 mV VS around 1156 mV). The FF is roughly 10% inferior than its limit (90%). This seem to mainly related to the low Voc. On the other hand CdTe has greater than 90% utilisation in Jsc, which is higher than that of Silicon and CIGS. To compare CdTe with other highly efficienct technologies, GaAs has the highest utilisation overall of both FF and Voc. Also silicon and CIGS based solar cells have better utilisation of Voc and FF than CdTe. The CdTe limitations seem to fall into two main categories. One is related to the low free carrier lifetime and low carrier density of the the CdTe bulk. The second limitation is related to the non-ohmic back contact due to the high CdTe electron affinity and/or by the pinning of the CdTe surface caused by surface defects. The CdTe solar cells substrate structure Glass/Metal/CdTe/CdS/TCO has yielded lower efficiencies than the conventional superstrate structure. This is due to a poor CdS/CdTe junction and non-ohmic contact with CdTe [14]. This is primarily caused by the thermal and chemical instability of the back contact, commonly including Cu, which easily diffuses to the CdS/CdTe junction during film growth and the $CdCl_2$ activation treatment.

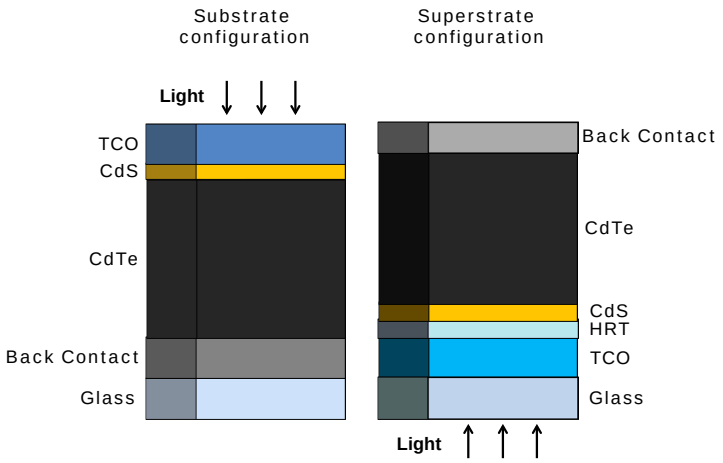

Figure 2.1: Typical substrate and superstrate configurations of a thin film CdTe solar cell.

The $CdCl_2$ treatment consists of an annealing step undertaken in the presence of chlorine that "activates" the solar cell and boosts its efficiency. The following sections of this chapter will provide a description of the role of each film included in a CdTe solar cell.

2.1 TCOs

Thin film technologies make use of TCO contacts either at the front or back of the solar cell [16, 17, 18, 19, 20]. Transparent conductive oxides are utilized in other fields such as flat panel displays (LCDs), plasma display panels, electronic paper displays, light-emitting diodes (LEDs) [21] and touch screen panels [22]. The basic requirements for an optimum TCO for thin film photovoltaic applications are good opto-electrical properties; the semiconductor needs to be very transparent in the visible and near infrared (NIR) wavelength range where the solar spectrum is more intense. This can be obtained if the semiconductor band gap $E_g > 3$ eV [23]. A resistivity below $10^{-3}\ \Omega \cdot cm$ is also required to achieve a conductive but relatively thin TCO [23]. One method to increase the conductivity of an n-type TCO is to dope it with shallow donors to increase the free carrier concentration. This must be limited, however, since increased doping levels ($\gg 10^{20}$ cm^{-3}) cause the plasma wavelength λ_p to shift towards the NIR-VIS spectrum range.

The resonance of electrons increases light absorption at λ_p and light reflection above λ_p. λ_p can be calculated by:

$$\lambda_p = 2\pi c\sqrt{\frac{\varepsilon_\infty \varepsilon_0 m_e^*}{Nq^2}} \tag{2.1}$$

Where ε_∞ and ε_0 are the absolute permittivity and relative permittivity of the material respectively, m_e^* is the electron effective mass, N is the free carrier density and q is the electron charge. The optimal carrier concentration is usually in the range $10^{20} cm^{-3}$ - $10^{21} cm^{-3}$ [23]. High mobility TCOs can provide low resistivity ($\approx 10^{-4}$ Ωcm) with a reduced doping concentration, while maintaining high transmission in the NIR range. Thermal and chemical stability are other key characteristics that a TCO requires. In fact, the TCO layer must withstand several thermal and chemical treatments during which it should maintain good opto-electrical properties [24].

2.2 HRT layer

The CdS layer in a CdS/CdTe solar cell absorbs part of the solar spectrum below ≈500 nm [14, 18]. Thinning the CdS layer has the effect of increasing the number of photons reaching the CdTe absorber. However, this process has detrimental effects on the open circuit voltage and the fill factor of the device. HRTs, which are large band gap ($E_g > 3$ eV) semiconductors, are used to prevent V_{OC} and FF degradation due to the thinning of CdS while allowing a higher current density output and higher efficiency [18]. The physical mechanisms related to the beneficial effect of an HRT are still not fully understood and its use has been prevalently empirical. The most common hypothesis considers the HRT as a barrier for shunts through the device. The hypothesis is that when thinning the CdS layer (below 100 nm) there is a larger portion of the CdS film area which is not uniform. This is due to the difficulty to deposit a very thin and at the same time uniform film. This can lead to localised areas of the film that are interrupted (a pinhole) or very thin, creating weak diodes and increasing the saturation current of the device. Following this hypothesis the HRT acts as a barrier for shunts between the CdTe and the TCO mitigating the effect of CdS non-uniformities [25]. If pinholes are the true cause of performance degradation, the problem could be mitigated if the CdS layer is made very thin but

uniform. However, it has been demonstrated by Kephart et al that, even in the presence of a thin but homogeneous CdS layer, the V_{OC} and the FF degrade when the film thickness is below 100nm [26]. This suggests that the "pinhole hypothesis" might not be the only explanation for this mechanism. In the same work Kephart suggests that the HRT's effect on band alignment can explain its positive effect on device performance. It may overcome any non-ideal TCO/CdS band alignement. Assuming that the TCO's work function is higher than the electron affinity of the CdS, a Schottky barrier can form causing the carrier depletion in the part of the CdS adjacent to the TCO. A barrier at the interface between the Fluorine-doped Tin Oxide(FTO) and the CdS was measured by Fritsche [27]. Following this hypothesis, as the CdS is made thinner, the CdS/CdTe junction moves into the depletion region because the TCO/CdS barrier causing a loss in built-in potential and consequently a drop in V_{OC}. Similarly Tingliang and colleagues [28] analysed the band alignment of window layers of a CdTe solar cell with a ITO/ZnO/CdS/CdTe structure. Using X-Ray photoelectron spectroscopy (XPS) and Ultraviolet photoelectron spectroscopy (UPS) analysis they concluded that the introduction of the ZnO HRT serves to decrease the barrier energy between the CdS and the ITO and consequently to facilitate the transfer of electrons between the two. There are studies highlighting a rectifying behaviour due to a ITO/CdS barrier building up after a thermal treatment similar to the $CdCl_2$ activation treatment [18, 29]. However, more research needs to be done to fully understand the role of HRT layers.

2.3 The CdS/CdTe p-n junction

The primary p-n junction occurs between the p-type CdTe absorber and the n-type CdS buffer layer despite the large lattice mismatch between the two [30]. CdS is also widely used in CIGS solar cells with the same n-type role. The deposition of pinhole free CdS is critical in achieving high solar cell efficiencies [30]. The CdS thickness is normally kept below 300 nm to ensure uniform coverage and to limit light absorption. CdS deposition techniques range from vapour deposition [29], to chemical-bath deposition (CBD) [31, 32], close space sublimation (CSS)[26] and magnetron sputtering [33]. The CdS can be subject to a post-deposition heat-treatment at temperatures above 400 °C. This step has the

effect of enhancing crystallization of the film and thickness homogeneity [24, 34]. The subsequent deposition of CdTe can be performed by a wide range of techniques: CSS, vapour transport deposition, magnetron sputtering, electro-deposition, ultrasonic spray pyrolisis and screen print [14]. Grain size and density are important characteristics to be monitored. Small grains result in films with high grain boundary density. Grain boundaries are thought to act as a traps for minority carriers and, if charged, may have a distorting effect on the free carrier path. The CdTe thickness is typically from 1 to 10 μm and deposition temperatures are usually maintained high, above 400 °C [35]. A post-deposition $CdCl_2$ treatment is required to activate the solar cell. It involves annealing at temperatures around 400 °C along with the diffusion of chlorine into the CdTe layer. The $CdCl_2$ can be deposited on the CdTe layer by vapour deposition, sublimation or by wet treatment in a solution [36, 37]. Recent studies highlight there may be two different processes occurring in parallel during the $CdCl_2$ treatment. The temperature raise during the thermal annealing step is mainly assissting a reduction of the recombination in the near-interface region, causing Jsc and fill factor to increase. The key role of chlorine seems related to the passivation of CdTe grain boundaries with consequent increase of the minority carrier lifetime, and Voc gain [38, 39, 40, 41]. $CdCl_2$ seem so effective because it dissociates Cl in the ideal temperature range for annealing. The treatment re-crystallizes the CdTe and the CdS layers helping grain growth, reducing structural defects and passivating grain boundaries. The re-organization of the CdTe structure that results also in higher acceptor concentration [39, 40, 41]. The key role of chlorine is to increase V_{oc} through passivation of the CdTe grain boundaries by increasing the doping concentration [38]. A critical aspect of the $CdCl_2$ annealing is intermixing. Ternary compounds can form at the CdS/CdTe interface as a result of inter-diffusion between CdTe and CdS: a sulphur rich layer of $CdTe_yS_{1-y}$ and a Te-rich layer of CdS_yTe_{1-y}. The formation of these ternary compounds is believed to reduce the concentration of recombination centres at the interface and to reduce CdS thickness coupled with a potential optical gain in the blue spectrum range [42].

2.4 The back contact

The formation of a low-resistance ohmic back contact with the CdTe layer is important. CdTe is a p-type semiconductor with a high electron affinity ($\chi = 4.5$ eV) and a band gap of 1.45 eV. The contact barrier ϕ_b at the CdTe/metal interface is given by the difference between the CdTe valence band edge and the Fermi energy in the metal [43]:

$$\phi_b = \frac{E_g}{q} + \chi - \phi_m \tag{2.2}$$

Where E_g is the band gap, χ is the CdTe electron affinity and ϕ_m is the work function of the metal forming the back contact. If present, a barrier at this interface can impede the hole transport to the metal that can result in a "rollover" effect on the current-voltage characteristic of a CdTe solar cell (Fig. 2.2) [43, 44]. A metal with a high work function (5.7 eV or greater [45]) would theoretically provide an ohmic contact; however no commercially available metals have a high enough ϕ_m and as a result the metal/CdTe junction creates a Schottky barrier [46, 47].

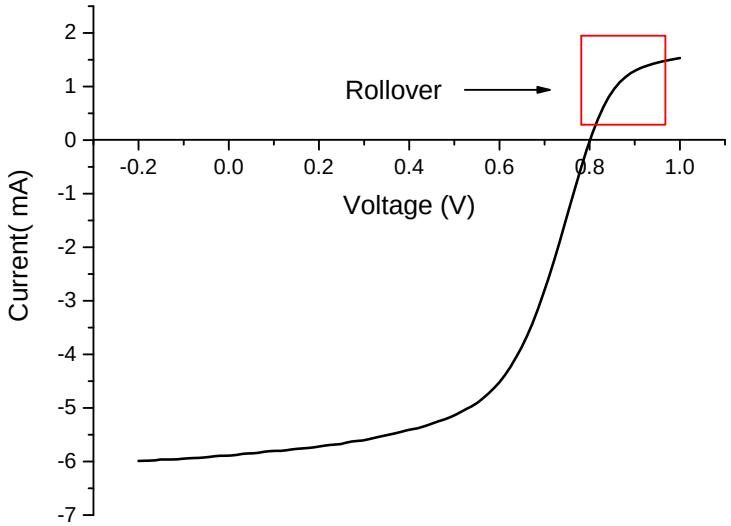

Figure 2.2: I-V curve of a CdTe solar cell having a barrier at the CdTe/back contact junction. The barrier causes the rollover of the IV characteristic highlighted in the graph second quadrant.

The contact resistance can be decreased by selectively etching the CdTe surface and leaving a Te-rich surface. This step is then followed by the deposition of a Cu [46] or Cu_xTe [48] layer, which increases the acceptor concentration in the CdTe layer through

the Cd susbtitution by Cu dopants [49, 50]. The result is that the depletion region of the metal/CdTe junction, which extends almost exclusively in the CdTe layer, narrows. If the depletion region reaches tunneling length the contact becomes quasi-ohmic reducing its resistance [51]. It is challenging to keep the performance stable in this type of back contact. The Cu+ ions have high diffusivity and tend to migrate during device operation from the back contact region towards the front of the device. While a controlled diffusion of Cu in the CdTe can be beneficial for performance, over-diffusion of the metal towards the front of the cell is believed to cause shunting and gradually degrades the solar cell efficiency [45, 48, 51]. Recently it has been demonstrated the deposition of an intermediate semiconductor between CdTe and the metal contact which aids the hole collection. Such semiconductors should have a higher conduction band compared to the CdTe layer, the valence band aligned to the CdTe and requires a p-type doping > 10^{20} cm^{-3} to provide an effective tunnel junction to the metal layer, example of this using Cu doped ZnTe have been published (ex. ZnTe [52, 53]].

2.5 The energy band structure of a CdTe solar cell

Each material within a thin film solar cell has a characteristic energy band structure and doping. Furthermore these characteristics may vary between the bulk and the surface of the material. The energy band diagram can aid the understanding of the carrier transport, the carrier recombination and the Fermi level distribution of a thin film heterostructure solar cell [54]. In figure 2.3 we show a representative energy band diagram of a CdTe/CdS/TCO heterostructure solar cell. The back contact is omitted for simplicity.

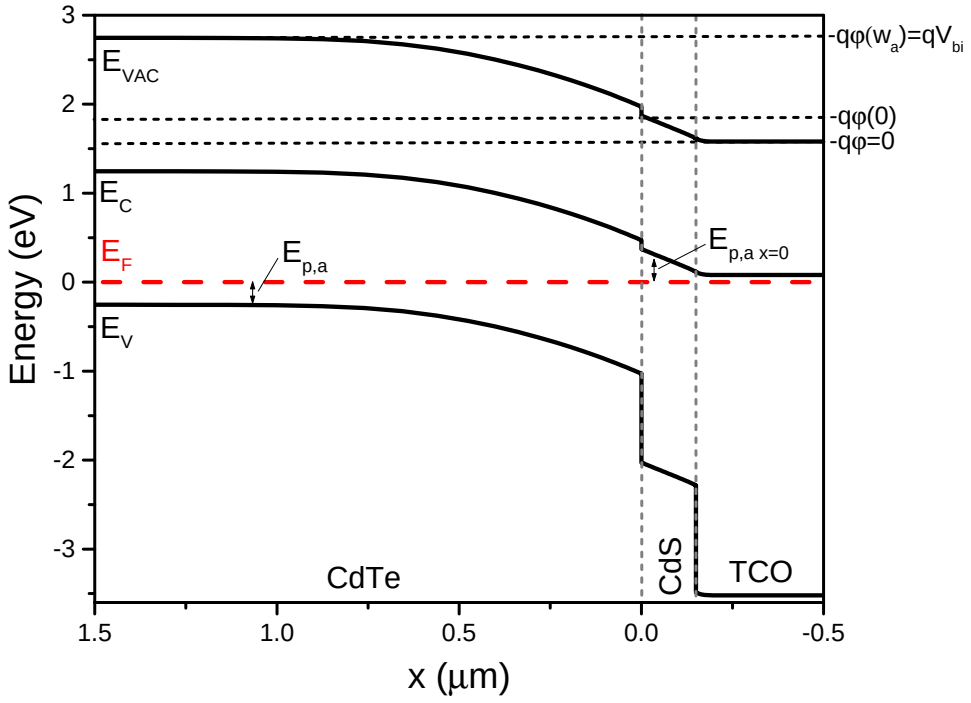

Figure 2.3: Example of an energy band diagram for a thin film CdTe solar cell

The quantity $E_{p,a}$ is defined as the energy gap between E_V and E_F. For an inverted p-type absorber at equilibrium the quantity $E_{p,a}$ is small in the bulk and large at the interface. It is possible to refer to $E_{p,a_{z=0}}$ to quantify the degree of the absorber free carrier inversion, where z = 0 indicates the absorber/buffer interface. Ideally $E_{p,a_{z=0}}$ should be as close as possible to the E_g of the absorber [54, 55]. If we assume the heterostructure to be composed solely by the absorber/buffer heterojunction, $E_{p,a_{z=0}}$ can be expressed as [54]:

$$E_{p,a_{z=0}}(V) = E_{p,a} + q(V_{bi} - V) \cdot \frac{\epsilon_b N_{D,b}}{\epsilon_a N_{A,a} + \epsilon_b N_{D,b}} \tag{2.3}$$

Where $E_{p,a}$ in this case is the energy gap between E_V and E_F taken in the absorber bulk far from the interface, V_{bi} is the built in voltage of the structure, ϵ_a and ϵ_b are the permittivity of the absorber and buffer respectively, $N_{D,b}$ and $N_{A,a}$ are the donor and acceptor density of respectively buffer and absorber layer. From Eq. 2.3 is clear that $E_{p,a_{z=0}}$ becomes larger when $N_{D,b} > N_{A,a}$. Since the built-in bias of the heterojunction is given by [54]:

$$qV_{bi} = E_{g,a} - E_{p,a} - E_{n,w} + \Delta E_c \tag{2.4}$$

$E_{p,a_{z=0}}$ will increase also with increasing ΔE_c, when E_c of the buffer layer is higher than the absorber E_c. The interface might contain some charged interface states that add to the charge balance between the absorber and buffer layer. If this charge is negative, in the case of acceptor defect states, it may decrease the inversion of the absorber and the opposite occurs if the defect charge is positive. The impact of the interface charge due to defects depends on the buffer/absorber charge balance. A high buffer doping density translates to a high buffer positive charge: if $N_{D,b} \gg N_{A,a}$ the positive charge of the buffer is able to screen a larger defect charge and at the same time to balance the absorber negative charge.

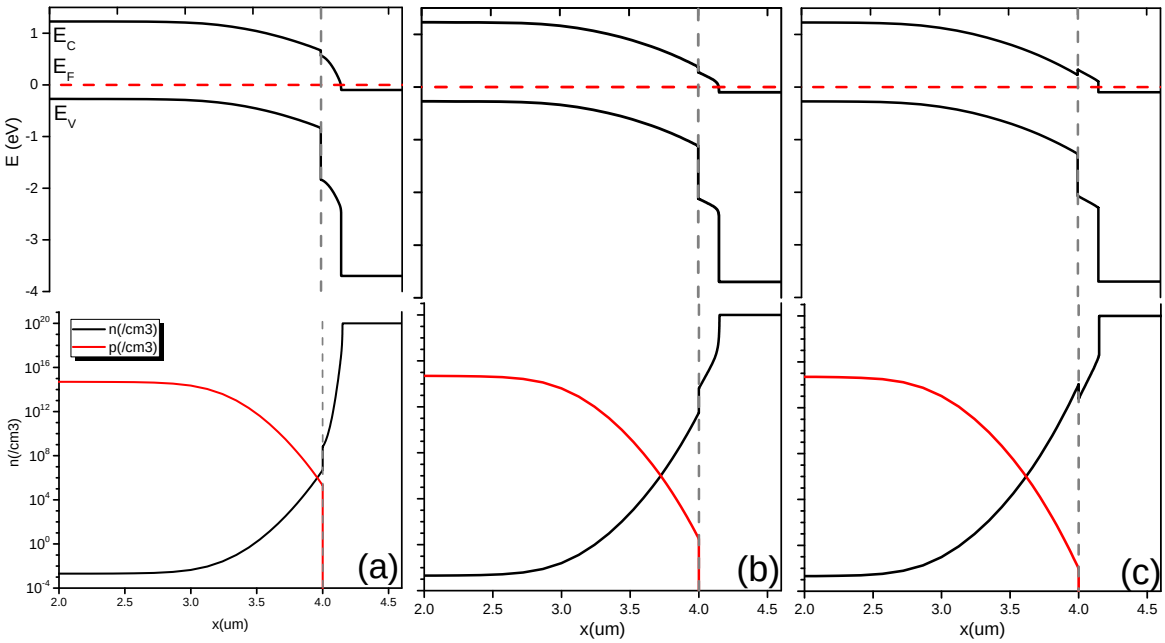

Figure 2.4: Simulation of absorber inversion for three different scenarios: (a) the reference structure composed by the CdTe layer with an average carrier concentration $N_{A,a}$ = 7 x 10^{14} cm^{-3}, the CdS donor concentration $N_{D,b}$ = 9.8 x 10^{17} cm^{-3}, the conduction band offset at the CdTe/CdS interface is $\Delta E_c^{b,a}$= -0.1 eV and the doping density of the TCO is 2.5 x 10^{21} cm^{-3}. The diagram in (b) shows a slightly different energy band structure simulated for a CdS doping concentration slightly increased to $N_{D,b}$ = 1 x 10^{18} cm^{-3}. In (c) both the donor concentration in the CdS and the conduction band offset at the CdTe/CdS interface were varied to $N_{D,b}$ = 1 x 10^{18} cm^{-3} and $E_c^{b,a}$= +0.1 eV respectively.

The quantity $E_{p,a_{z=0}}$ quantifies the type inversion of the absorber which is related to the carrier distribution throughout the device. In heterostructure devices interfaces can be critical. In a thin film CdTe solar cell there is a 10% mismatch factor between the CdTe and the CdS and as a consequence a large number of defects are likely to appear at the interface. As a result, the interface region is where the defect density rises compared to the bulk of the materials. Some of these defects lie within the band gap of the absorber or buffer and can be electrically active. Trapped carriers and recombination at the interface is one of the main causes of loss in V_{OC} and FF. It is crucial to avoid interface and near-interface recombination for a high performing device. Fig. 2.4 helps to visually explain the concept by showing a CdTe/CdS/TCO energy band structure and carrier distribution under three different situations simulated with SCAPS-1D: Fig. 2.4(a) refers to a reference structure of a CdTe/CdS/TCO solar cell. Fig. 2.4 (b) shows a slightly modified situation where the doping concentration of the CdS layer was increased. Finally in Fig. 2.4(c) the diagram represents the situation where the donor concentration of the CdS layer is equal to case (b) and the conduction band offset at the CdTe/CdS interface was changed from being slightly negative to slightly positive. Graphically we can see that $E_{p,a_{z=0}}$ increases from case (a) ($E_{p,a_{z=0}}$ = 0.83 eV) to case (c) ($E_{p,a_{z=0}}$ = 1.27 eV) through case (b ($E_{p,a_{z=0}}$ = 1.12 eV). Then, as suggested by Eq. 2.3 and 2.5, the increased buffer carrier concentration and the slightly positive conduction band offset between absorber and buffer increased the absorber inversion. The carrier distribution within the solar cells is related to the absorber inversion (Fig. 2.4, bottom graphs). The absorber depth at which hole and carrier concentration equalise is represented by the cross between the two concentration plots. This shifts further away from the interface when the inverter absorption increases, causing the hole and electron concentration to diverge at the interface. As a result at the CdTe/buffer interface, where the concentration of active interface states is normally higher than in the bulk, electron ricombination is limited by the lack of holes [55]. A positive ΔE_c then can decrease interface recombination. The offset however must be limited, since it can impede electron flow if too large. It is believed that $\Delta E_c^{b,a} = 0.3$ eV is the maximum value at which the device efficiency can benefit [56, 57, 58, 59].

If we add the TCO to form a TCO/buffer/absorber structure, $E_{p,a_{z=0}}$ becomes [54]:

$$E_{p,a_{z=0}}(V) = E_{g,a} + \Delta E_c^{TCO,b} + \Delta E_c^{b,a} - E_{n,b} + q\varphi(0) \tag{2.5}$$

Were $\Delta E_c^{TCO,b}$ is the conduction band offset between TCO and buffer, $\Delta E_c^{b,a}$ is the conduction band offset between buffer and absorber, $E_{n,b}$ is energy gap between conduction band and Fermi level in the buffer and finally $q\varphi(0)$ is the potential drop in the buffer and the TCO layer combination. The potential drop in these layers depends upon their carrier concentration and thickness, for example, since the TCO is highly doped, the potential drop in this layer is close to zero and can be neglected. For the slightly more complicated case where a HRT layer is inserted between TCO and CdS, the conduction band offset between buffer and TCO and the TCO carrier density must also be taken into account. This model implies that the performance of any heterostructure solar cell is strongly affected by the carrier concentration of each layer and the alignment of the transport energy levels at the interfaces.

2.6 Scope of thesis

The research presented in this thesis focuses on the window layers of thin film CdTe solar cells. The physical mechanisms at the front part of a CdTe solar cell are very complex and not entirely understood. Chapter 4 describes a detailed analysis of ZnO HRT layers which aims to provide information helping our understanding on why CdTe solar cells benefit from their use. This is one of the major gaps in our understanding of this technology. Chapter 5 is divided into two sections. The first section presents a study focusing on the relation of various band alignments of magnesium-doped zinc oxide (MZO) HRTs with the adjacent semiconductors and the performance of CdTe devices. Results highlight the importance of the HRT band alignment for device performance. Results of this first section provided the foundation for the second study described in this chapter. This involved the complete elimination of CdS layer from the CdTe solar cell, replaced by a TCO/MZO/CdTe/back contact structure. The utilisation of this structure establishes a new process for CdTe solar cell production in CREST. This fabrication processes and the materials involved are all compatible with scalability to larger module production. Finally, Chapter 6 compares the performance of different glass superstrates and TCOs,

namely ITO, FTO, AZO and ITiO, in combination with MZO buffers to form the window bilayer of CdTe solar cells.

Chapter 3

Experimental methods and characterisation

The fabrication of CdTe solar cells involves the deposition of different materials on glass. The CdTe devices discussed in chapter 4 were partially fabricated by Colorado State University PV group whilst the thin film CdTe solar cells described in the first part of chapter 5 were fabricated with the aid of Universita' di Verona PV group. For both these collaborations the glass superstrates with TCO and HRT coatings were prepared in the CREST laboratory whilst the remaining processing steps were carried out by the collaborating PV group. This is because at the time of processing no baseline process had been developed at CREST when these studies were carried out. Thin film CdTe solar cells produced at CREST are presented in the second part of chapter 5 and in chapter 6. Since there are several fabrication techniques involved, their full description will be given in the respective chapter whilst the standard techniques involved in the preparation of superstrates for device fabrication will be described in the following two sections. In the remaining sections of the chapter the focus will go on the techniques used to characterise materials and devices studied in this thesis.

3.1 Superstrate preparation

3.1.1 Glass superstrate preparation

A standard cleaning step was applied to the glass superstrates prior to deposition to aid film growth and consequent quality. Glass superstrates were wiped with a tissue with a mixture of deionised (DI) water and isopropanol (IPA) to remove visible impurities. The superstrates were then placed in an ultrasonic bath heated to 50 °C in a solution composed of 1/3 DI water, 1/3 isopropanol (IPA) and 1/3 acetone for 1 hour. Finally, the substrates were removed, rinsed with DI water and stored in DI water to prevent contamination prior to use. The glass type varied depending on the study.

3.1.2 Magnetron sputtering

In this work, sputtering was used as the deposition technique for TCO and HRT thin films. Sputtering is a well-known and effective way to deposit thin films. It involves ion bombardment of the target surface. Material ejected from the target surface is then directed to the substrate, where it condenses into a film. The deposition chamber of a sputtering system is initially placed under high vacuum to exclude contaminant gases which may interfere in the process. Before the process starts the chamber is filled with argon and other intentional reactive gases such as oxygen. By applying a high voltage to the target a glow discharge is created resulting in the creation of plasma from the process gas. The substrate is kept at zero voltage while the target is biased at a high negative voltage. The positively charged Ar ions are accelerated towards the target surface by the electric field; the kinetic energy of the argon ions is used to eject material from the target surface which will eventually reach the substrate surface, nucleate, and grow into a thin film. Depending on the composition of the sputtering atmosphere and the target composition, the plasma shows a characteristic glow that is caused by photon emission due to the re-encounter between electrons and ions to form atoms again. Magnetron sputtering uses a magnetic field to keep the plasma near the target, intensifying the bombardment of ions and increasing the process efficiency.

The sputter deposition of aluminium-doped zinc oxide (AZO), zinc oxide (ZnO),

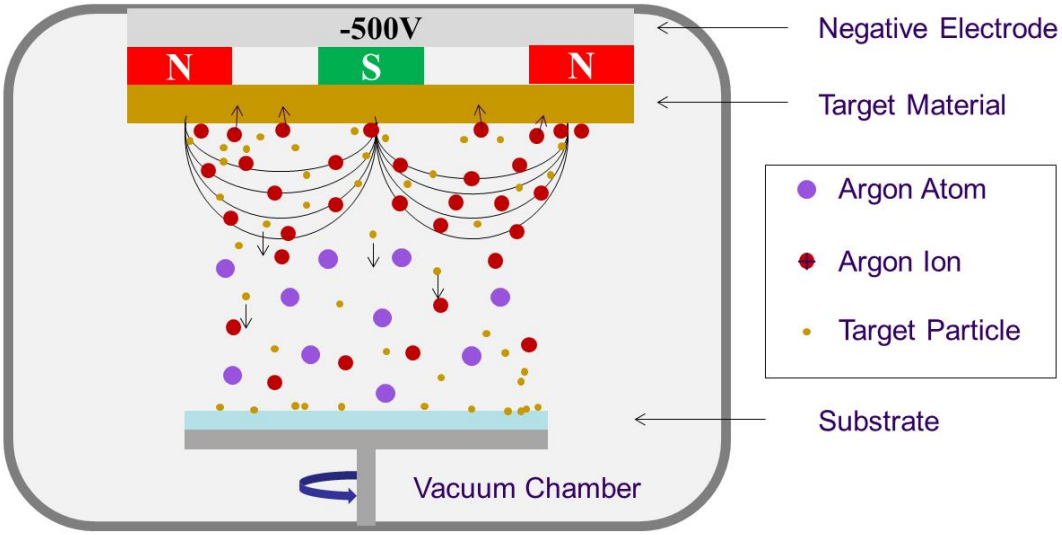

Figure 3.1: Simplified diagram of the sputtering system used at CREST.

magnesium-doped zinc oxide (MZO), tin-doped indium oxide (ITO) and titanium-doped indium oxide (ITiO) were performed at CREST. The films were deposited using an AJA international Orion 8HV magnetron sputtering system. All films were deposited from a 7.62 cm diameter targets using an AJA 600 series radio-frequency (RF) power supply. The system allows variation of sputtering power, sputtering pressure, substrate temperature and gas composition. The sputtering power influences the voltage at which the target is held and the kinetic energy of both the ions hitting the target surface and sputtered material reaching the superstrate surface. The chamber pressure also affects the energy of the sputtered material; a higher pressure translates in a decreased mean free path of the sputtered atoms and a reduction of their kinetic energy. The substrate temperature can be tuned (up to 700 °C) to provide the energy required by the deposited atoms to create the preferred crystal structure. Finally the gas mixture can be adjusted to include extra elements to the reaction. In this work oxygen was added for certain materials during the sputtering process. All these parameters can be used to affect the properties of the grown material. The main chamber is constantly under high vacuum (below 5×10^{-7}Torr) and the substrate is typically rotated to increase film uniformity.

3.2 Material optical characterisation

3.2.1 Spectrophotometry

The optical properties of the window materials of a thin film solar cell are of crucial importance since they will directly affect the generation of photocurrent in the absorber. Spectrophotometry is a technique that allows the measurement of the wavelength-dependent transmission, reflection and absorption of a material. The technique was carried out using a Cary 5000 (Agilent technologies, USA) spectrophotometer. For the analysis of thin film samples, an integrating sphere was used. The integrating sphere is a hollow sphere coated internally with a very reflective material that serves to integrate both the direct and diffused light that is transmitted or reflected by a film. The spectral range of analysis available is between 200nm and 2500 nm. If transmittance is to be measured, the sample is placed over a small aperture in front of the integrating sphere. A light source illuminates the sample and the transmitted light is integrated by the sphere and then detected by a sensor through a second small aperture in the sphere. When examining the reflection of a sample, the frontal aperture is left free while the sample is placed over a third aperture, known as the reflection port. This is opposite the transmission aperture, and during transmittance measurement is covered by a reference reflectance disk. Prior to sample measurement, the 100% and 0% transmission baselines must be taken. The 100 % baseline is taken by leaving the front opening free and gives the wavelength-dependent transmission characteristic properties of the integrating sphere. The 0% baseline assumes that no light is detected when the front opening is covered, hence the light beam must be blocked before entering the sphere. Sample spectra are provided as a percentage of these two baseline. Sample absorption spectra can be calculated using the formula 3.1

$$a(\lambda) = 1 - t(\lambda) - r(\lambda) \tag{3.1}$$

Where a(λ) is the wavelength-dependent absorption, t is the transmission and r is the reflection of the sample.

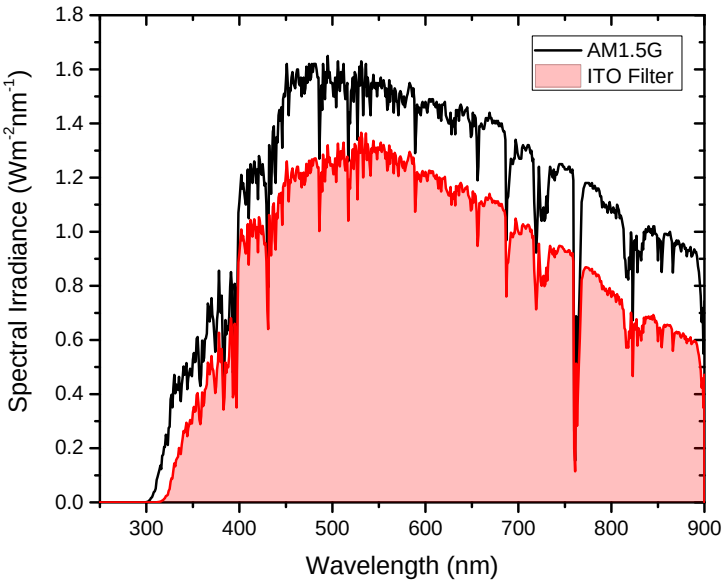

Figure 3.2: The diagram presents the AM1.5G spectrum before (black line) and after (red line) being filtered with an ITO filter. The modelled Jsc is calculated by integrating the number of photons available below the red curve.

3.2.2 Transmittance data modelling

A Matlab script previously written at CREST has been used in chapter 4, 5 and 6 to model the ideal Jsc of a CdTe solar cell from the transmission spectrum of the TCO or of the TCO/buffer combination. A graphical example of the methodology is given in Fig. 3.2. The AM1.5G spectrum is used as a starting point and is filtered with the transmission spectrum being modelled, which simply constists in the multiplication of the wavelength dependent power of the spectrum (P(λ)) and the respective transmission %. The result yields the theoretical spectral irradiance available after the light pass through the filter (red line in the graph). The calculation of the photon flux at each wavelength (F(λ)) is done by dividing the power by the photon energy

$$F(\lambda) = \frac{P(\lambda)}{E(\lambda)} = \frac{P(\lambda)\lambda}{hc} \tag{3.2}$$

where h is the Planck constant and c is the speed of light. Assuming all electrons generated by photons will be extracted from the solar cell to an external circuit, the Jsc value can be calculated as

$$J_{sc,max} = \int_0^{855} qF(\lambda)d\lambda \tag{3.3}$$

By limiting the wavelength range to everything shorter than 855 nm (1.45 eV) the CdTe absorption is simulated. This calculation is made assuming that the layers optical characteristic is not affected when other materials are added on top of the TCO. This is not the case, nevertheless the modelled Jsc value provides a relative value which is useful to compare the optical quality of the films.

3.2.3 Band-gap calculation

The semiconductor band-gap can be estimated using the method first discovered by the physicist Jan Tauc [60]. The Tauc technique is graphical and involves plotting $(\alpha h\nu)^2$, where α is the wavelength-dependent absorption coefficient against the photon energy. The resulting graph is known as a Tauc plot, presenting an absorption edge as a roughly linear drop. The band-gap is extrapolated by fitting the linear drop and estimating its intercept with the x-axis (figure 3.3).

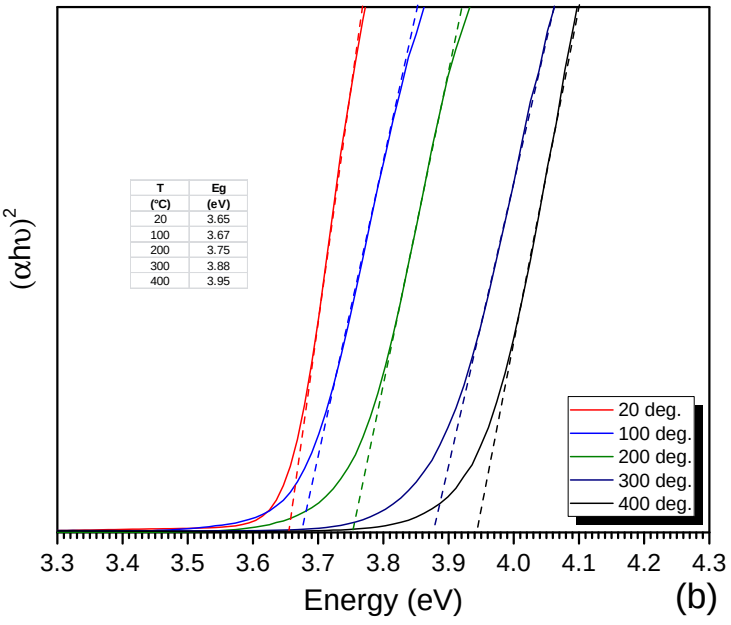

Figure 3.3: Tauc Plot of MZO films deposited at temperatures ranging between 20 and 400 °C

The absorption coefficient can be extracted from the transmission and reflection spectra using Equation 3.4.

$$\alpha = -\ln(\frac{lx}{1-R})/d \tag{3.4}$$

Where lx is the normalised transmittance for a given photon energy, R is the normalised reflectance for the given photon energy and d is the film thickness.

3.3 Electrical characterization

3.3.1 Four-point probe

The four-point probe is a technique used to measure the sheet resistance of a metal or semiconductor. R_{sheet}, which is given in units of Ω/sq, is a standard electrical parameter used to evaluate the TCO layer conductivity. The setup involves 4 equally spaced electrodes in a line, with the two outer ones being current-currying and the two inner ones being voltage sensing. These are brought in contact with the film surface (Fig 3.4). The separation of current and voltage electrodes eliminates problems due to high contact resistance between the probes and the film as well as very low material resistances. Having a second set of probes measuring only the voltage drop across the film makes the measurement more accurate since negligible current is flowing through them. The sheet resistance is obtained using equation 3.5.

$$\rho_s = \frac{\pi}{\ln 2}\frac{V}{I} \tag{3.5}$$

Where V is the measured voltage drop and I is the applied current. When measuring a conductive sample it is possible to take advantage of the fact that the ratio $\pi/\ln 2$ is equal to 4.53236 and then, if a current of this value in mA is applied then the output measured in mV corresponds to the sheet resistance. When dealing with resistive samples however, the current-voltage relationship can lose its linearity due to a high contact resistance. Low conductivity films, to be measured, require reducing the current input and find a region in the IV curve where the linearity holds; a software was created for this purpose with LabVIEW programming language. The script allows the control of a Keithley 2400 source-meter which, connected to a four-point probe, provides a IV profile between a chosen range of current values. Plotting the IV profile makes it possible to locate the

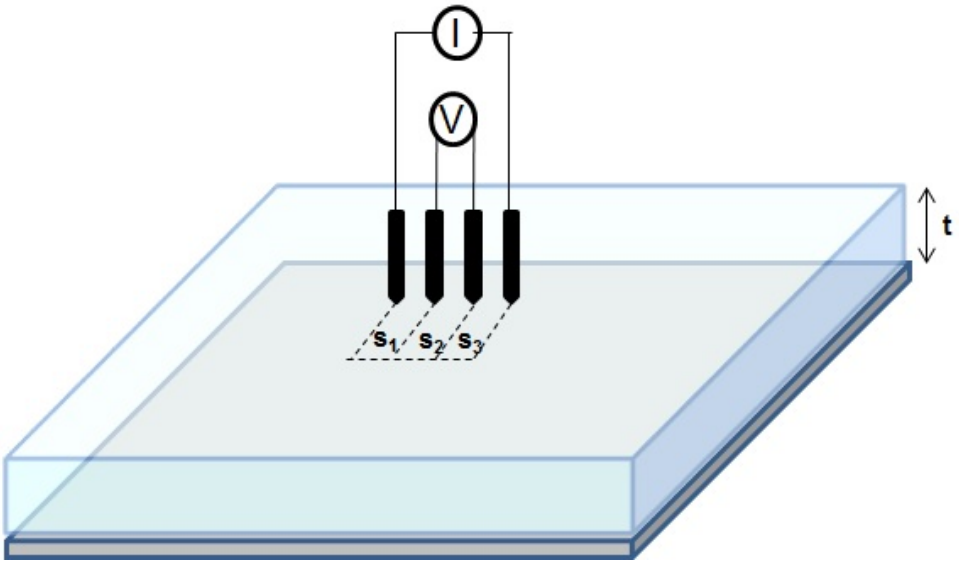

Figure 3.4: A schematic representation of a 4-point probe system

range of currents for which the IV relationship is linear. The value of R_{sheet} can then be extrapolated from the slope of the plot.

The sample sheet resistance of the film can also be described by Equation 3.6 which links it to the resistivity by knowing the thickness of the film.

$$R_{sheet} = \frac{\rho}{d} \tag{3.6}$$

The Hall effect method (described in the next section) was used to estimate the mobility and the carrier concentration of the film.

3.3.2 Hall effect method

The Van der Pauw Hall Effect method was used to measure the resistivity, Hall mobility and carrier concentration of a conductive material. Hall Effect measurements presented in this work have been carried out using an Ecopia HMS-3000 Hall Measurement System. A square sample with a maximum size of 4 cm^2 can be used. Electrical contacts must be placed at each corner of the sample. Before the measurement starts it is necessary to specify the intensity of the current input, the delay time, the sample thickness and the magnet strength. The input current depends on the sample's resistivity and it is selected using a software tool which tests the IV linearity within a chosen range. The

delay time depends upon how long a sample takes to stabilize after the current is applied. A value of 0.1 s of delay time was applied for all measurements carried out for all these thesis. The magnetic strength is characteristic of the magnet and was set at 0.55 Tesla. The technique consists of subsequent measurements of the voltage between each pair of contacts. The measurement is reiterated until all the possible contact combination have been analysed. The entire process is repeated three times; at first the magnet is removed from the system; then the magnet is positioned around the sample and then the magnetic field is reversed. The magnetic field, which is perpendicular to the current input, is used to push the electrons to one side of the film (Lorentz force). The accumulation of electrons on one side of the film creates a Hall voltage V_H

$$V_H = \frac{IB}{qN_s} \tag{3.7}$$

Where N_s is the sheet carrier concentration of the film that can be converted to the bulk carrier concentration, N_b, knowing the thickness of the film. The Hall mobility of the film can be deduced from resistivity and carrier concentration through

$$\mu = \frac{1}{qN_sR_{sheet}} = \frac{|V_H|}{R_{sheet}IB} \tag{3.8}$$

3.4 Structural and compositional characterisation

3.4.1 X-Ray diffraction

The structural properties of crystalline materials are highly linked to its opto-electrical characteristics. X-Ray diffraction (XRD) is a technique that makes use of Bragg's law to determine the atomic structure of a crystal. Bragg's law states that when shining an appropriate electromagnetic wave on a crystal, it is possible to observe interference phenomena caused by the reflection of such waves from parallel crystal planes of the material crystal. Bragg's law follows Eq. 3.9.

$$n\lambda = 2d\sin(\theta) \tag{3.9}$$

Where θ is the angle between the light ray and the crystal plane, λ is the wavelength

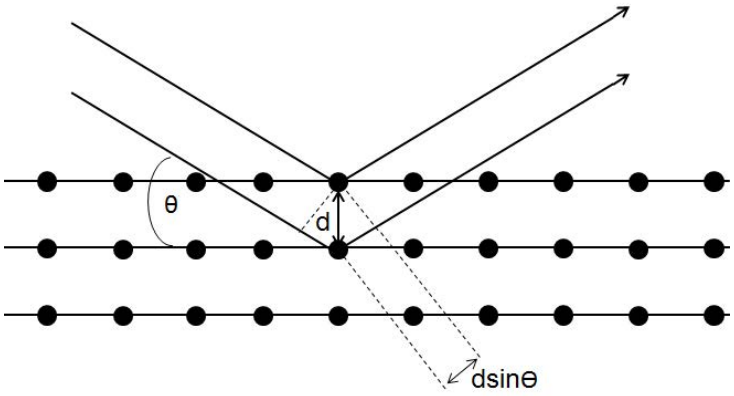

Figure 3.5: Schematic describing the Bragg's law. The light reflected by the second plane will have a longer optical path than the one reflected by the first plane. The excess length is given by $2dsin\theta$.

of the electromagnetic radiation, d is the distance between two adjacent planes and n indicates the order of the diffracted wave (typically n=1).

The system used in this work is a Bruker D8 diffractometer using radiation with a wavelength of 1.5406Å. For the diffraction to happen the wavelength of the radiation needs to be of similar magnitude to the atomic spacing. The role of this device is to shine a monochromatic beam of X-rays towards a sample. The source and the detector scan through a predetermined range of 2θ angles (the registered angle is twice the diffraction angle) in respect to the sample surface. The first plane the beam encounters will reflect part of the radiation and transmit the other, and the same will be for the following planes. If the reflected X-rays from different crystal lattice stratum are in phase, they will interfere constructively and a peak will be registered by the detector. Otherwise the interference will be destructive and only the back ground noise will be recorded. The 2θ data are recorded and peaks can be identified by comparison with diffraction files from the International Centre for Diffraction Data (ICDD).

3.4.2 Electron microscopy

An electron microscope is a device used to investigate the surface and the cross-section of thin film materials with nanometer resolution. It uses accelerated electrons as a source of illumination since the wavelength of an electron can be significantly smaller of that of a visible photon, and as such can examine the structure of smaller objects. The elec-

tron beam produced by a gun (cathode) can be controlled by using electrostatic and electromagnetic lenses and an anode to accelerate the beam. These lenses consist of coils producing a magnetic field that focuses the electron beam towards the chosen sample area. The electrons encountering the specimens are absorbed, scattered or transmitted. Different regions of the material will have different electron scattering properties. Transmission electron microscopy (TEM) detects the electrons transmitted through the film and not those ones scattered or expelled. Since the electrons are transmitted across the sample this technique enables imaging through the sample rather than imaging its surface. TEM uses a large voltage to provide a higher acceleration to the electron beam. It also requires thinner films (around 200 nm). The best TEM systems can image the material down the atomic scale. Samples for TEM cross-section were prepared by Focused Ion Beam (FIB) milling using a dual beam FEI Nova 600 Nanolab. A standard in-situ lift out method was used to prepare cross-sectional samples through the coating into the glass substrate. An electron beam assisted platinum (e-Pt) over-layer was deposited followed by an ion assisted layer to define the surface and homogenise the final thinning of the samples down to 100 nm. TEM analysis was carried out using a Tecnai F20 operating at 200 kV to investigate the detailed microstructures of the cell cross sections. The system was equipped with an Oxford Instruments X-max N80 TLE SDD energy-dispersive X-ray spectroscopy (EDX) detector which was used in STEM mode to produce elemental distribution maps. These maps were collected in a single frame using a long dwell time. A small condenser aperture (70 microns) to minimize drift and beam spread during data collection.

3.4.3 X-Ray photoelectron spectroscopy

X-ray photoelectron spectroscopy (XPS) is a high vacuum technique used to characterise the elemental composition of a material surface. The sample is irradiated with a monochromatic X-ray beam where photons enter the material and interact with its atoms. The photoelectric effect and Auger emission are the two types of interaction exploited using this technique. In both cases an electron is expelled from the material with a kinetic energy that is related to the energy of the bond the electron has come off. By measuring the kinetic energy of the expelled electron with a detector it is possible to establish the bond energy using Eq. 3.10

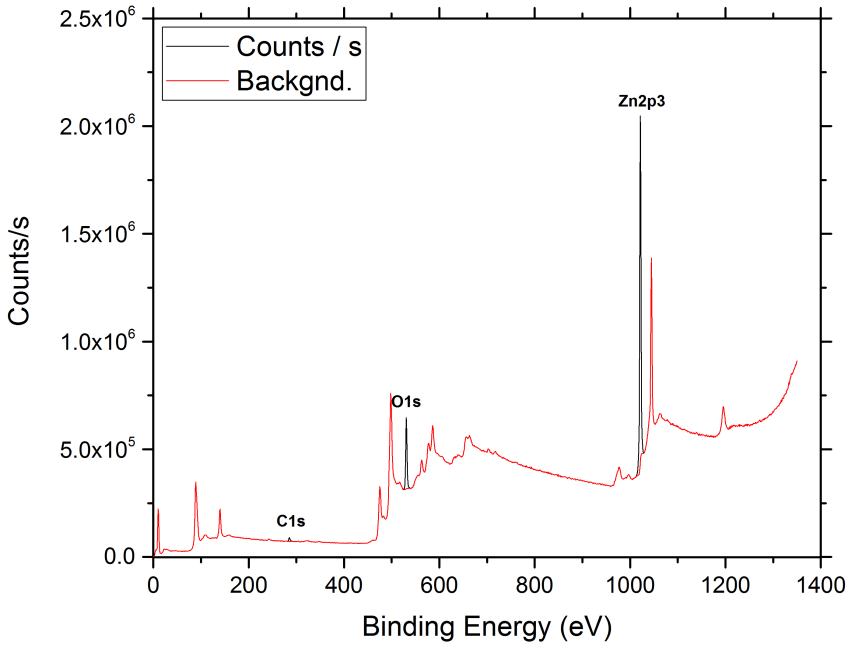

Figure 3.6: Example of a XPS profile of a ZnO sample. The red signal is due to the background noise and it is typical of the system. The Zn2p3 and O1s peak confirm the presence of both Zn and O. The C1s peak is related to some unavoidable contamination of the sample's surface

$$E_B = h\nu - K - \phi \tag{3.10}$$

Where E_B is the energy of the bond, hν is the energy of the incident photons, K is the kinetic energy of the electrons and ϕ is the work function of the detector. Only the very first atomic layers (few nanometres deep) can be analysed since only electrons exited near the surface can exit the sample without interfering with the surrounding material. A Thermo-Fisher Scientific K-alpha Surface Analysis instrument was used in this work. The system uses an aluminium X-ray source ($K\alpha$ 1486.6 eV). Data analysis was performed using the NIST XPS database.

3.5 Device characterisation

Efficiency, FF, Voc and Jsc were the main parameters used to evaluate the performance of the thin film CdTe solar cells fabricated described in this work. These parameters are calculated using the current density-voltage characteristics (J-V) of these devices,

measured under a simulated a AM1.5G spectrum at 1000W. The light was sourced by a bespoke solar simulator using a high power (1kW) Xenon arc lamp (Osram, XBO1000W/HS, Germany) filtered to match AM1.5G, and calibrated with a Si photodiode.

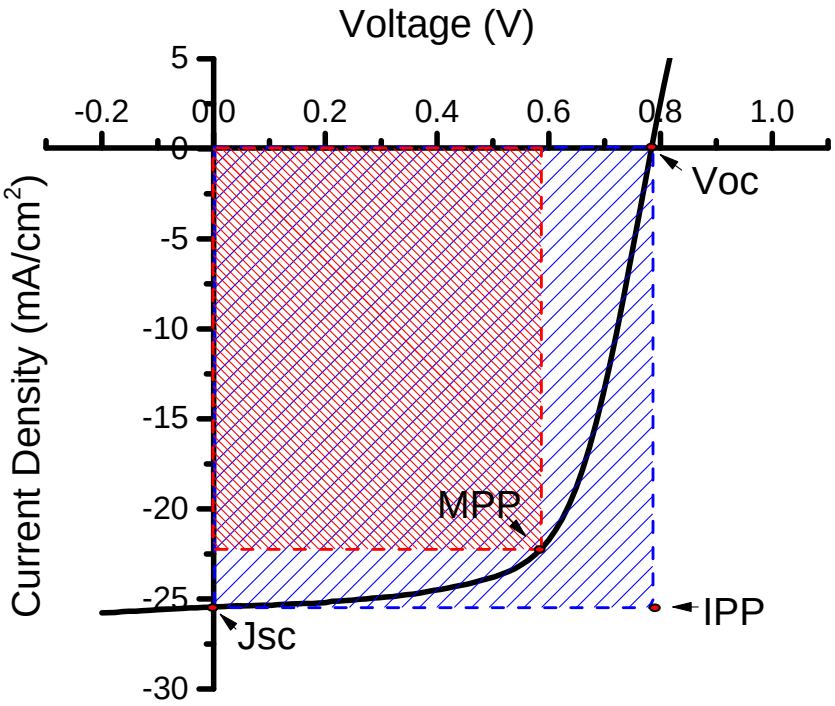

Figure 3.7: The diagram presents graphically the short circuit current density (Jsc), the open circuit voltage (Voc) and the FF of a solar cell. The FF can be seen as the ratio between the area of the red rectangle with vertex in the maximum power point (MPP) and the area of the blue rectangle which represents the ideal power yielded by the same solar cell if the diode was perfect (IPP). In other words the FF reflects the quality of the diode by quantifying the squareness of the J-V curve.

The cells were contacted using a four-wire configuration using two double-ended Kelvin probes. The bias sweep (between -0.2V and 1V) and the current response were respectively sourced and measured using a LabVIEW (National Instruments, USA) controlled source-meter (Keithley 2425, USA).

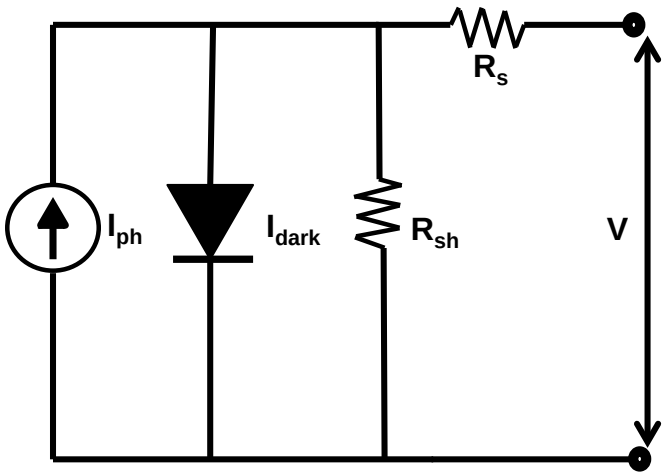

Figure 3.8: The circuit diagram of a non-ideal solar cell with series (Rs) and shunt (Rsh) resistance losses

The extrapolation of Jsc and Voc from the J-V characteristic is straight forward, with Jsc being the current density when the device is not biased and Voc the voltage when no current is flowing within the device. The FF is given by the ratio between the actual maximum power produced by the device and the ideal power the device would produce if the diode was perfect (Fig. 3.7). The efficiency depends upon the 3 parameters following Equation

$$n = \frac{P_{in}}{P_{out}} = \frac{I_{sc} V_{oc} FF}{P_{out}} \tag{3.11}$$

which is the ratio between the incoming power (Pin) and the output power (Pout) of the solar cell. Extra information were extrapolated by using a single diode model of a non-ideal solar cell has been used (Fig. 3.8). The model includes shunt and series resistance losses

$$I = I_0\left(e^{q(V+IR_s)/(nK_BT)} - 1\right) + \frac{V + IR_s}{R_{sh}} - I_{ph}$$

(3.12)

where I is the net current flowing through the diode, I_0 is the dark saturation current or leakage current, Iph is the photogenerated current, V is the applied bias across the terminals of the diode, q is the electron charge, k is the Boltzmann constant, T is the absolute temperature (K), Rs is the series resistance of the device, Rsh is the shunt resistance of the device and n is the diode ideality factor. In some cases the J-V curves were modeled on a single diode model [61] using Visual Basic Excel macros previously developed at CREST. In these cases Rs and Rsh are provided.

Chapter 4

Investigation on ZnO HRT layers

4.1 Introduction

The physical mechanisms related to the role of HRT layers in CdTe solar cells are not fully understood. This study aims to anlyse the relation between HRT film characteristics and device performance, with a focus on resistivity, crystal structure and interface properties of ZnO HRTs. ZnO film properties have been varied by tuning independently the sputtering gas pressure, substrate temperature and gas composition. Results of these three studies have been divided in three sections. A detailed characterization of films was used to take into account as much information as possible during this analysis. The novelty lies in the information that this study provides. ZnO is widely used in chalcogenide solar cells like copper indium selenide (CIS), copper indium gallium selenide (CIGS) and CdTe based devices [62, 25, 63, 64, 65]. It was chosen as material, however, because some of its characteristics can be easily tuned by varying the deposition conditions. ZnO is a II-VI semiconductor with a band gap of $\approx$ 3.3 eV, transmitting wavelengths of $>$ 360 nm. It most commonly assumes the hexagonal wurtzite crystal structure (unit cell: a = 0.325nm, c = 0.52006 nm) where the zinc atoms are surrounded by oxygen atoms in a tetrahedral configuration (Fig. 4.1) [66]. A cubic phase with the zinc blend structure is also known but occurs less frequently due to lower stability at room temperature and atmospheric pressure [66]. ZnO can exhibit a n-type behaviour even when un-doped, due to intrinsic defects (oxygen vacancies and interstitial zinc atoms) [67].

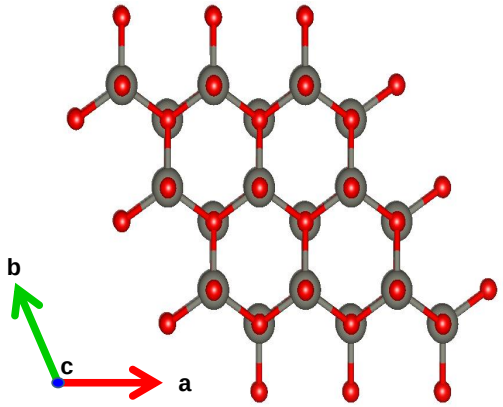

Figure 4.1: (a) The hexagonal ZnO crystal structure can clearly be seen looking down the c-axis; each oxygen atom (red sphere) is surrounded by 4 Zn atoms (gray sphere) and vice versa.

4.2 Methodology

Thin ZnO films were deposited by Radio-Frequency (RF) magnetron sputtering. Soda lime glass (SLG) and NSG TEC TM C10 glass (Pilkington) were used as superstrates. The cleaning technique of the glass superstrates has been previously described in chapter 3. Thin films were deposited using an Orion 8 HV magnetron sputtering system (AJA international, USA) equipped with an AJA 600 series RF power supply. The target diameter was 3", and the ZnO target purity was 99.99 %. The glass superstrates were rotated at 10 rpm during deposition to enhance the uniformity of the films. The sputtering process was carried out at a constant power density of 3.95 Wcm^{-2} using Ar and in some cases different combinations of Ar and O_2 as the working gases. The film thickness was fixed at 150 nm on SLG and on TCO-coated superstrates. The electrical properties of ZnO films were investigated using Hall Effect measurements obtained by the Van der Pauw method using an Ecopia HMS 3000 Hall measurement system. The optical properties were investigated by UV-VIS-NIR spectrophotometry using a Cary Varian 5000 spectrophotometer. The structural properties of the films were analysed by X-ray diffraction (XRD) using a Brucker D2 phaser desktop X-ray diffractometer equipped with a Cu-K-alpha X-ray gun. The XRD measurements were obtained using 15 rpm rotation, a 1 mm beam slit and 3 mm anti-scatter plate height. Devices were subsequently fabricated on ZnO-coated su-

perstrates by the PV group of Colorado State University using the Advanced Research Deposition System (ARDS), an in-line system which has been described previously [68]. The process included the deposition of CdS and CdTe, a $CdCl_2$ activation treatment and a Cu/Ni back contact. CdS was sublimated at a substrate temperature of 420 °C while CdTe was sublimated at a substrate temperature of 360 °C. The $CdCl_2$ treatment was carried out for three minutes at a substrate temperature of 388°C. The thicknesses of CdS and CdTe films were maintained at ≈120 nm and 2.3 µm-2.5 µm respectively. Devices performance was calculated using current density-voltage (J-V) measurements and 1000 W/m^2 irradiance. Cross-section images were obtained using transmission electron microscopy (TEM). Samples for TEM were prepared by focused ion beam milling using a dual beam FEI Nova 600 Nanolab. A standard in situ lift out method was used to prepare cross-sectional samples. An electron beam assisted platinum (e-Pt) over-layer was deposited onto the sample surface above the area to be analysed followed by an ion assisted layer to define the surface and homogenize the final thinning of the samples down to 100 nm. TEM analysis was carried out using a Tecnai F20 operating at 200 kV. Unless otherwise stated, images were taken using the bright field (BF) detector; for elemental contrast images the high angle annular dark field (HAADF) detector was used also to take some images. The behaviour of solar cells was modelled with SCAPS-1D, a one-dimensional simulation program for solar cells. Device materials properties used for the simulations will be listed directly in the related section.

4.3 Variation of sputtering pressure of ZnO

ZnO films were produced at working pressures ranging between 1 mTorr and 9 mTorr. Prior to deposition the pressure in the deposition chamber was 3 x 10^{-7} Torr. The power and substrate temperature were kept constant at 180 W (3.5 Wcm^{-2}) and 20 $°C$ respectively. In the study presented in this first section the sputtering atmosphere was pure argon. Changing the sputtering pressured allowed the deposition of ZnO films with slightly different structural and optical properties, as detailed by XRD and spectrophotometry. Furthermore, the Hall effect method highlighted a significant increase in the resistivity of ZnO films was obtained by increasing pressure. An analysis of the relation

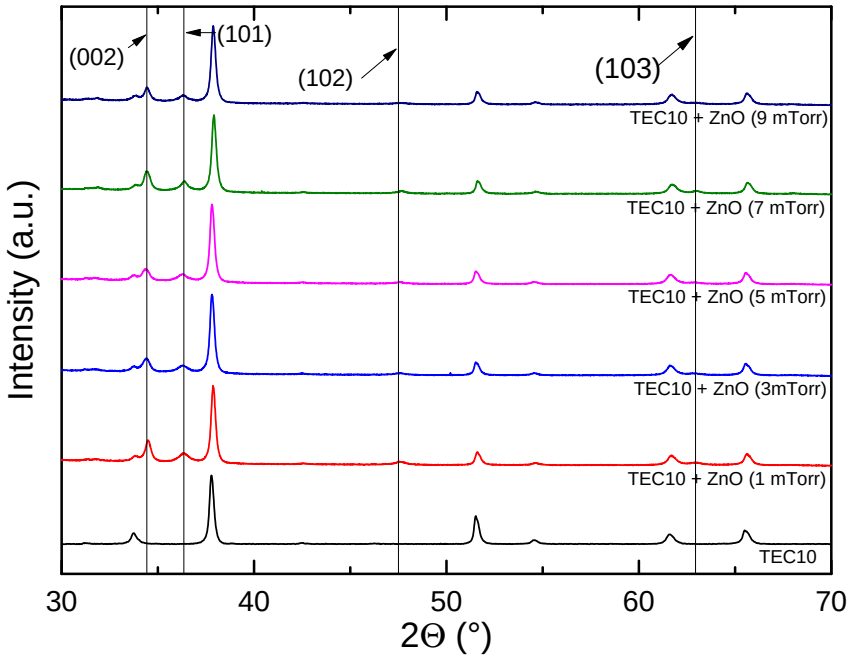

Figure 4.2: XRD patterns of ZnO films deposited on FTO coated glass

between these ZnO film properties and CdTe solar cell performance is finally given in the last part of this first result section of the chapter.

4.3.1 XRD characterization

XRD analysis was carried out on ZnO films deposited on FTO coated glass. FTO coated glass was also used for device fabrication, hence depositing ZnO on top of it simulates the growth conditions of ZnO in CdTe devices. The XRD patterns are shown in Fig.4.2, with the XRD plot of standard FTO coated glass to distinguish between peaks related to FTO and those related to ZnO. The (002) and (101) phases yield the two most distinct ZnO-related peaks. The (002) peak indicates that the film is growing with a c-axis preferential orientation perpendicular to the substrate [69]. The (101) peak's intensity is, depending on the deposition conditions, less intense or occasionally not noticeable at all when ZnO is deposited on bare glass by R.F. magnetron sputtering [70, 71]. This suggests that the underlying FTO induces the growth of this phase during sputtering. Peaks related to the plane orientation (102) and (103) are also appearing. Their intensity is very low when films are deposited at 1 mTorr or 7 mTorr and almost undetectable at the other deposition pressures. The peak position and full width half maximum (FWHM) of (002) and (101)

have been extrapolated by peak fitting (Table 4.1). The peak position of stress-free films provided by the Internal Centre for Diffraction Data (ICDD 00-003-0752) is 34.74° for the (002) peak and 36.80° for the (101) peak. Both (002) and (101) peaks for the deposited ZnO were found at lower 2θ angles than the ones proposed by the ICDD. Assuming the measuring setup and sample positioning are identical, a shift in peak position is generally related to increasing stress within the film crystal structure. In this case the peak shift towards lower diffraction angles indicates compressive stress formation in the deposited films along the related diffraction planes [72]. The distortion in the crystal lattice d-spacing is stronger for both diffraction planes when the films are deposited at 3 mTorr and 5 mTorr. It is possible that part of the distortion in the crystal lattice structure is caused by transmission of stress built up at the FTO/ZnO interface to the rest of the structure. The cause of the interfacial strain between the two semiconductors is the large mismatch factor between the two crystal structures (ZnO lattice constant c = 0.52066 nm [66], FTO lattice constant c = 0.3198 nm [73]). The FWHM can be associated with the average coherent domain length (ACDL) which can be smaller or equal to the crystallite size. A narrower FWHM generally relates to a wider coherent domain length. If applied to the XRD patterns, along the (002) plane the average coherent domain length is larger when ZnO films are deposited at 1 mTorr and at 9mTorr, if compared to films deposited at the other pressures. Similar observations can be drawn relative to peak (101). The ZnO peaks (101) and (002) show their respective minimum FHWM at different deposition pressures. The estimated ACDL values are above 10 nm for all samples and diffraction planes. An ACDL below 10 nm would mean that the band gap could begin behaving like a quantum dot, with consequent band gap variations. This does not happens in this case, in fact the band gap of all films is identical.

4.3.2 Electrical characterization

The electrical properties of ZnO used as a buffer/HRT layer have been analysed previously [62, 63]. The "pinhole" theory considers HRT layers to be barriers for shunts through the device. Following the "pinhole" theory there would be an ideal resistivity for any determined thickness at which the ZnO layer is sufficiently efficient at blocking shunt currents whilst low enough to avoid increasing the series resistance of the device, thereby

Table 4.1: XRD Peak position and FWHM and average coherent domain length (ACDL) values for ZnO films deposited at different deposition pressures.

Peak	Parameter	Deposition Pressure (mTorr)				
		1	3	5	7	9
(002)	2θ (°) [ICDD: 34.74]	34.50	34.40	34.37	34.45	34.45
	FWHM (°)	0.37	0.43	0.43	0.40	0.36
	ACDL (nm)	24	20	20	22	24
(101)	2θ (°) [ICDD: 36.708]	36.34	36.30	36.28	36.36	36.36
	FWHM (°)	0.56	0.50	0.55	0.46	0.67
	ACDL (nm)	16	17	16	19	13

causing a deterioration of the FF. The resistivity of ZnO layers was verified by the Van der Pauw Hall effect method. ZnO films were deposited on bare SLG so that the electrical properties of ZnO are isolated from the influence of other semiconductors. The Hall effect method highlighted that the variation of deposition pressure during the sputtering process provided a wide range of resistivity (Fig. 4.3). A minimum of ≈2.7 x 10^{-2} Ω·cm was reached at a deposition pressure of 3 mTorr and a maximum of ≈1.3 x 10^{4} Ω·cm was achieved at 9 mTorr, a difference of six orders of magnitude. While the resistivity values were consistent if the measurement was repeated, the measured values of carrier concentration and mobility changed significantly from one measurement to another. This is due to the relatively high resistivity of this films which does not allow to measure these parameters reliably. For this reason carrier concentration and mobility data are not reported. It was expected that once the ZnO films are incorporated as HRT layers in CdTe solar cells, this wide range of resistivity will produce a significant variation in the performance of such devices. This would support the "pinhole theory" .

The influence of the ZnO layer on the electrical properties of the TCO was investigated. FTO coated glass was used as a reference (sheet resistance 9.6 Ω/□). ZnO films were deposited on top of the TCO-coated glass using the same deposition conditions as the films discussed above. Thickness was maintained at 150 nm. R_{sheet} was then tested using a 4-point probe on top of the ZnO layer. The result was 9.6 Ω/□, showing no change from the TCO on its own. This suggests that the bi-layer is still conductive

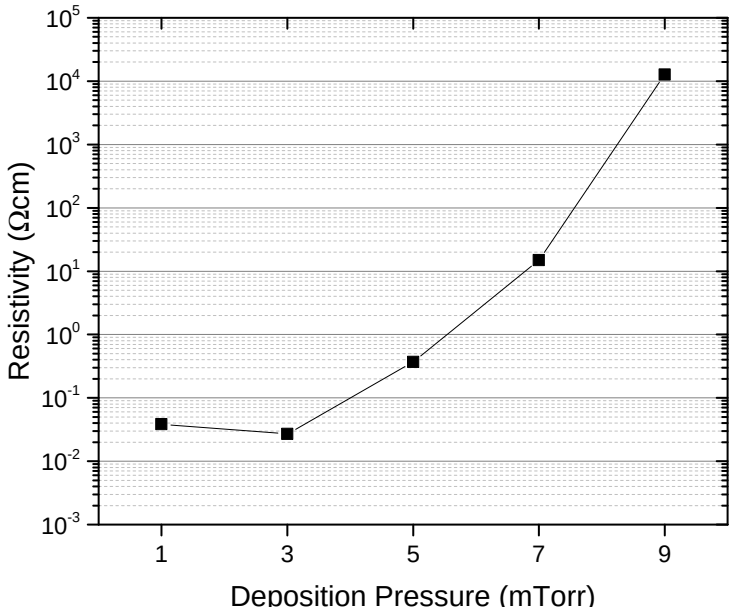

Figure 4.3: The variation of resistivity of ZnO films deposited at different deposition pressures

while it was expected that the higher resistivity of films deposited at higher deposition pressures on SLG would translate to a higher overall R_{sheet} when ZnO is deposited on FTO. One possibility is that ZnO films deposited on FTO have significantly different electrical properties than those deposited on bare glass. Another option is that because the TCO is a conductive layer rich in free carriers, a thicker or more resistive ZnO layer is required to isolate the TCO from the rest of the device. The thickness of HRT layers is however generally limited to maximum 150 nm-200 nm and often higher efficiencies are obtained with HRT layers as thin as 50 nm [74].

4.3.3 Optical characterization

The optical properties of ZnO are of key importance. The ZnO layer, along with the TCO layer, should let as much light as possible through to reach the absorber layer. Due to the relatively high band gap of ZnO (≈3.3 eV) and the low carrier concentration, which avoids plasma reflection in the near-infra-red (NIR), ZnO guarantees a high level of transparency. However, the transmittance of the ZnO films is affected by the deposition pressure. Transmission plots of FTO/ZnO bilayers are shown in Fig. 4.4. The films deposited at 3 mTorr and 5 mTorr yield lower transmittance, averaging 78% in the

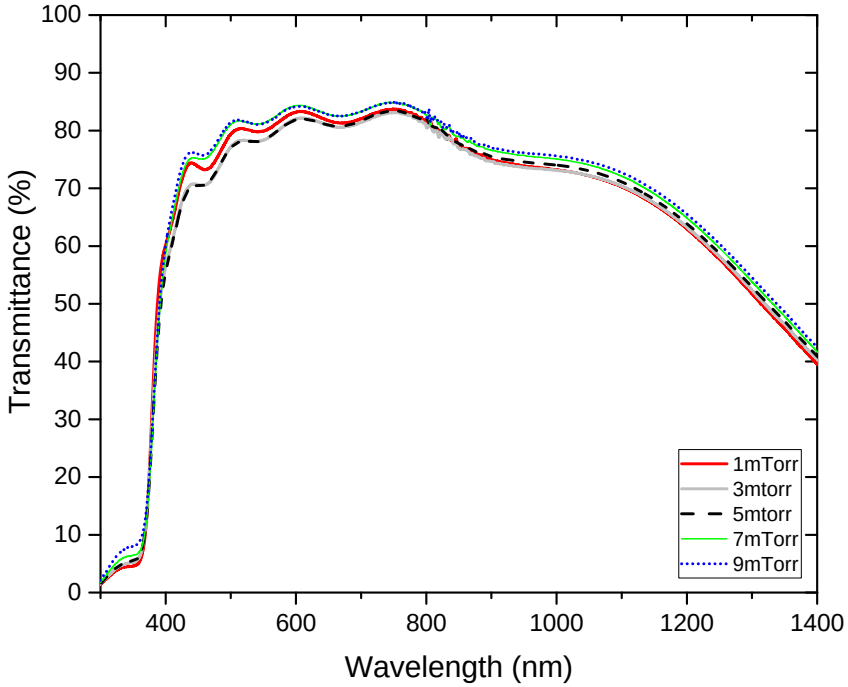

Figure 4.4: The transmission plots of ZnO films deposited on FTO coated glass at different deposition pressures

wavelength range 400 nm - 850 nm, while the ZnO with the highest average transmittance (81%) was deposited at 9 mTorr. The optical properties seem to be related to the XRD peak positions and ACDL listed in Table 4.1 and then to structural variations due to the changing deposition conditions.

A quantitative evaluation of the ZnO optical performance was modelled using a Matlab script previously described in chapter 3. The model computes the number of available photons from the AM1.5G spectrum and then filters it according to the transmission plots of Fig. 4.4 giving as an output the "available" Jsc. Results (Tab. 4.2) highlight that there is a potential Jsc difference of almost 1 mA/cm^2 translating in 1 % gain if the ZnO is optimised. It was then concluded that the optical properties of the FTO/ZnO bi-layer can be optimized by using an optimal ZnO deposition pressure.

Table 4.2: The table presents the maximum J_{SC} of a device depending on the transmittance of the FTO/ZnO bilayer. The column named "no filter" shows the potential J_{SC} if all the photons of the AM1.5G spectrum without any filtering, i.e. if all incoming photons would be available to the active layer of the solar cell.

Sample	no filter	1 mTorr	3 mTorr	5 mTorr	7 mTorr	9 mTorr
J_{SC} (mA/cm^2)	33.7	26.1	25.7	25.8	26.5	26.6

4.3.4 CdTe solar cells

The performance of CdTe solar cells incorporating ZnO HRTs is presented in this section. The main cell parameters are shown in Figure 4.5. The efficiency of the devices is similar despite a variation within the other performance parameters. The mean efficiency ranges from 11.6% for the 1 mTorr, 7 mTorr, and 9 mTorr samples to 11.3% efficiency at 3 mTorr and 11.2% at 5 mTorr. The relatively small difference can be explained by the fact that the influence of the ZnO layer on the device performance would be more pronounced if the CdS layer measured less than 100 nm [26], while in this study the CdS was ≈120 nm thick. The variation of J_{SC} and V_{OC} among devices follow a similar trend while FF follows an opposite trend (Fig. 4.5). As a result these performance parameters largely balance out and the samples yield similar efficiencies. These results do not show any clear correlation between increasing resistivity of the ZnO layer and device performance nor with crystal structure variation (as detailed in XRD studies). Samples containing ZnO films deposited at 3 mTorr, 5 mTorr and 7 mTorr have lower mean J_{SC}. This can be explained by the relatively low transmittance of ZnO films deposited at 3 mTorr and 5 mTorr while CdTe solar cells containing ZnO films deposited at 7 mTorr might be affected by some other mechanism. This could be caused by an high device recombination rate that would explain also the low Voc.

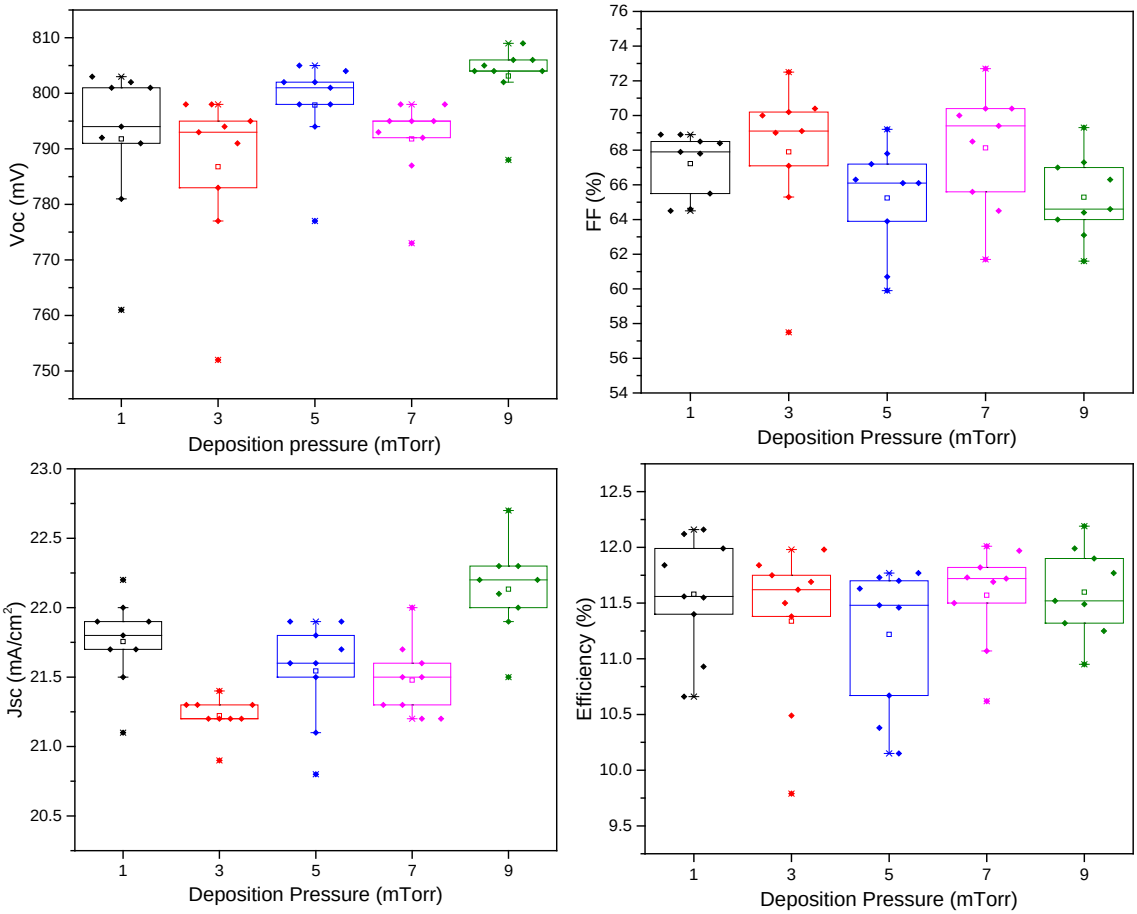

Figure 4.5: The efficiency, open circuit voltage, fill factor and short circuit current density of devices containing ZnO films sputtered at different deposition pressures.

4.4 The impact of sputtering temperature of ZnO

The ZnO films for this study were produced at a range of temperature between 20 °C and 400 °C. The power and pressure were kept constant at 180 W (3.5 Wcm^{-2}) and 1 mTorr respectively. The sputtering atmosphere was pure argon. The substrate temperature was used mainly to increase the grain size of ZnO films and relate its effect to device performance, although even the opto-electrical properties were slightly affected.

4.4.1 TEM cross-section images

Fig. 4.7 shows device TEM cross-section images with a focus on the TCO/ZnO interface.

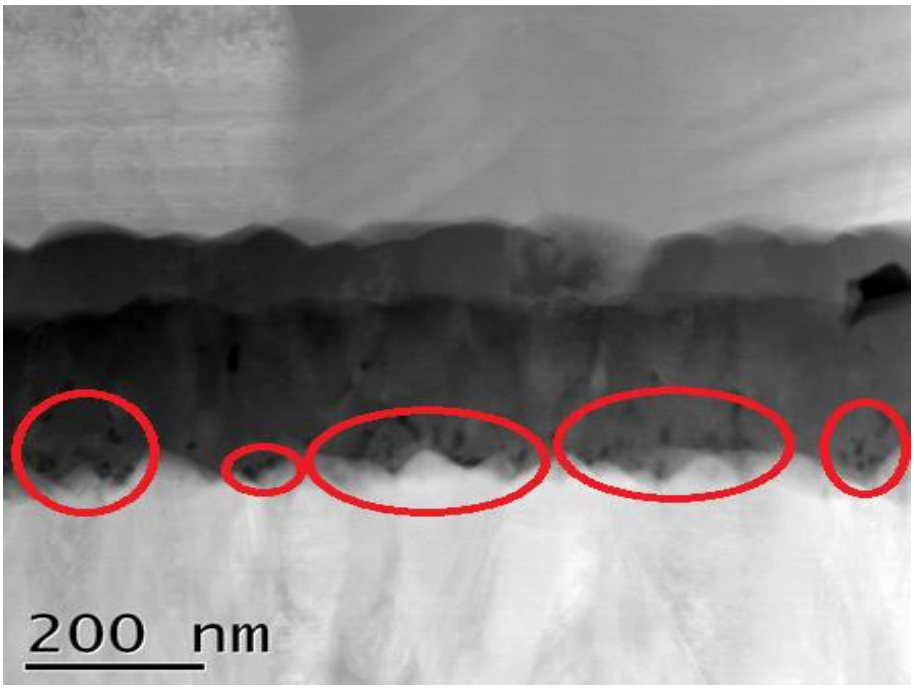

Figure 4.6: The interface between TCO layer and ZnO layer deposited at 20 °C, seen with TEM microscopy using the HAADF detector

The grain size of the ZnO layer increases at higher temperatures and at 200 °C and 300 °C the grains expand to the full height of the layer, with an average width of between 50 nm and 100 nm. The films deposited at room temperature contain smaller grains. The elemental contrast image (Fig. 4.6) of the cross section reveals the creation of small voids in the ZnO film deposited at 20 °C. These small voids appear as black spots (highlighted with red circles) and are concentrated at the interface with the TCO. They may be caused by stress build-up in the ZnO near-interface region due to the large lattice mismatch with the FTO (ZnO lattice constant c = 0.52066 nm, FTO lattice constant c = 0.3198 nm , Sec. 4.3.4). This phenomenon was not observed at higher ZnO deposition temperatures, possibly indicating that partial relaxation of the stress occurs.

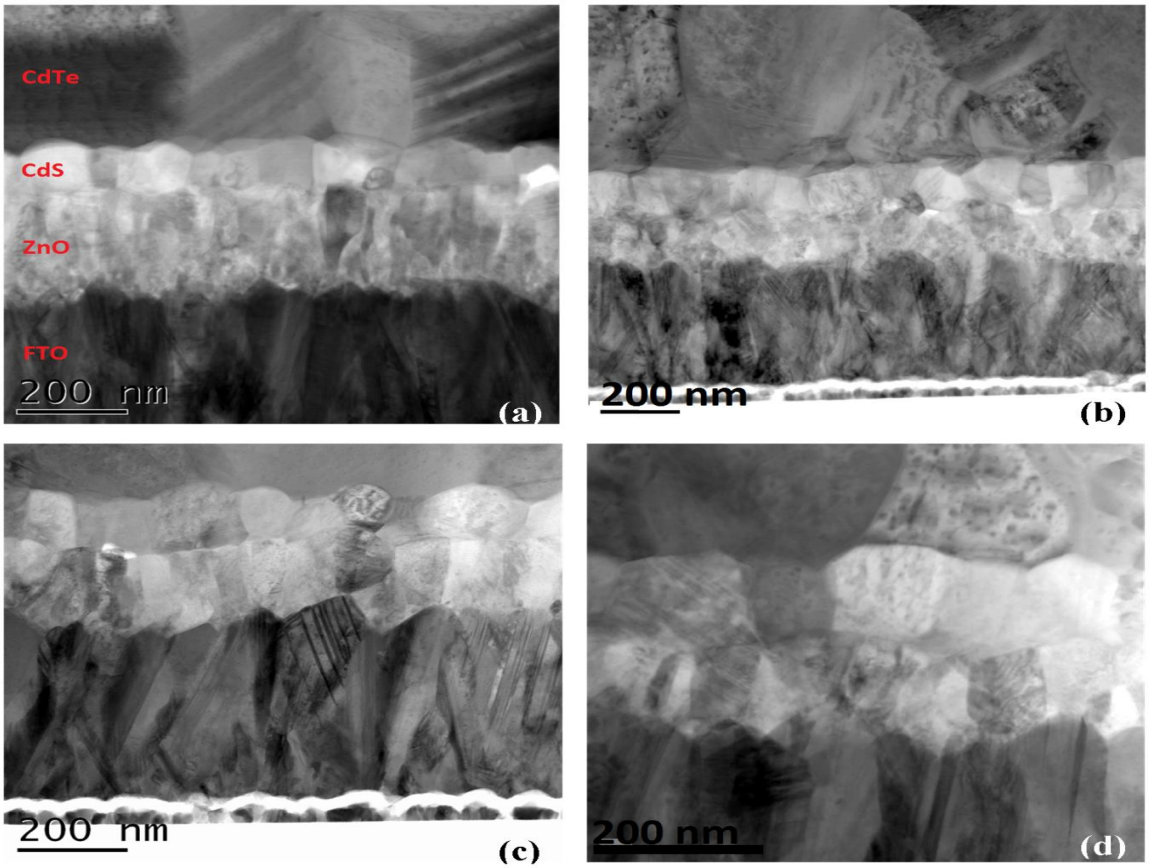

Figure 4.7: TEM cross-sections of devices including ZnO deposited at 20°C (a), 100°C (b), 200°C (c), 300°C (d).

4.4.2 X-ray diffraction (XRD)

The peak position 2Θ and its full width at half maximum (FWHM) were extrapolated by Gaussian fitting (Table 4.3). The (102) and (103) phases were taken into account in this analysis also. The position of all peaks of the various phases is shifted to slightly lower 2Θ angles in comparison with the reference peaks (ICDD 00-003-0752). The reference peak positions are 34.74°, 36.80°, 48.10°, 63.20° respectively for (002), (101), (102), (103). This can be attributed to the influence of the fluorine doped tin–oxide (FTO) coated superstrate on the ZnO growth (large miss-match factor). The FTO crystal structure mismatch with ZnO may force the film to grow in a different way than on bare glass. The peaks associated with the ZnO films deposited at room temperature have the 2Θ peaks close to the ICDD values (similarly to what found in the previous section) whilst their

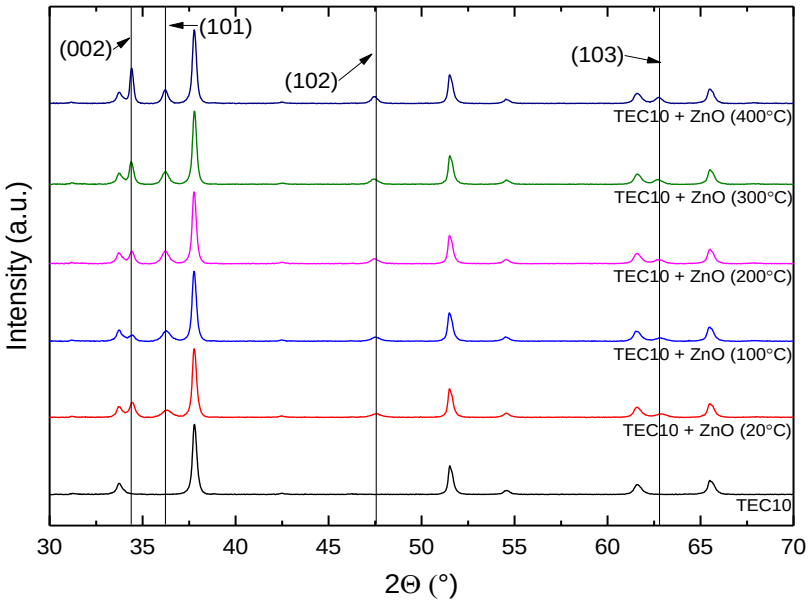

Figure 4.8: The XRD patterns of ZnO films deposited on FTO coated glass at varying substrate temperature

position moves further away from the reference peak at higher deposition temperatures. Fig.4.6 shows the stress build-up at the TCO/ZnO interface for a ZnO deposited at 20 °C. Use of higher temperature assists the ZnO structure to adjust to the underlying semiconductor, shifting the XRD peaks to lower 2Θ angles. The peak shift towards lower diffraction angles is however generally related to compressive stress formation along the relevant diffraction planes. The FWHM of the peaks is reduced for films deposited at higher temperature, which is hence associated with improved crystallite growth.

4.4.3 Optical characterization

Fig. 4.9 shows the transmission curves of FTO coated glass with ZnO deposited at the different temperatures. The mean transmittance calculated over the wavelength range from 400 nm and 950 nm was 80% for all samples other than the room temperature sample which has a marginally lower transmission. The maximum "available" J_{SC} was modelled using Matlab (see chapter 3 for the methodology description) and results (Fig. 4.4) highlighted that a substrate temperature of 100°C is sufficient to achieve such an improvement, while further increase in temperature does not cause any benefit from an optical point of view. Most transparent films have similar optical performance of films

Table 4.3: XRD Peak position and FWHM values for ZnO films deposited at different deposition pressures

Peak	Parameter	Substrate Temperature (°C)				
		20	100	200	300	400
(002)	2θ (°) [ICDD:34.74]	34.44	34.39	34.42	34.40	34.42
	FWHM (°)	0.39	0.42	0.33	0.29	0.24
(101)	2θ (°) [ICDD:36.80]	36.32	36.28	36.23	36.23	36.22
	FWHM (°)	0.60	0.53	0.47	0.43	0.35
(102)	2θ (°) [ICDD:48.10]	47.57	47.54	57.48	47.46	47.47
	FWHM (°)	0.73	0.64	0.58	0.55	0.46
(103)	2θ (°) [ICDD:63.20]	62.86	62.82	62.74	62.70	62.74
	FWHM (°)	0.67	0.56	0.56	0.51	0.49

analysed in the previous section.

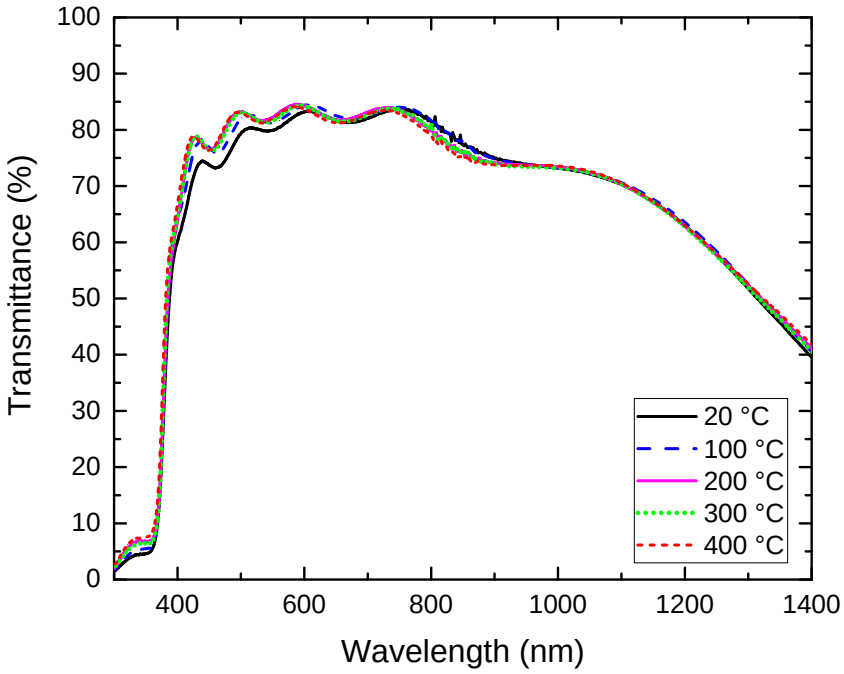

Figure 4.9: The transmission plots of ZnO films deposited on FTO coated glass at different deposition pressures

Table 4.4: The table presents the maximum J_{SC} of a device depending on the transmittance of the FTO/ZnO bilayer. The column named "no filter" shows the potential J_{SC} if all the photons of the AM1.5G spectrum without any filtering, i.e. if all incoming photons would be available to the active layer of the solar cell.

Sample	no filter	20 °C	100 °C	200 °C	300 °C	400 °C
J_{SC} (mA/cm^2)	33.7	26.1	26.5	26.5	26.4	26.4

4.4.4 Electrical characterization

The resistivity of ZnO films deposited on SLG glass at different substrate temperatures has been measured by the Van der Pauw method (Fig.4.10). Films deposited at 100 °C produced the lowest resistivities of 1.87 x 10^{-2} Ωcm, whilst a temperature of 300 °C yielded ZnO films with the highest resistivity of $2 \cdot 10^{-1}$ Ωcm, an order of magnitude difference. The resistivity reported here is relatively low compared to those in other studies where the optimal resistivity was found to be above 10^3 Ωcm and higher [62, 74, 63]. The influence of the ZnO layer on the electrical properties of the TCO was also investigated. The sheet resistance of FTO coated glass was found to be 9.6 Ω/□. The same measurement was repeated on ZnO films deposited on the TCO-coated glass, and the thickness of the ZnO films was kept at 150 nm. The measured sheet resistance showed only minor variation, with all samples giving similar sheet resistances to that of FTO on its own. Samples with the ZnO layer deposited at 100 °C, 200 °C, 300 °C gave a slightly lower sheet resistance (9.5 Ω/□) while the sample deposited at 400 °C gave a slightly higher sheet resistance of 9.7 Ω/□. These differences could be due to non-uniformity of the conductivity of the TCO itself.

4.4.5 CdTe solar cells

Current density-Voltage (J-V) characteristics of each device were obtained and the mean J-V parameters are summarized in Fig. 4.11. The mean short circuit current density (J_{SC}) ranges from 21.2 mA/cm^2 to 21.8 mA/cm^2. The minimal difference in J_{SC} is expected given the similar transmittance of the films. The mean FF increases constantly with increased ZnO deposition temperature, from 65% to 69%, with the exception of the 200 °C

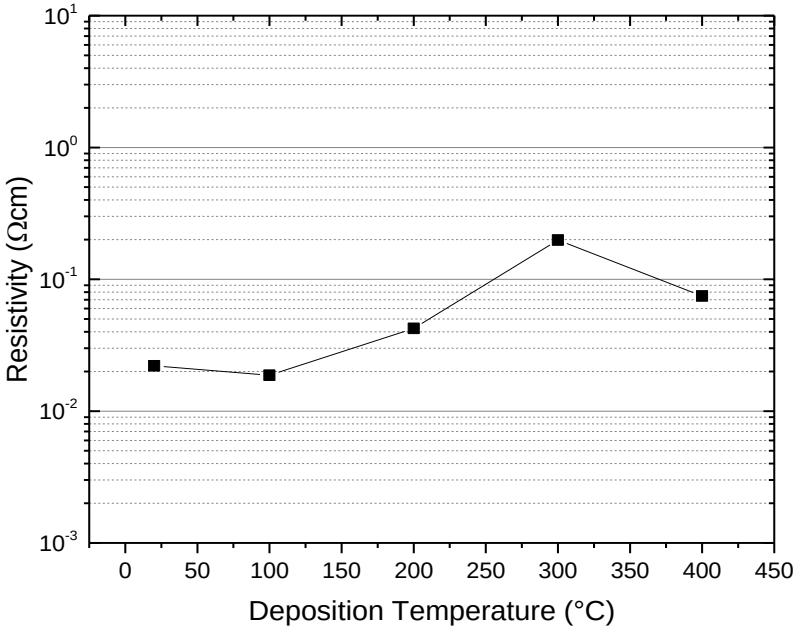

Figure 4.10: The variation of resistivity of ZnO films deposited at different substrate temperature

sample. This increase in FF follows the improvement in crystal structure and the increase in resistivity. The FF may improve due to a combination of an improved TCO/ZnO interface, improved growth of the ZnO crystal structure and increasing resistivity of the ZnO buffer layer. There is no clear trend between the film resistivity and any particoular device parameter, however. The Voc steadily degrades as the ZnO deposition temperature increases, reducing by 23 mV from 798 mV to 775mV, in contrast to the trend for FF. Overall, the mean device efficiency improves marginally from 11.2% to 11.5%. It is likely that a more pronounced trend on the effects of a ZnO HRT layer on a CdTe device will be observed when the CdS layer thickness is thinned below 100 nm. The relatively thick CdS layer used in this study (120nm) is thought to partially screen the ZnO effect [26].

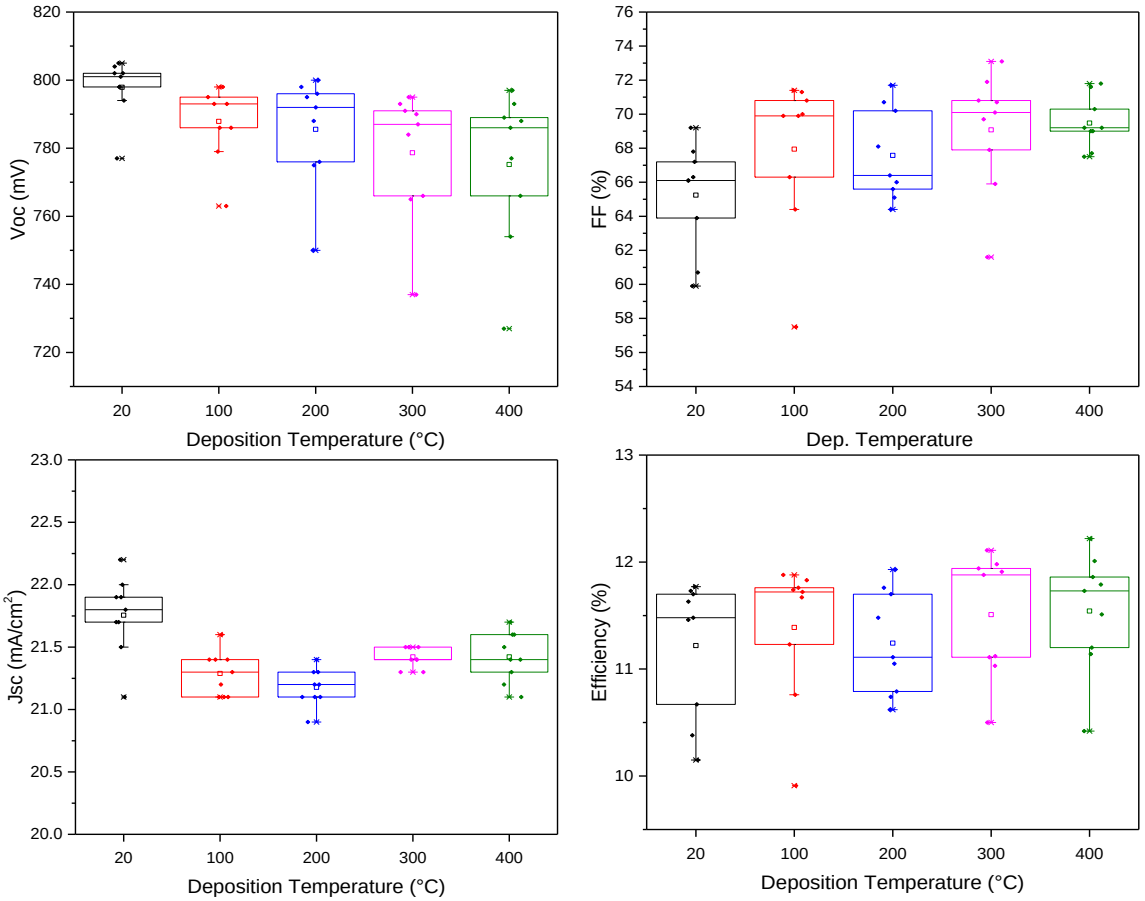

Figure 4.11: The efficiency, open circuit voltage, fill factor and short circuit current density of devices containing ZnO films sputtered at different substrate temperature

4.5 The impact of O_2 content in the sputtering atmosphere

ZnO films were deposited at O_2/Ar ratios in the sputtering atmosphere ranging from 0 % (no oxygen) to 1 %. This range of O_2/Ar ratios allowed yielding films with higher resistivity than those obtained by raising the sputtering pressure, as depicted in the first result section of this chapter. The average baseline pressure in the deposition chamber was 3 x 10^{-7} Torr. The power and pressure were kept constant at 180 W (3.95 W/cm^2) and 1 mTorr respectively. The substrate temperature was 300 °C for all samples. Films XRD patterns and transmittance resulted fairly similar to those presented previously and they will be omitted in this section.

Table 4.5: Sheet resistance measurement of FTO/ZnO bilayers

R_{sheet}	oxygen/argon (%)					
	0	0.2	0.4	0.6	0.8	1
Ω/□	9.6	9.9	9.8	9.7	9.7	9.7

4.5.1 Electrical characterization

The resistivity of ZnO films deposited on SLG at different O_2/Ar ratios was measured using the Van der Pauw method (Fig. 4.12). The increase in resistivity due to higher oxygen content in the sputtering atmosphere follows a logarithmic trend. Film resistivity could be measured up to an O_2/Ar ratio of 0.6%. Above that level, the resistivity became too high to be measured accurately. The resistivity data were given a linear fit and good agreement was found between with the fitted data. The theoretical resistivity of ZnO samples deposited with O_2/Ar ratio higher than 0.6 % was estimated and plotted also in Fig. 4.12. Assuming that the resistivity continues to follow the same trend, the resistivity for the 0.8 % and 1% O_2 samples is estimated to be in the order of 10^6 Ωcm and 1.7 x 10^8 Ωcm, respectively. The resistivity obtained by varying the oxygen partial pressure in the sputtering atmosphere is higher than those achieved by variation of the deposition pressure and substrate temperature. Its influence on the electrical properties of the FTO was investigated. The sheet resistance of both the TCO on its own and of the samples was measured. R_{sheet} of the TCO is 9.6 Ω/□, while R_{sheet} of the FTO substrates coated with ZnO is slightly higher (Table 4.5). The slight increase of R_{sheet} does not correspond to the increase of resistivity obtained when adding oxygen during ZnO deposition, compared to when the ZnO is deposited on bare glass. As found previously, an increase in the resistivity of the ZnO layer deposited on top of FTO was not found to significantly change the conductivity of the bilayer.

4.5.2 CdTe solar cells

For this study the thickness of the CdS layer was reduced to ≈70 nm because, following what found in previous sections, a thinner CdS might help highlighting the effect of the ZnO HRT layers. The performance of devices is summarized in Fig.4.13. The V_{OC} was

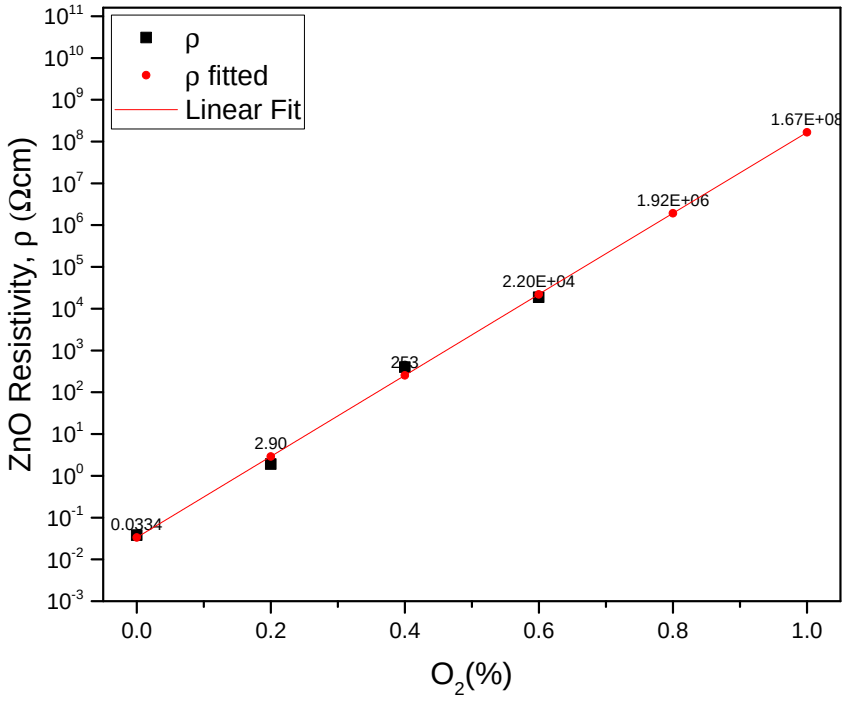

Figure 4.12: The variation of resistivity of ZnO films deposited at different oxygen/argon ratio measured by Hall effect method

higher for devices including ZnO deposited at a oxygen concentration between 0 % and 0.4 %. The mean V_{OC} of these samples averages around 670 mV while for the others is around 630 mV. The best mean V_{OC} was obtained with ZnO deposited with 0.4 % of O_2 (681 mV) and lowest with 1 % of O_2 (625 mV).

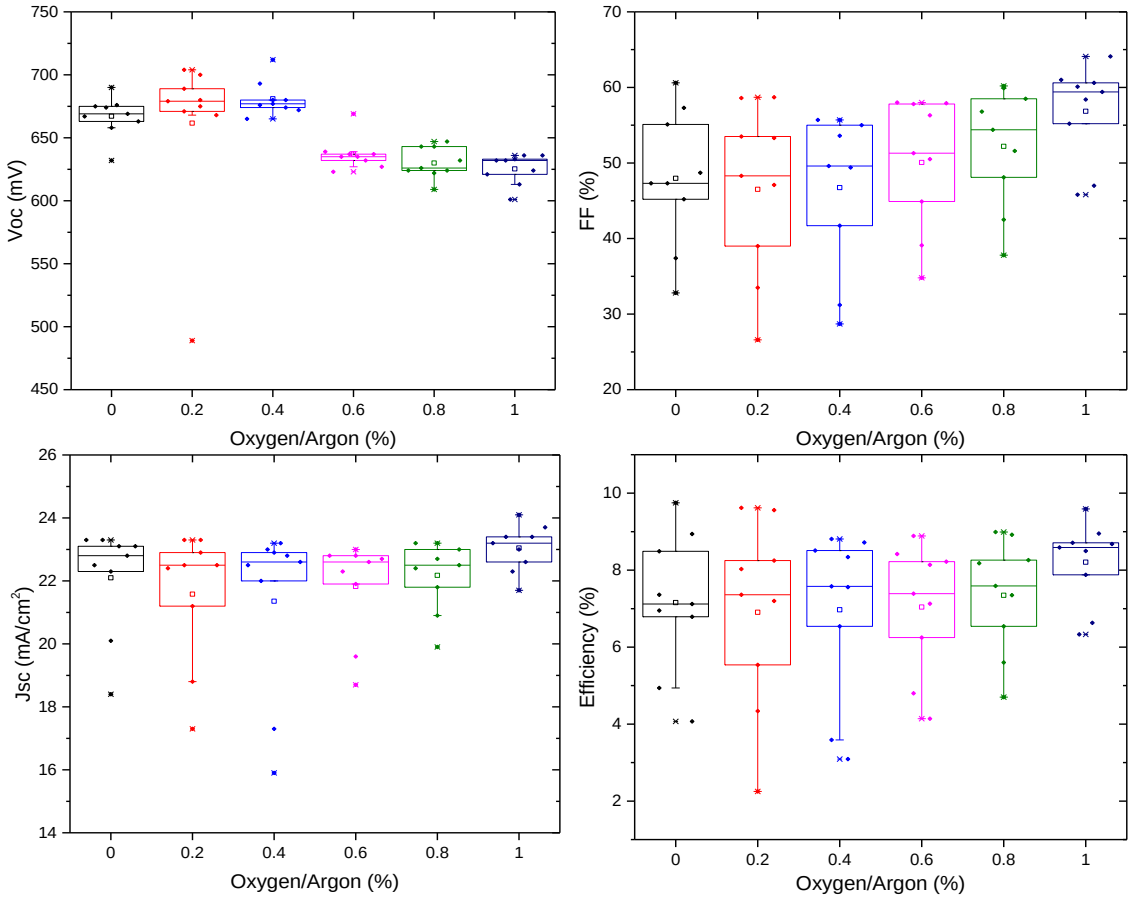

Figure 4.13: The efficiency, open circuit voltage, fill factor, and short circuit current density of devices containing ZnO films sputtered with different oxygen concentrations in the sputtering atmosphere

The Voc of these samples is significantly lower than the one of the samples described in the previous chapters (≈ 800 mV). This is due to the thinning of the CdS layer. Moreover, no process of optimization has been carried out for devices including a thin CdS , therefore the results should be interpreted relative to each other. The FF benefits of oxygen concentration above 0.4 %: samples deposited with a oxygen concentration between 0 % and 0.4 % have FFs of ≈ 47 % while for higher O_2 concentrations the FF increases up to a maximum of 57 % at 1 % O_2 content, which is a significant improvement. The mean FF is also worse than that found for previous samples because of the thinning of the CdS layer. A similar trend was found for the short circuit current density J_{SC} where the addition of oxygen was most beneficial at 0.8 % and 1 % O_2 content. The maximum mean J_{SC} is 23 mA/cm^2 compared to the 22 mA/cm^2 in the sample deposited with no O_2

in the sputtering gas. The maximum mean Jsc achieved is higher than that obtained with a thicker CdS (section 4.3.4 and 4.4.5), which is likely related to the decreased absorption losses due to a thinner CdS layer. The addition of oxygen in the sputtering atmosphere during the deposition of ZnO HRTs was beneficial for device efficiency. At an oxygen concentration of 1%, a significant increase in mean efficiency was obtained. The improvement was achieved through FF and J_{SC} increase. While oxygen addition was followed by an increase of resistivity of ZnO films, there is no clear evidence that the improvement in efficiency is related to the resistivity itself.

4.6 Discussion of the results

In the previous sections the performance of several devices was analysed. It was observed that the mean device V_{OC} and FF had consistently alternating trends: whenever one of the two parameters is improving due to the varying deposition conditions of the ZnO HRTs, the other one degrades. An explanation of this phenomena could not be found in literature. A hypothesis raised in section 4.4.5 relates this mechanism to the CdS/ZnO junction properties or, in other words, the amount of interface defect states. In order to investigate what effect these interface defects might have on the devices, modelling was carried out with SCAPS. SCAPS is a PV simulation software allowing for simplified modelling of 2-dimensional PV structures. A baseline structure was prepared as a starting point for simulations. The parameters of the baseline are represented in Table 4.6. Parameters have been taken from commonly used values [75] and values used to simulate CdTe thin film solar cells produced at the Colorado State University photovoltaic research centre [76]. Moreover values of CdS shallow acceptor density and parameters relative to interface defects at both ZnO/CdS and CdS/CdTe interfaces were optimized to create a structure yielding similar performance to real devices. The JV plot and main performance parameters of the simulated baseline structure device are available in Fig. 4.14 and the J-V characteristic of a representative cell added to the figure as a comparison. The ZnO/CdS interface properties were modified using the batch calculation function in SCAPS. This function allows a step by step variation of a defined parameter within a certain range.

Table 4.6: The baseline parameters used for SCAPS simulations. Parameters presented in table that needs defining are: the permittivity (ε), the dielectric constant (ε_0), the effective density of states for electrons in the conduction band (Nc), the effective density of states for holes in the valence band (Nv), the electron mobility (μ_e), the hole mobility (μ_h), the electron and hole lifetime (T_n,T_p), the density of defect states (N_t), the defect energy (E_t) and the electron and hole capture cross-section (σ_e,σ_h).

Parameter	**FTO**	**ZnO**	**CdS**	**CdTe**
x (nm)	400	150	120	2400
Eg (eV)	3.6	3.3	2.4	1.5
X (eV)	4.8	4.8	4.5	4.4
ε / ε_0	9	8.5	10	9.4
N_C (cm^{-3})	2.2 x 10^{18}	2.2 x 10^{18}	2.2 x 10^{18}	8 x 10^{17}
N_V (cm^{-3})	1.8 x 10^{19}	1.8 x 10^{19}	1.8 x 10^{19}	1.8 x 10^{19}
μ_e (cm^2/Vs)	9	8.5	100	320
μ_h (cm^2/Vs)	25	25	25	40
T_n, T_p (ns)	0.1	0.1	0.1	0.7
n or p (cm^{-3})	2.35 x 10^{21}	1 x 10^{17}	4.26 x 10^{16}	2 x 10^{14}
Defect States				
N_t (cm^-3)	D:10^{15}	D:10^{15}	A:10^{18}	D:8^{13}
E_t (eV)	midgap	midgap	midgap	midgap
σ_e (cm^2)	1 x 10−12	1 x 10−12	1 x 10−17	8 x 10−13
σ_h (cm^2)	1 x 10−15	1 x 10−12	1 x 10−12	8 x 10−13
Interface Defect States				
	ZnO/CdS		CdS/CdTe	
N_t (cm^-3)	6.31 x 10^{10}		10^{11}	
E_t (eV)	1.2 eV (above highest E_V)		0.4 eV (above highest E_V)	
σ_e (cm^2)	10^{-13}		9 x 10^{-15}	
σ_h (cm^2)	10^{-13}		9 x 10^{-15}	

Simulations have been carried out for varying concentrations of interface defects at the ZnO/CdS interface. The defects lie energetically in the middle of CdS energy band gap.

Results obtained in simulations showed that a linear variation of the defect density at the ZnO/CdS interface can have an opposite effect on V_{OC} and FF. The energy band diagram of the structure has been simulated at 3 different interface defect densities. Results represented in Fig. 4.16 show that a variation of the amount of defect states can affect the hole Fermi energy distribution in the CdS layer: (highlighted in the figure by a red rectangle). As a result the change in free carrier distribution within the CdS layer causes a change in the SRH recombination through mid-gap defects of the CdS layer, as highlighted in Fig. 4.17. In particular SRH recombination decreases when the concentration of defects at the ZnO/CdS interface is higher, which is counter-intuitive. The reduction of the SRH recombination translates in a decreased saturation current and as a consequence a improvement of the device V_{OC}. On the other hand, the higher defect density at the interface can be an obstacle the free carrier diffusion increasing the series resistance of the device. The series resistance of the devices has been extrapolated using a Lambert-W function fitting method of the one-diode model detailed by Zhang and colleagues [61]. The mean FF and V_{OC} of devices was plotted in relation to the correspondent R_S. What was found is that generally devices with higher FF and relatively lower V_{OC} have in turn a lower series resistance, and vice versa. This supports the idea that a higher defect density at the ZnO/CdS interface can increase the series resistance of the device and as a consequence can affect the FF.

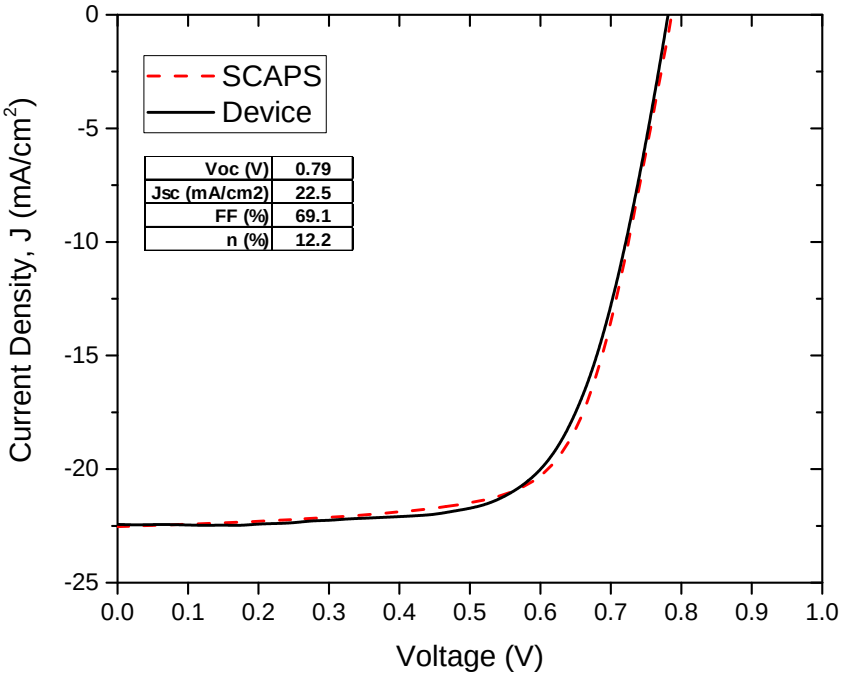

Figure 4.14: In black the I-V characteristic of the baseline structure set up with SCAPS. In red the I-V plot of a representative real device. Performance parameters of the SCAPS baseline are provided within the graph.

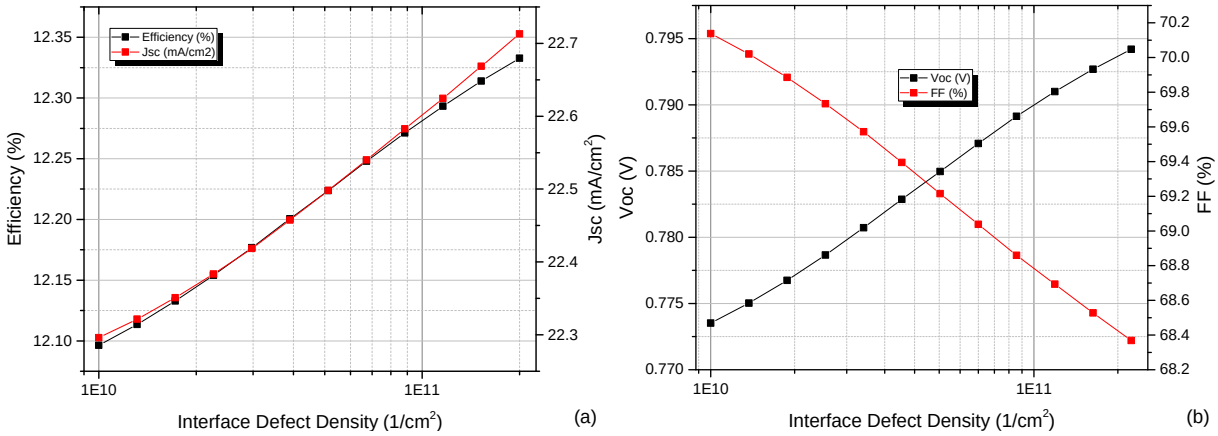

Figure 4.15: The simulated effect of an increasing concentration of mid-gap defects at the ZnO/CdS interface on (a) efficiency and J_{SC} and (b)V_{OC} and FF.

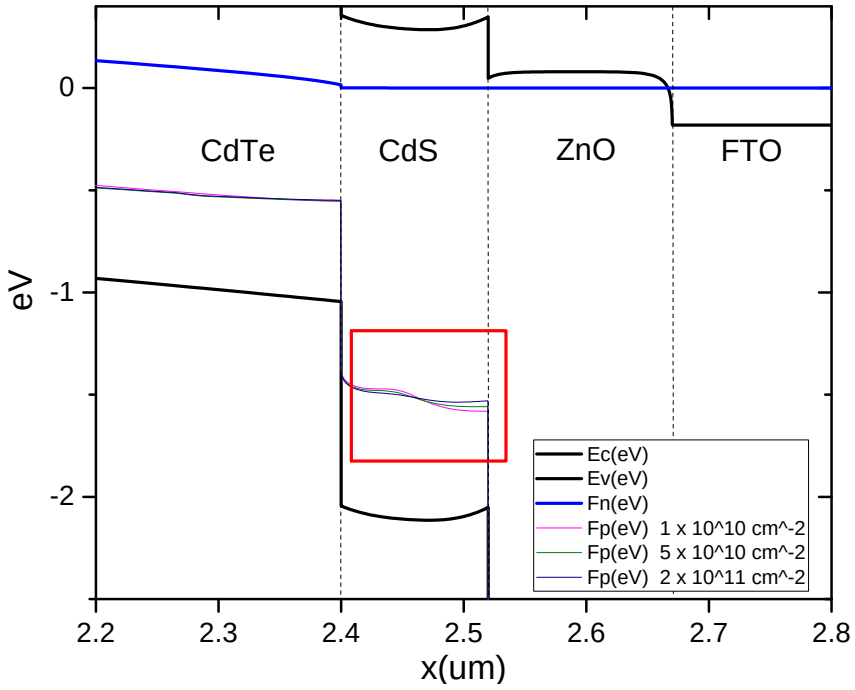

Figure 4.16: The simulated energy band diagram of the baseline structure at three different donor-type ZnO/CdS interface defects. Highlighted in red the region within the device where the Fermi energy level for holes slightly varies.

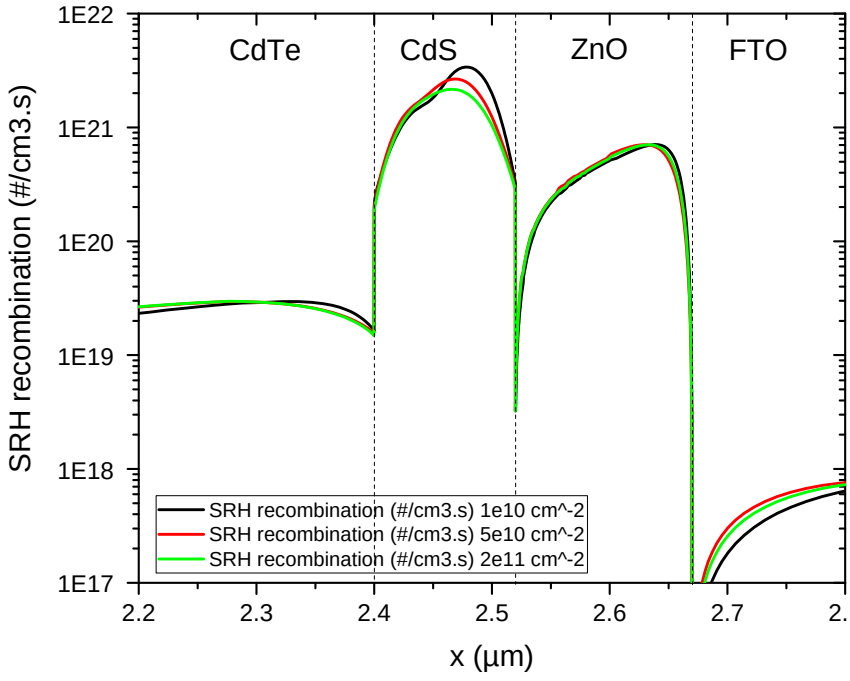

Figure 4.17: The simulated SRH recombination frequency at three different donor-type ZnO/CdS interface defects.

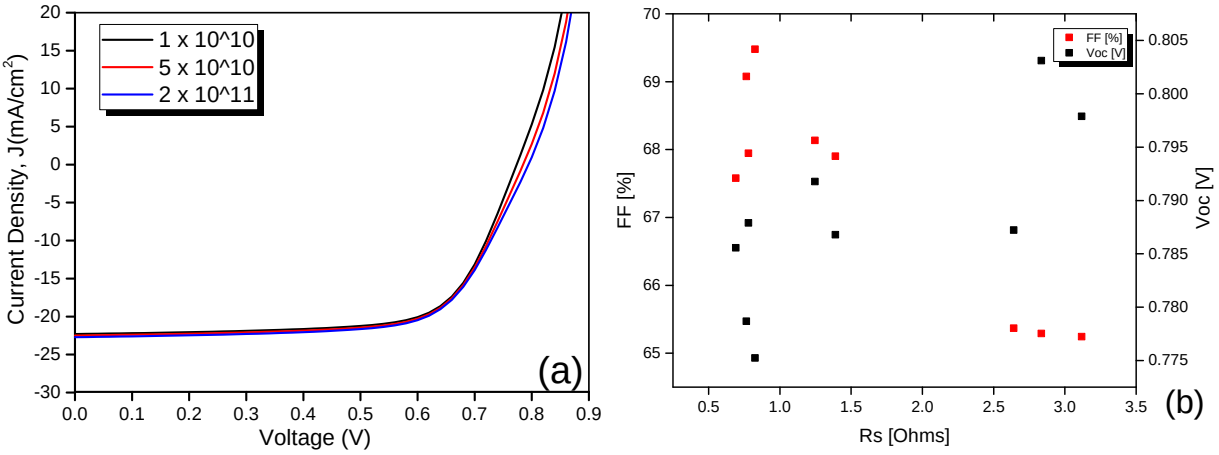

Figure 4.18: (a) Simulated J-V plots for device with different concentration of interface defects at the ZnO/CdS interface and (b)the relationship between the mean series resistance of devices and their mean open circuit voltage and fill factor.

4.7 Conclusions

In this work we investigated the effect that structural, optical and electrical properties of ZnO HRTs have on the performance of CdTe thin film solar cells. All these properties were altered by changing the sputtering conditions. It was found that very low and high deposition pressures (avoiding intermediate sputtering pressures between 5-7 mTorr) and sputtering temperatures above 100 °C causes a gain of ≈ 2% in the average transmittance in the wavelength range 400 nm - 950 nm of ZnO films. It was noticed that temperature assisted the crystal and the grain growth of the ZnO HRTs. This structural improvement was followed by a significant improvement in FF of devices. The addition of oxygen during ZnO sputtering was found to be beneficial. A higher O_2/Ar ratio had the consequence of increasing the resistivity of films. Oxygen addition had the main effect of improving device FF. A significant improvement in FF and J_{SC} was obtained at 1% of O_2 concentration in argon, however the improvement does not share any clear trend with film resistivity and no evidence to support the "pinhole" theory was found in this study. It seems also very difficult to relate any of bulk parameter taken into account, to the device performance. By exclusion, it is suggested that it might be the interface chemistry/properties modification caused by the variation of the deposition conditions of ZnO films to be affecting in this case the CdTe solar cells performance. Using SCAPS it was simulated the effect that a

different amount of interface mid-gap defects at the ZnO/CdS interface can have on the performance of a CdTe device. Simulation results showed that an increased concentration of interface defects can affect the Fermi energy level distribution within the device and as a result decrease the SRH recombination within the CdS layer. This phenomenon can be linked to the anti-correlate behaviour of the Voc and FF. In parallel the increased concentration of interface defects increases the series resistance of the device degrading its FF. As a consequence of this two phenomena, a decreased number of ZnO/CdS interface defects can cause the degradation of V_{OC} while improving FF and vice versa for the opposite case.

Chapter 5

Magnesium-doped Zinc Oxide

5.1 Introduction

There are several studies highlighting the importance of controlling the alignment between the band levels of absorber and window layers in chalcogenide solar cells [77, 78, 55]. These emphasize the importance of a slightly positive conduction band at the buffer/absorber interface to control the inversion of the absorber and recombination at the interface. The ZnO/CdS interface has previously been analysed by photoelectron spectroscopy (XPS and ultraviolet photoelectron spectroscopy) and it has been estimated that the valence band offset between the two semiconductors is $\Delta E_{VB} = 1.2$ eV [79, 80]. The energy band gap of CdS and ZnO is 2.4 eV and 3.3 eV respectively [81, 66, 82], thus leading to a conduction band offset of approximately 0.3 eV with the ZnO conduction band being lower than the CdS conduction band. Following what is stated in chapter 2 this is not a favourable band alignment. Doping ZnO with MgO ($E_G = 7.7$ eV) leads to an energy band gap increase through the formation of $Zn_{1-x}Mg_xO$ (MZO)[83]. The increase depends linearly upon the Mg content in the film, up to a Mg content of x = 0.46, at which point the band gap is $E_G = 4.2$ eV [84]. Experimental determination of the band alignment of MZO indicates that the larger band gap of MZO is almost exclusively due to an upshifting of the conduction band energy level [85, 80]. A similar behaviour occurs when ZnO is doped with Ca rather than Mg [86, 87]. In the range x = 0 to x = 0.46 $Zn_{1-x}Mg_xO$ maintains the typical hexagonal structure of ZnO while above this doping level there is a gradual transition to the cubic structure of MgO [84]. The first applications

of MZO were reported with copper indium gallium selenide (CIGS) thin film solar cells [88, 89, 90, 91, 92, 93, 94, 95], where MZO was used as a replacement for the CdS buffer layer. The successful application of magnesium-doped zinc oxide to CdTe thin film solar cells has been recently reported[76]. Other semiconductors have been investigated for the tunability of their energy band structure (CdS:O, ZnS, Zn(O,S) [56, 96, 97, 98, 99]). The first part of the work presented in this chapter was focused on using MZO as an HRT layer with an emphasis on the effect of changing its conduction band alignment with the adjacent semiconductors. To date, studies have achieved band gap variation by using targets with different compositions. In this work instead the band gap of MZO was tuned by modifying the substrate temperature during the sputtering deposition. The investigation of the effect of band alignment of the HRT layer within the solar cell can also be considered novel. A similar theoretical investigation was carried out by Kephart [76] by simulating the effect of HRT electron affinity. Results presented in this chapter follow these simulated results. Finally, the use of MZO as an intermediate layer between TCO and CdS was also proven for the first time. While the utilisation of MZO as an HRT layer has been effective, it did not completely eliminate the optical losses due to the small band gap of the CdS layer. The second part of this chapter focuses on the complete elimination of the CdS buffer layer. This achievement allowed an increase in the current density output and efficiency of the CdTe devices without Voc and a FF degradation.

5.2 Magnesium-doped Zinc Oxide as a High Resistance Transparent Layer for thin film CdS/CdTe solar cells

5.2.1 Methodology

Tin-doped indium oxide and magnesium-doped zinc oxide thin films were deposited by Radio-Frequency (RF) magnetron sputtering. Soda lime glass (SLG) was used as superstrate. The glass cleaning technique is described in chapter 3. Thin films were deposited using an Orion 8 HV magnetron sputtering system (AJA international, USA) equipped

with an AJA 600 series RF power supply. The 3" diameter ITO target contained 10 % SnO_2 and 90 % In_2O_3 (Wt %). The 3" diameter MZO target contained 11 % MgO and 89 % ZnO, (Wt %). The glass superstrates were rotated at 10 rpm during deposition to enhance the uniformity of the films. The sputtering process was carried out at a constant power density of 3.5 W.cm^{-2} and at a pressure of 133.3 Pa using Ar as the working gas. The sputtering deposition of MZO films was carried out in a 1 % O_2 in an Ar atmosphere. The temperature of the superstrate was kept constant at 450 °C for the deposition of ITO and ranged from 20 to 400 °C for MZO. The optical properties were investigated using a Cary Varian 5000 UV-VIS-NIR spectrophotometer. The films surface elemental composition of the films was measured using an X-ray photoelectron spectrometer (XPS) (Thermo Scientific K-alpha). Samples were processed into complete CdTe solar cells in the laboratories of University of Verona. ITO/MZO superstrates were coated with CdS and CdTe by thermal evaporation. The deposition process was carried out in a vacuum chamber at a pressure of 10^{-4} Pa with a Edwards XDS10 roughing pump and a Edwards ST-451 turbo-molecular pump. CdS was evaporated from a tungsten crucible at a deposition rate of 0.15 nm/sec. During deposition the substrate temperature was kept at 100 °C using halogen lamps. Before and after CdS deposition, the stack was annealed in vacuum at 450 °C for 30 minutes. CdTe was deposited from a graphite Knudsen cell with an evaporation rate of 40 Å/sec. The deposition rate was monitored using an Intellemetrics IL-150 quartz controller. The CdTe activation treatment was performed using a $CdCl_2$ wet treatment. The solution was prepared by dissolving the $CdCl_2$ powder in methanol to form a saturated solution. The $CdCl_2$ powder was dried in a furnace at 0.1Pa before processing in solution. Typically, ≈250 μl was deposited in form of drops on the CdTe surface. The stack was then annealed in air at 380 °C for 30 minutes after a 15 minutes ramp from room temperature. Prior to back contact formation, the CdTe surface was treated with a solution of bromine (50 μl) and methanol (50 ml). This process removed residual $CdCl_2$ and etched the CdTe surface forming a Te-rich layer. Subsequently, a 2 nm thick layer of Cu and a 50 nm thick layer of Au were deposited by thermal evaporation at room temperature in a vacuum of 10^{-3} Pa. The process was finished by annealing the structure for 20 min at 190 °C in air. Devices were characterized using current density-voltage (J-V) characteristics and cross-section images were obtained using transmission

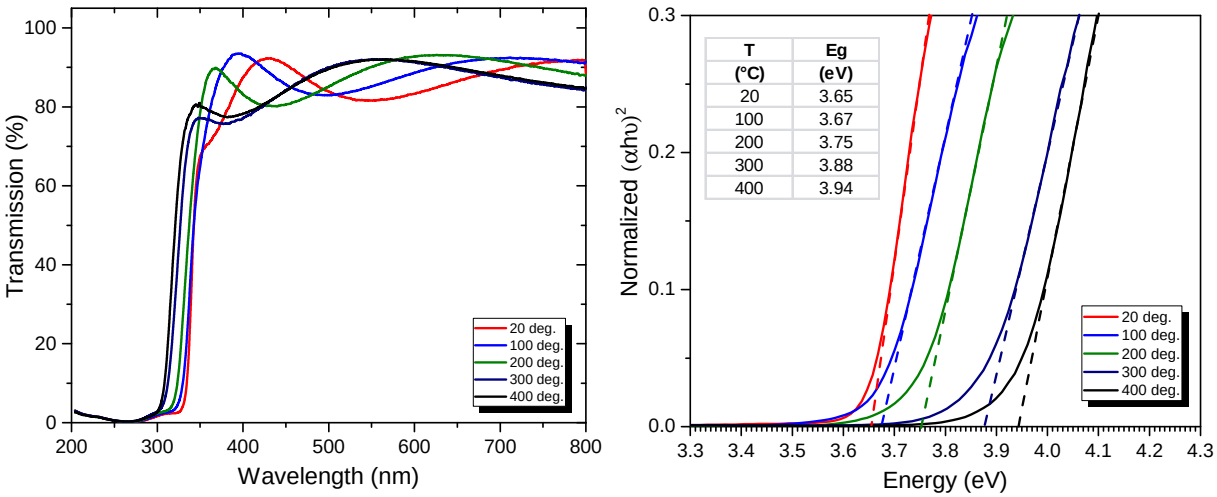

Figure 5.1: (a) The transmittance plots of MZO films deposited at increasing substrate temperature and (b) estimation of energy band gap of the same films using the Tauc Plot technique.

electron microscopy (TEM). Samples for TEM were prepared by focused ion beam milling using a dual beam FEI Nova 600 Nanolab. A standard in situ lift out method was used to prepare cross-sectional samples. An electron beam assisted platinum (e-Pt) over-layer was deposited onto the sample surface above the area to be analysed followed by an ion assisted layer to define the surface and homogenise the final thinning of the samples down to 100 nm. TEM analysis was carried out using a Tecnai F20 operating at 200 kV to investigate the detailed microstructure of the cell cross-sections. Images were obtained using the bright field (BF) detector.

5.2.2 Characterization of Magnesium-doped Zinc Oxide films

Transmission plots of MZO films deposited at increasing temperature are shown in Fig. 5.1(a). The absorption edge shift in the UV region indicates that the band gap of the films varies with the deposition temperature. The band gap of MZO films was estimated using the Tauc plot technique (Fig. 5.1(b)). The energy band gap of MZO films deposited at room temperature was estimated to be $E_g = 3.65$ eV, 0.35 eV higher than that of ZnO. This confirms that doping ZnO with Mg widens the optical band gap of the semiconductor. It was also observed that raising the temperature assists further increase of E_g. E_g increased from 3.65 eV at room temperature to 3.95 eV at 400 °C, similar to what is

previously reported [100].

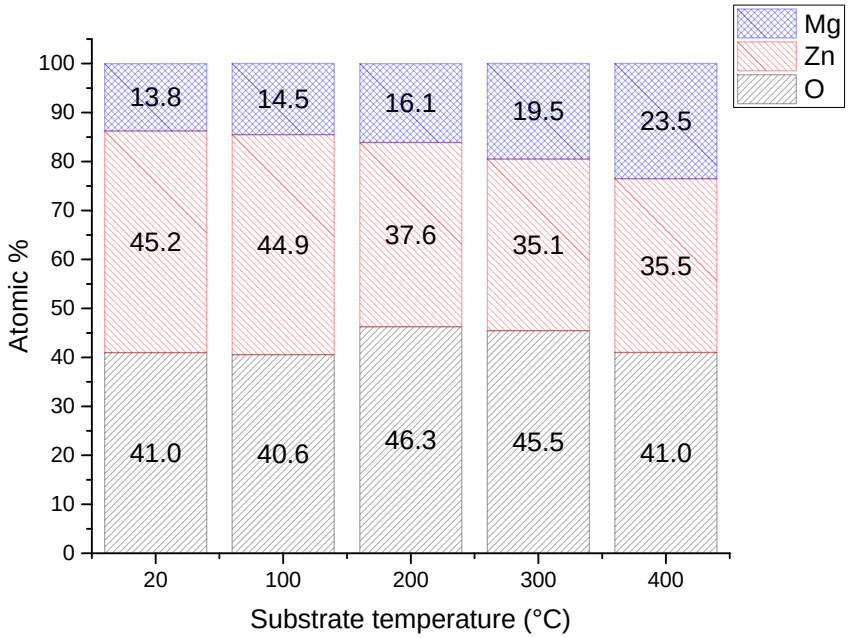

Figure 5.2: The atomic percentage of Mg,ZnO and O_2 in MZO films estimated by XPS analysis.

Table 5.1: MZO films atomic Mg/Zn, Mg/O, Zn/O ratios.

Ratios	Deposition Temperature (°C)				
	20	100	200	300	400
Mg/Zn	0.31	0.32	0.43	0.56	0.66
Mg/O	0.34	0.36	0.35	0.43	0.57
ZnO/O	1.10	1.11	0.81	0.77	0.87

XPS analysis showed that increasing the temperature during MZO film deposition leads to a growing concentration of Mg atoms as shown in Fig. 5.2. The Mg/Zn ratio increases up to 400 °C suggesting that temperature enhances the inclusion of Mg ions in the MZO crystal structure (Table 5.1). The evaporation of Zn or Mg during deposition can have an important role in this process. The vapourization temperatures of Zn and Mg at a pressure of 1 mTorr (used during deposition) are ≈290 °C and ≈380 °C respectively [101]. At 300 °C and 400 °C, the Mg/Zn ratio increases significantly compared to films deposited at lower temperatures possibly because Zn ions evaporate leaving free lattice

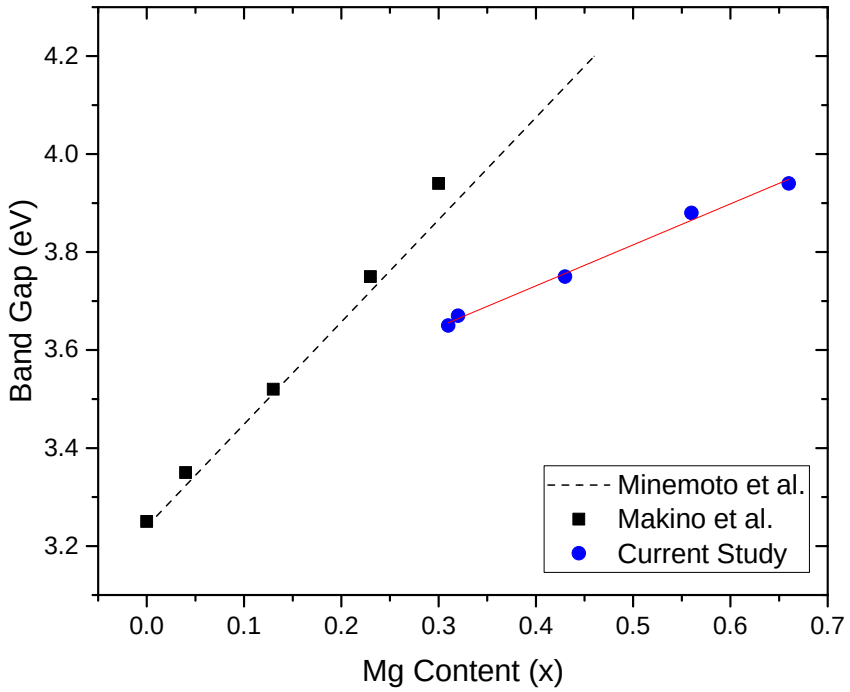

Figure 5.3: The graph represents the relation between film Mg/Zn atomic ratios and their band gap. For comparison purposes, the values extrapolated in previous studies are also represented in figure.

sites for Mg ions to occupy. Up to 200 °C the increasing Mg atomic concentration should not be related to Zn evaporation but to some other mechanism. Hwang et al have reported [100] that increasing the substrate temperature causes a reduction of the Mg elemental content in the films due to Mg evaporation as measured by electron probe microanalysis. This result is opposite to our findings. They also suggested that the increase in optical energy band gap occurs because raising temperature assists the replacement of Zn ions with Mg ions. Our work confirmed that temperature helps Mg ions replacing Zn ions. It was also confirmed that higher film deposition temperatures promote the growth of the MZO films band gap. Unlike what is found in [100], however, the Mg concentration was found to increase by raising the deposition temperature. The band gap dependence of $Zn_{1-x}Mg_xO$ with the Mg content x is linear (Fig. 5.3).

The linear relationship between Mg content and band gap is different than other studies on MZO deposited by RF magnetron sputtering [84] and pulsed laser deposition [102]. Trends extrapolated in these previous studies highlight a steeper band gap widening with the Mg content increase. This phenomenon could be related to the different fabrication

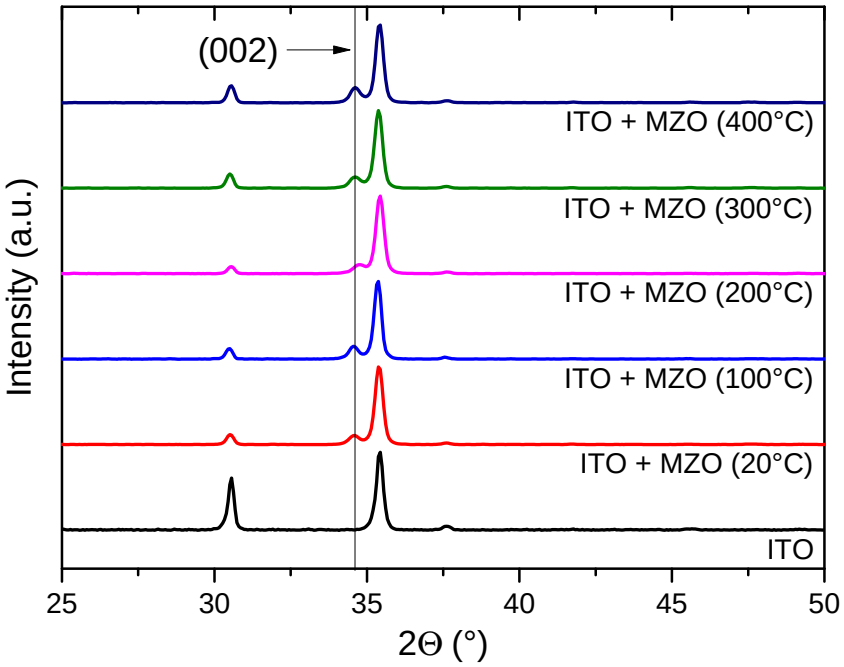

Figure 5.4: The XRD patterns of MZO films deposited at different temperature on ITO.

techniques and conditions of films. It is possible that the method used to vary the film composition affects the type its linear relationship with the band gap. Different mechanism might have occurred in this study, as the deposition temperature was used to increase the films Mg/Zn ratio. Another possibility is that the film composition varies between the bulk and the surface of the film. In this study the compositional values detected by XPS refer to the very first few nm of the film. The crystal structure of MZO has been investigated by XRD analysis (Fig. 5.4). The (002) diffraction peak was observed, and the other peaks are associated with the underlying ITO film. The (002) peak was also observed for ZnO films and is indexed from the crystallographic data of the ZnO hexagonal structure [103]. Peaks (200) and (220) indexed from the crystallographic data of the cubic structure of MgO are not visible [84] (ICDD 00-003-0752). ZnO has a band gap of 3.3 eV and a negative CBO with CdS of -0.3 eV. Room temperature deposited MZO films show a band gap of 3.65 eV. This corresponds to an almost flat conduction band alignment with CdS [80]. Raising the deposition temperature of MZO films increases its band gap up to 3.95 eV at 400 °C. This corresponds to a CBO with CdS of +0.35 eV.

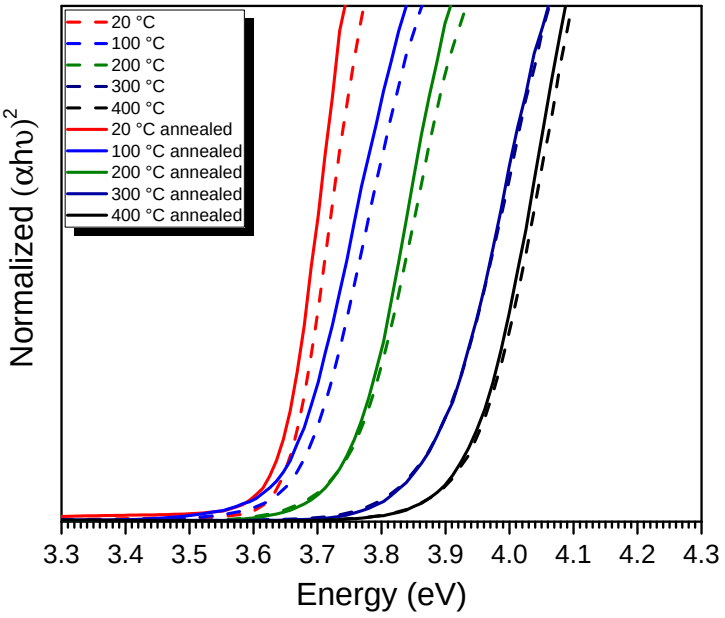

Figure 5.5: Tauc plot of MZO films deposited at different temperatures (dashed lines) and of the same films annealed at 450 °C for 30 minutes (solid lines).

5.2.3 Thermal Stability of MZO

Multiple annealing steps were performed during the fabrication process of thin film CdTe solar cells and the band gap of MZO films are sensitive to the temperature of the substrate during deposition. To test whether the band gap of MZO can change during the fabrication process, a thermal annealing step was carried out at 450 °C for 30 minutes which simulates the annealing step used during the fabrication process. The band gaps of the films were extrapolated using the Tauc Plot technique (Fig. 5.5). The plot reveals the band gap is slightly affected by the annealing step, especially for films deposited at low temperature. However the change is minimal and difficult to quantify precisely with a graphical estimation used in the Tauc method.

5.2.4 CdS/CdTe Solar Cells with MZO HRTs

The MZO films were tested as HRT layers in CdS/CdTe solar cells with the following structure: ITO/MZO/CdS/CdTe/Au back contact. The performance of the devices was significantly affected by the deposition temperature of the MZO HRTs (Fig. 5.6). This suggests that the band gap of the MZO layer is playing a key role within the solar cell.

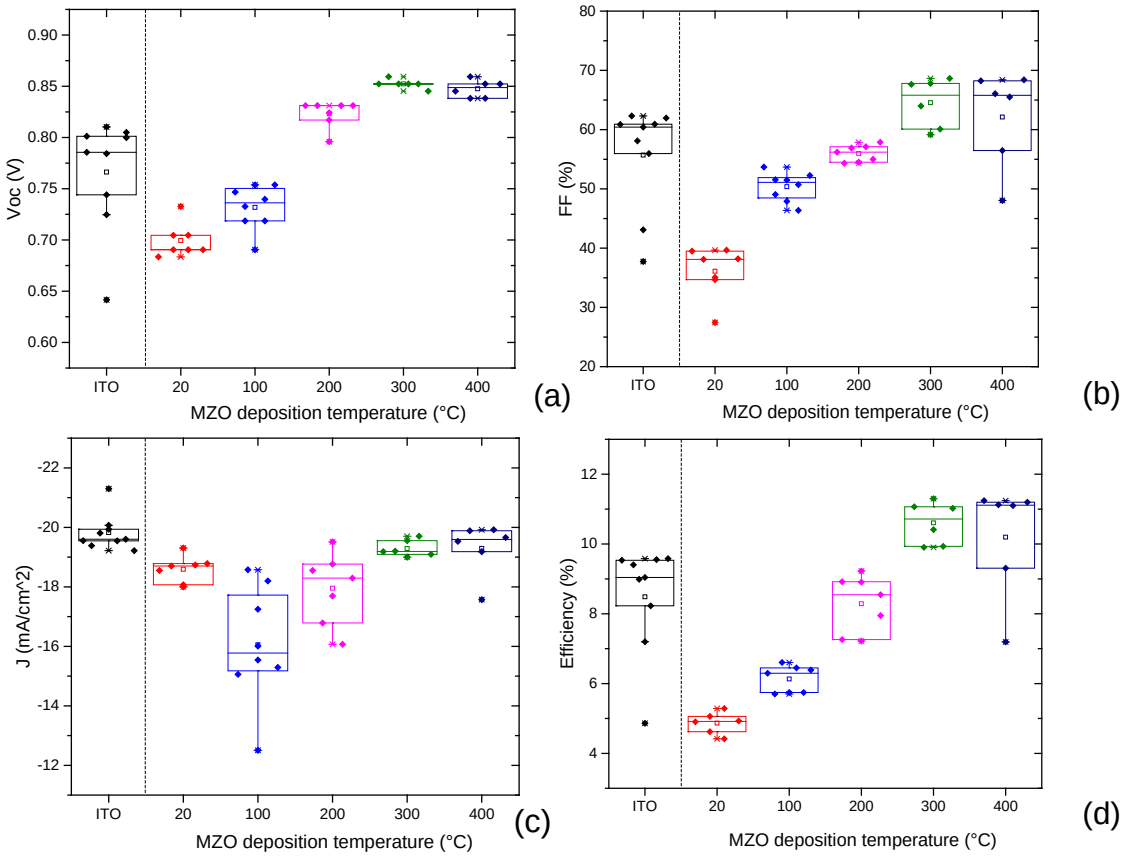

Figure 5.6: Box Plots giving a statistical representation of Voc (a), FF (b), Jsc (c) and efficiency (d) of devices containing MZO deposited at increasing substrate temperature.

The mean device efficiency increases from slightly below 5% with the MZO layer deposited at room temperature, to ≈10.6 % at for a MZO substrate temperature of 300 °C. The higher efficiency is a consequence of improved Voc and FF, which were respectively 0.82 V and 66% compared to 0.7 V and 36% for MZOs deposited at RT. Temperature has a detrimental effect on Jsc at 100°C while a further increase of temperature gradually improves the current density which reaches a maximum at 300 °C and 400 °C (≈20 mA/cm^2). CdTe devices not incorporating MZO HRT layers were fabricated and results have been compared. Efficiency, Voc and FF all benefit from the addition of MZO deposited at high temperature. The highest current densities achieved with MZO are similar to those achieved without the layer indicating that the high transparency of the films deposited at high temperature does not greatly affect device Jsc.

5.2.5 Quantum efficiency, TEM and EDX analysis

The EQE of the highest performing device, with an MZO layer deposited at 400 °C is shown in Fig. 5.7. The absorption edge in the near infra-red (NIR) region lies at 850 nm, which corresponds to the CdTe absorber band gap of 1.45 eV [14]. Whilst the device performance improves with the MZO deposition temperature thanks to improved Voc and FF, the current density is limited by the high absorption in the blue region of the CdS layer. It is clear that to improve the device further, a reduction of thickness of the CdS layer is required. This would lead to higher photocurrent density generation in the device. TEM images of the cross-section of the sample show the layer by layer microstructure of the solar cell (Fig. 5.8). The thickness of the CdS layer has been estimated from the images to be in the range 250 nm - 300 nm, sufficiently thick to absorb most of the radiation in the blue visible region. The CdTe layer is ≈ 7 μm in thickness and its grains develop across the full thickness of the layer.

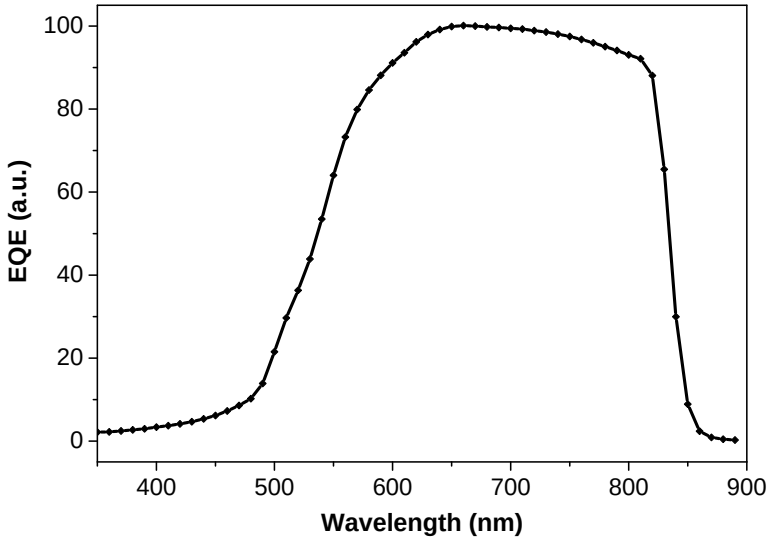

Figure 5.7: The EQE spectra of a ITO/MZO/CdS/CdTe solar cell with MZO Eg = 3.88 eV.

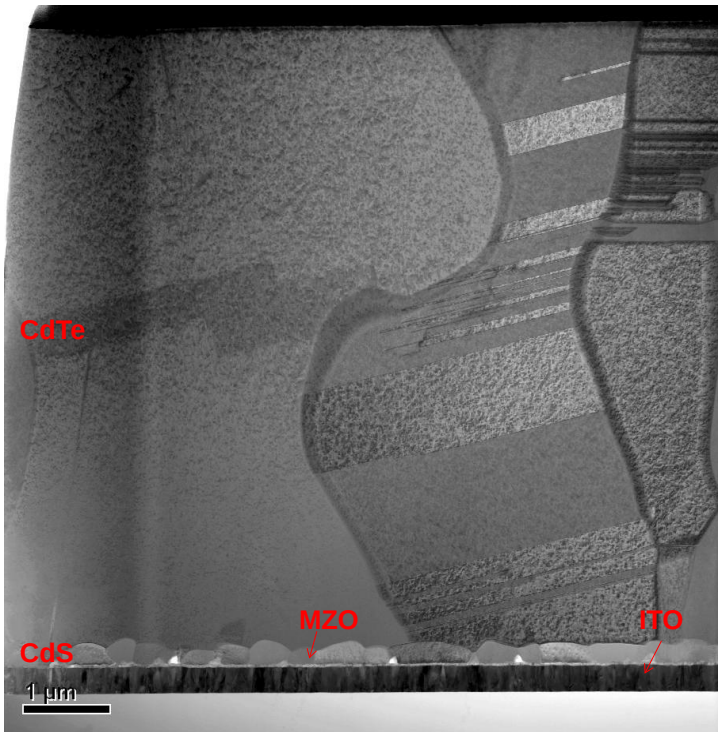

Figure 5.8: The TEM cross-section of a CdTe device with the FTO/CdS/MZO/CdTe structure.

5.2.6 Temperature-Dependent Current/Voltage Measurements

The temperature dependent I-V measurements (I-V-T) helps to establish which type of recombination is dominating in the device. In CdTe thin film solar cells, the recombination rate at the interface is proportional to the hole concentration. The concentration of holes at the interface is given by eq:

$$p = N_v exp(\frac{qV - \phi_b}{kT}) \tag{5.1}$$

where N_v is the valence band density of states and $\phi_b = E_{fn} - E_v$ (where E_{fn} is the electron Fermi level at the interface) is the potential barrier height at the interface which is equivalent to the activation energy of the interface recombination. Bulk recombination happening in the space charge region or in the neutral region is on the other hand activated by the band gap energy E_g. The activation energy was extraplated by analysing the temperature dependence of device V_{oc}. The methodology used for the calculation is explained in [104, 105]. The theory states that if the estimated activation energy is lower

Table 5.2: The dependence between the MZO film deposition temperature, the film band gap, the conduction band offset between at the MZO/CdS interface and the recombination activation energy.

Dep. Temperature (°C)	Eg (eV)	MZO/CdS ΔEc (meV)	Ea(eV)
20	3.65	50	1.23
100	3.67	70	1.25
200	3.75	150	1.42
300	3.88	280	1.52
400	3.94	340	1.57
ITO	-	-	1.54

than the band gap energy of the absorber layer, the buffer/CdTe interface recombination is dominant, while if the activation energy is equal than the CdTe E_g it is the CdTe bulk recombination dominating. The estimated activation energy E_a varied depending on the MZO film deposition temperature and its band gap (Table 5.2). Devices containing MZO layers deposited at room temperature (band gap of ≈3.65 eV) yield an activation energy of 1.23 eV. The activation energy then grows with the MZO film band gap up to 1.57 eV obtained with MZOs deposited at 300 °C, which is higher than the CdTe band gap. This suggests that the main source of recombination within these devices is neither bulk recombination nor the CdS/CdTe interface recombination. Due to the strong dependency between the MZO band gap and the recombination activation energy it is hypothesised that it is rather the recombination at the MZO/CdS interface to be dominant. This could be possible in the case of a poorly inverted absorber. Further investigation is required to improve the understanding of this mechanism. This result seems to indicate that the Voc and FF improvement could be related to a diminished interface recombination, although it is still not clear whether this reduction happens at the MZO/CdS interface, since it is between those two layers that the band alignment is changing, and/or at the CdS/CdTe interface.

Sheer et Al cell [106] simulated the effect of interface states in a heterostructure solar cell. In the simulation it was found that the inversion of the absorber can be influenced by interface states at the secondary junction between CdS and HRT layer, when the charge

held at the interface becomes comparable to the charge of the CdS layer. Furthermore, Kephart et al [76] simulated the effect of the electron affinity of the HRT layer in case of a device with a poorly inverted absorber. Results of the simulation highlighted that a lower electron affinity of the HRT layer can be beneficial for the Voc of the device. The band gap widening in MZO films is mainly caused by a conduction band shift that in turns results in a reduced electron affinity. The results reported in this study are in agreement with these works, showing a strong correlation between the electron affinity of the MZO HRT layer and all device performance parameters. It was also found a correlation between electron affinity of the HRT layer and the interface recombination.

5.3 The reduction of optical losses by CdS layer elimination

This section presents a work focused on the use of a MZO buffer layer as a replacement for CdS which is completed eliminated from the solar cells structure. The process of optimisation of the MZO layer used as buffer layer is similar to what was presented before in the firs section of this chapter, and involved the tuning of the MZO band gap to a favourable band alignment with the CdTe absorber. CdS elimination was desired to enhance the transparency of the window stack of layers.

5.3.1 Methodology

Magnesium-doped ZnO thin films were deposited by Radio-Frequency (RF) magnetron sputtering with a 3" diameter MZO target containing 11 % MgO and 89 % ZnO (Wt %). A 4 mm thick glass coated with FTO conductive oxide (NSG TECTM C10 Pilkington glass :$\approx 2.61 \cdot 10^{-4}$ Ω·cm, ≈ 10 $\Omega \setminus \square$) was used as superstrate. The cleaning technique of the glass superstrates has been previously described in chapter 3. The CdTe absorber was deposited at CREST by CSS at a pressure of 1 mTorr of 6% O_2 in Ar, at a CdTe source plate temperature of 630 °C and substrate temperature of 515 °C for 2 minutes. The spacing between substrate and source plate was set to be 2 mm. The $CdCl_2$ activation treatment was carried out by thermal evaporation. A quartz crucible was loaded with

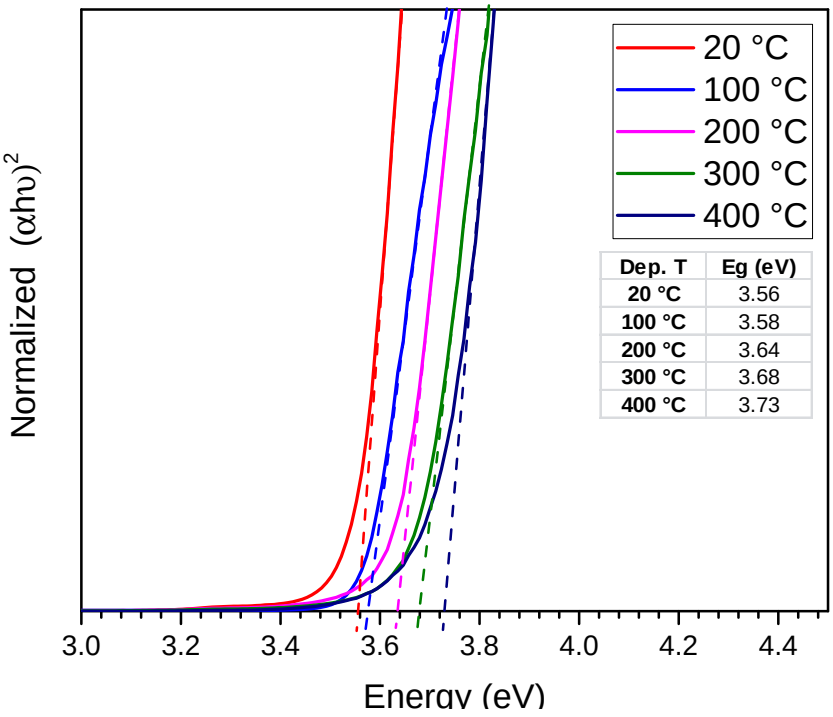

Figure 5.9: The Tauc plot relative to MZO films sputtered with the new target showing the relation between the band gap of the material and the temperature at which the film is deposited.

0.5 g of $CdCl_2$ pellets, which was then evaporated at ≈1 x 10^{-6} Torr for 20 minutes. The samples were subsequently annealed on a hot plate at a dwell temperature of 425 °C for 3 minute with a 5°/min ramping rate. Devices were then washed with DI water to clean the CdTe surface from the $CdCl_2$ residues and then completed with 80 nm gold contacts deposited by thermal evaporation. The results of the two studies presented in this chapter cannot be directly compared as samples were prepared in two different labs.

5.3.2 New target: characterization of MZO films

Due to MZO target depletion, a new target was used for the following study. The requested composition of the new target was identical, however slight changes were found between the two targets. Films deposited with this second target yielded, under identical deposition conditions, a lower band gap (Fig. 5.10). The band gap widening due to the increase in substrate temperature was also lower. The temperature profile of the MZO films band gap is provided in Fig. 5.9.

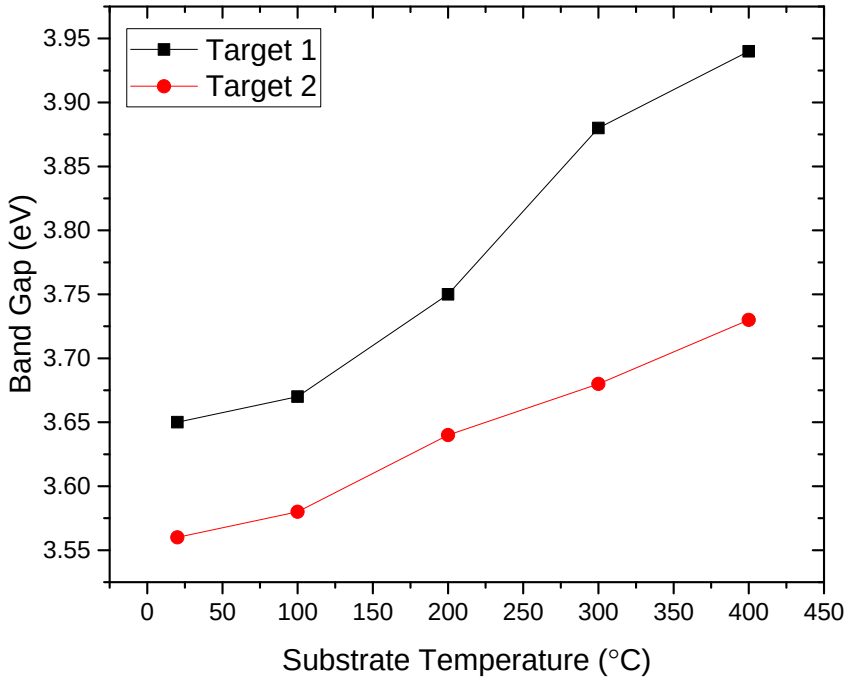

Figure 5.10: The different temperature profiles of MZO films deposited with two different targets. The targets are theoretically of equal composition, however from this graph it is clear that one target contains less Mg than the other.

5.3.3 MZO/CdTe solar cells

The complete elimination of the CdS layer from device structure was achieved. This simplified the solar cell structure to FTO/MZO/CdTe/Au Back contact. Devices were fabricated sublimating the CdTe absorber layers directly on MZO buffer layers deposited at different temperatures (results are presented in Fig. 5.11). As found in the previous section of this chapter where MZO was used in combination with CdS, the deposition temperature of the MZO layers and their band gaps had a significant effect on the device performance. Best efficiencies were achieved when MZO buffers were deposited at 300 °C. The improvement of Voc following the band gap increase is also noticeable in Fig. 5.11 (a). The device Jsc slightly degrades with higher MZO band gap; a possible explanation is that too positive a conduction band offset might hinder electron flow in the conduction band. FF differences can be addressed to slight variation in the fabrication process and especially within the CdTe deposition and $CdCl_2$ treatment which were still not totally consistent between different runs.

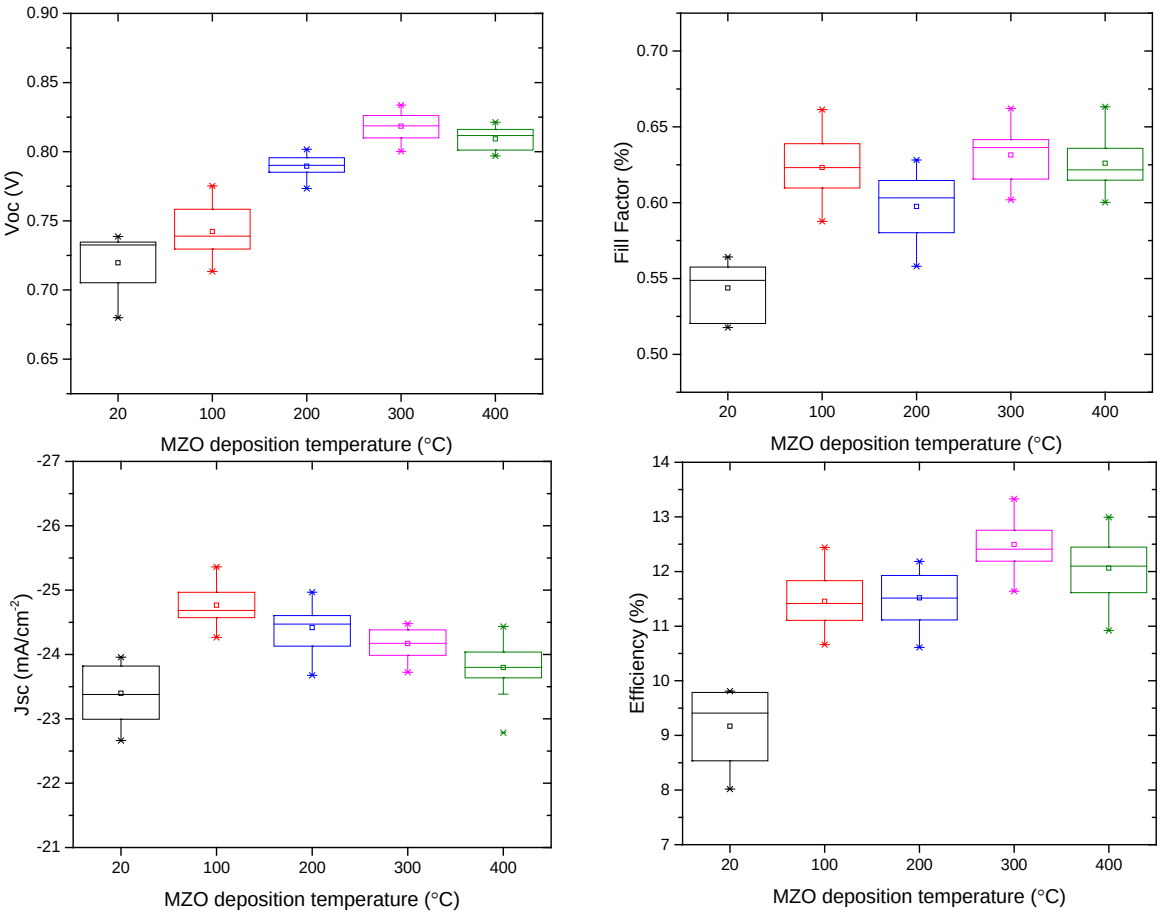

Figure 5.11: Box plots giving a statistical representation of Voc (a), FF (b), Jsc (c) and efficiency (d) of devices containing MZO buffers deposited at increasing substrate temperature.

The current output was the most improved parameter compared to the Jsc values reported for devices containing CdS layers; this is because of the higher transparency of the MZO layers compared with CdS. The transmittance plots of the SLG/FTO/CdS and SLG/FTO/MZO superstrates (Fig. 5.12(a) were used to model the ideal Jsc values available by using each structure type. The methodology for this calculations is explained in detail in chapter 3. Modelled Jsc resulted being 26 mA/cm^2 by using MZO and 20 mA/cm^2 by using a CdS buffer. Fig. 5.12(b) shows a comparison between the AM1.5G spectrum before and after being filtered with the transmission spectrum of the two structures. This is a good way to visualise the photon flux gain due to the MZO layer. In fact by using a MZO buffer instead of CdS, a significant increase in the available spectral irradiance is obtained, especially below 500 nm. The normalised EQE of devices incorpo-

rating equivalent bilayer confirms the improved spectral response when using MZO and validates the modelled data presented previously.

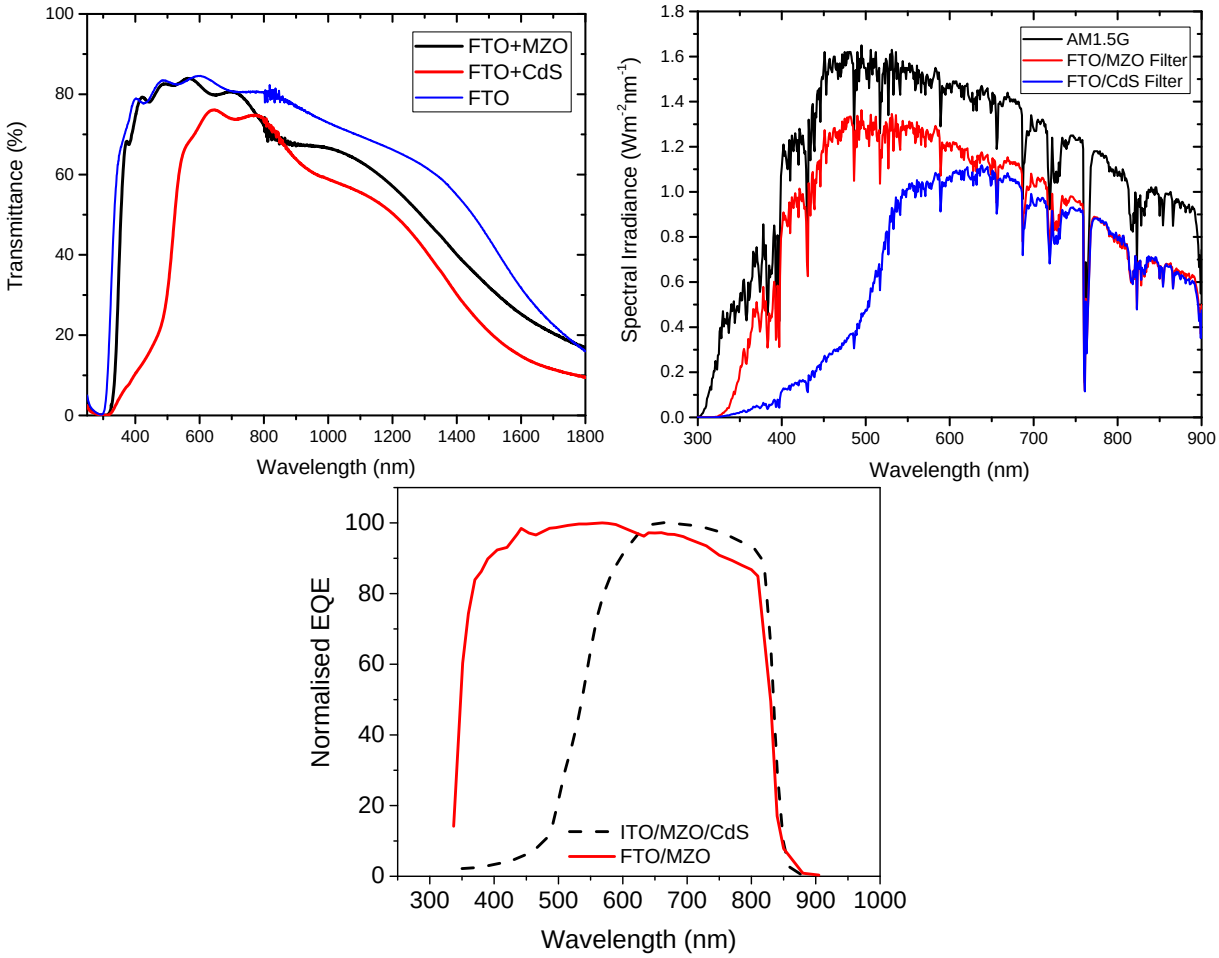

Figure 5.12: Diagram (a) shows the transmittance of the standard FTO layer used in this study, of a FTO/MZO bilayer and of a FTO/CdS bilayer, all deposited on an identical glass superstrates. Diagram (b) shows the AM1.5G spectral irradiance, i.e. the theoretical irradiance available to a solar cell if the window layers were completely transparent and then compares it with the filtered spectral irradiance in the two cases the filter are a FTO/MZO and a FTO/CdS bilayer. Finally diagram (c) shows the EQE characteristic of a FTO/MZO/CdTe device (red line) in comparison with a FTO/MZO/CdS/CdTe device (black dashed line).

5.4 Conclusions

In this study MZO was used both as an HRT layer and as a buffer layer for CdTe thin film solar cells. In both cases it was found strong evidence to support the hypothesis for

which the conduction band alignment of the window layers of a CdTe solar cell is a key parameter to improve solar cell efficiency. The band gap of MZO was increased by an increased film deposition temperature (20 °C - 400 °C), resulting in higher Mg/Zn ratios and then a higher MgO concentration in the film. The band gap growth consisted mostly in the upward shift of the conduction band minimum, resulting also in a diminished electron affinity. The use of MZO as an HRT layer was proofed for the first time in thin film CdTe solar cells. The band gap increase was used to increase device efficiency, with a maximum of 10.6 % obtained at a MZO layer deposition of 300 °C and a band gap of 3.9 eV which was an improvement on devices without using a MZO HRT. All device parameters were significantly affected by the energy band alignment of the window layers. Results of temperature-dependant JV analysis suggested that one of the cause of this improvement is a reduction of the device interface recombination. Complete elimination of the CdS layer in favour of a FTO/MZO/CdTe/Au back contact structure, allowed further efficiency improvement due especially to higher transparency of the MZO buffer compared to CdS, especially below in the electromagnetic spectrum region below 500 nm. In this case also the electron affinity was used to to reach a maximum efficiency of 12.5 % obtained with MZO $E_g = 3.7$ eV.

Chapter 6

The TCO/MZO window bilayer

6.1 Introduction

The studies presented in the previous two chapters examined the optimisation of the HRT/buffer layer of a CdTe solar cell. This chapter focuses on the testing of different TCO materials used in combination with MZO buffers. It was also investigated the effect of glass substrates with different transparencies. The main aim of the study was to find better performing TCO/MZO combinations than the FTO/MZO bilayer used so far. A description of optimal characteristics of a TCO material is given in chapter 2. The first part of this chapter presents a comparison of optical and electrical properties of FTO, ITO and AZO deposited on commercially available SLG. All these materials have already been tested for thin film CdS/CdTe solar cells [37, 27, 24, 107, 108, 103], however only FTO has been investigated as a partner for MZO in a TCO/MZO/CdTe/back contact structured device [76]. The second part of the study aims to maximise the transparency of the glass superstrate and TCO by improving the NIR transmission. In this study AZO and titanium-doped indium oxide(ITiO) TCOs were deposited on boro-aluminosilicate glass superstrates. Both AZO and ITiO TCOs can be fabricated with carrier concentrations in the 10^{20} cm^{-3} range and with high mobility (above 40 m^2/Vs). These characteristics should guarantee resistivity in the 10^{-4} Ωcm range with low free carrier absorption below 900 nm, which is the range where the CdTe absorber layer is photo-active. Boro-aluminosilicate glass was used because of its low iron content, since a high iron concentration in SLG causes the absorption of a portion of the solar spectrum [109]. Finally the

last part of this study analyses the performance and EQE of thin film CdTe solar cells incorporating the superstrate/TCO combinations.

6.2 Methodology

ITO, AZO, ITiO and MZO thin films were deposited by Radio-Frequency (RF) magnetron sputtering. 4 mm thick Soda lime glass (SLG) and 1 mm thick boro-aluminosilicate glass (EagleXG, Corning) were used as superstrates in the first and second part of the study respectively. The glass cleaning technique is described in chapter 3. Thin films were deposited using an AJA International Orion 8 HV magnetron sputtering system (AJA international, USA) equipped with an AJA 600 series RF power supply. All sputtering targets were 3" diameter. The ITO target contained 10 % SnO_2 and 90 % In_2O_3 Wt %; the AZO target contained 0.5 % Al_2O_3 and 99.5 % ZnO Wt %; the ITiO target contained 2 % TiO_2 and 98 % In_2O_3 Wt %; finally the 3" diameter MZO target contained 11 % MgO and 89 % ZnO Wt %. The glass superstrates were rotated at 10 rpm during deposition to enhance the uniformity of the films. The sputtering process was carried out at a constant power density of 3.5 W.cm^{-2} and at a pressure of 1 mTorr using Ar as the working gas for the TCO materials. Sputtering of MZO films was carried out in a 1 % O_2 in Ar atmosphere at a pressure of 5 mTorr. The temperature of the superstrate was kept constant at 450 °C for the deposition of ITO and ITiO and 300 °C for AZO and for MZO films. NSG TEC^{TM} C10 glass (Pilkington) was used for FTO analysis. The optical properties were investigated using a Varian Cary 5000 UV-VIS-NIR spectrophotometer. The composition of the glass superstrates was measured using an X-ray photoelectron spectrometer (XPS) (Thermo Scientific K-alpha). The CdTe absorber was deposited by CSS at a pressure of 1 Torr of 6% O_2 in Ar, at a CdTe source plate temperature of 630 °C and substrate temperature of 515 °C for 2 minutes. The spacing between substrate and source plate was set to 2 mm. The $CdCl_2$ activation treatment was carried out by thermal evaporation. A quartz crucible was loaded with 0.5 g of $CdCl_2$ pellets, which was then evaporated at ≈1 x 10^{-6} Torr for 20 minutes. The samples were subsequently annealed on a hot plate at a dwell temperature of 425° C for 3 minutes with ramping rate of 5°/min. Devices were washed with DI water to clean the CdTe surface from the remaining $CdCl_2$

and completed with 80 nm gold contacts deposited using thermal evaporation. Devices were characterised by measuring their J-V characteristics as described in chapter 3, and by EQE. The EQE measurements were carried out with a PVE300 EQE system (Bentham Instruments Limited, UK) with a 5 nm resolution.

6.3 Optical-electrical Properties of AZO, ITO and FTO on 4mm thick SLG

The electrical properties of the AZO, ITO and FTO TCOs deposited on 4 mm thick SLG were analysed using 4-point probe and Hall effect measurement. ITO proved to be the most conductive material due to both a higher carrier concentration and mobility (Table 6.1) while AZO films exhibited the worst electrical performance among the three materials. Consequently, relatively thin ITO films (250 nm) can provide a sufficiently low sheet resistance ($< 10\ \Omega/\square$) while FTO and AZO films require thicker films, with FTO being a compromise between ITO and AZO. The high ITO carrier concentration, can however limit the transmittance of the solar spectrum in the NIR wavelength due to high free carrier absorption and plasma resonance reflectivity. The optical properties of ITO, AZO and FTO films are shown in Fig. 6.1 (a) and (b). ITO absorption exhibits a grows at around 640 nm reaching its maximum at ≈1230 nm. Considering the CdTe band gap of 1.45 eV (≈ 855 wavelength) the ITO transparency decease after 630 nm could potentially cause photocurrent losses. FTO also shows free carrier absorption but the maximum is shifted between 1600 nm and 1700 nm, hence the impact on the number of photons available to be absorbed by the CdTe layer is reduced. AZO was not expected to show any significant free carrier absorption within the wavelength range analysed due to its lower carrier concentration, however Fig. 6.1 (b) shows an increasing absorption from 700 nm upwards, similar to that of FTO.

Table 6.1: The thickness of ITO, AZO and FTO films and their sheet resistance (R_{sheet}), carrier concentration (N), mobility (μ) and resistivity (ρ).

Material	Thickness [nm]	R_{sheet} [Ω/□]	Carrier concentration (N) [cm^{-3}]	Mobility (μ) [$cm^2/V{\cdot}s$]	Resistivity (ρ) Ω·cm
ITO	250	4	-1.80 x 10^{21}	34	1 x 10^{-4}
AZO	900	10	-3.66 x 10^{20}	19	9 x 10^{-4}
FTO	450	10	-5.60 x 10^{20}	25	4.40 x 10^{-4}

Overall FTO provides the best optical properties for CdTe solar cells due to the highest overall transmittance below 830 nm and the highest band gap (≈4 eV against the 3.9 eV of ITO and 3.4 eV of AZO, Fig. 6.1 (c)) allowing a larger amount of the UV spectrum through the film. A MATLAB script was used to model the ideal Jsc that a CdTe solar cell could yield depending on the optical transmittance of the TCOs. This method is explained more in detail in chapter 3 and it was used as a first test to have an approximate quantification of the TCO performance. However, it is important to specify that this method does not reliably simulate the optical behaviour of the final solar cell, because the addition of MZO and CdTe layer potentially vary the optical performance of the layer stack. Fig. 6.1 (d) shows the available spectral irradiance of the AM1.5G spectrum filtered with the TCO transmittance characteristics: significant optical losses occur below 450 nm when using AZO, due to its lower band gap, while towards higher wavelengths the transparency of the AZO films is comparable with the one of ITO and FTO, despite it is a thicker layer. The ideal Jsc available from the AM1.5G in the wavelength range between 250 nm and 855 nm assuming zero optical losses was calculated to be 30.8 mA/cm^2 . When the spectrum was filtered with an ITO, AZO and FTO filter this value decreased respectively to 23.9 mA/cm^2, 23.2 mA/cm^2 and 25.0 mA/cm^2, confirming that FTO has the best optical properties among the 3 TCOs analysed in this section.

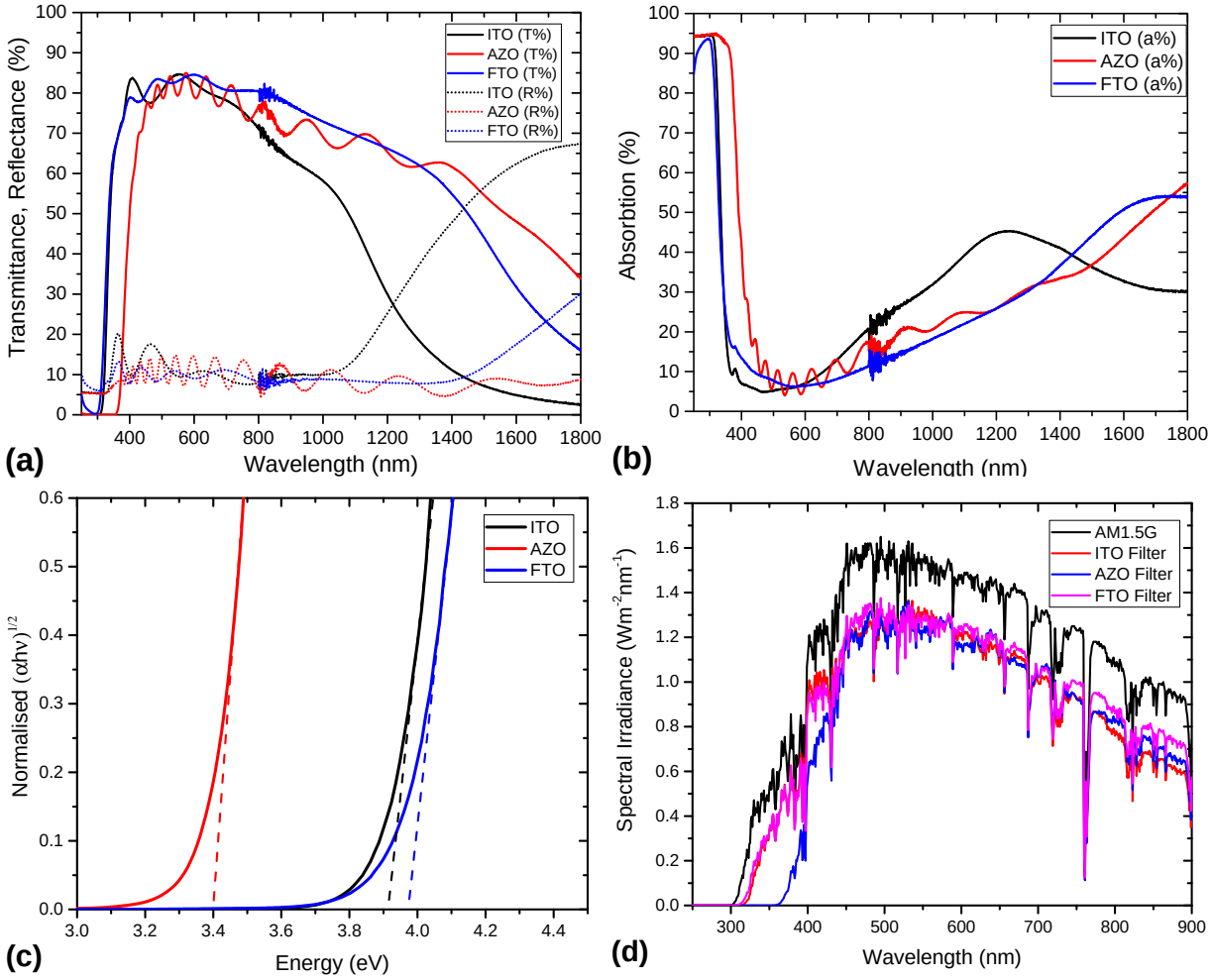

Figure 6.1: (a) shows the transmittance and the reflectance of ITO, AZO and FTO films. The absorption is shown in diagram (b) while diagram (c) shows the Tauc plot with the estimation of each material band gap. The diagram (d) shows the AM1.5G spectrum before and after filtering it with the transmittance characteristic of each material and serves to compare visually the impact of material transparency on the spectrum.

6.4 Analysis of optical properties of glass superstrates

Due to the lower carrier concentration of AZO compared with ITO and FTO, it was expected that it would provide the best optical transparency in the spectrum NIR region. As shown in the previous section this was not the case and further investigation was carried out to test whether the glass substrate has a role in the decreased AZO transparency. A possible cause of degraded optical properties of the glass is a high-iron content. It has been

shown that Fe_2O_3, depending on its concentration in the glass, can increase the glass NIR photon absorption [109]. Spectrophotometry has detected a growing absorption above 600 nm of the 4 mm thick SLG (the same glass used to produce TEC10 superstrates) used as a superstrate (Fig. 6.2). In addition XPS analysis confirmed the presence of iron (1.9% at. %). This indicates that the unexpected absorption above 600 nm measured for the AZO samples could be related to the glass substrate rather than material itself.

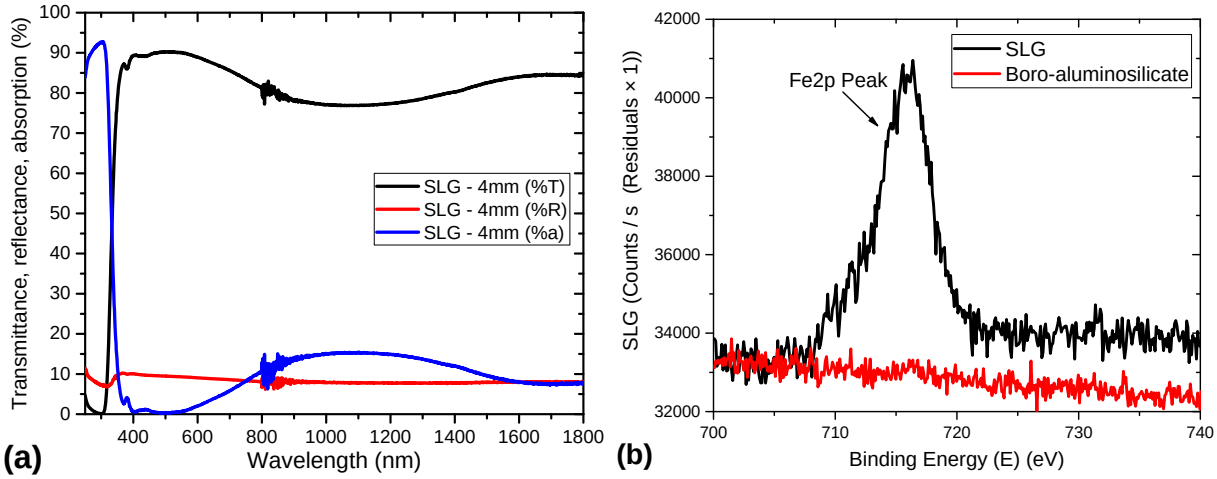

Figure 6.2: Diagram (a) shows the transmission, reflection and absorption spectra of the 4 mm thick SLG used as a superstrate for ITO, AZO and FTO TCOs. Diagram (b) presents the high resolution XPS spectrum focusing on the Fe2p peak, both for boro-aluminosilicate glass and SLG.

A 1 mm thick boro-aluminosilicate (BSG) glass was tested as a superstate material. The iron content of this glass is below detection level for XPS measurement, and lower than that of SLG. The optical properties are summarised in Fig. 6.2. The glass transmits an average of 92 % above 300 nm and absorbs almost 0 % of the the radiation up to 1800 nm. Modelling indicated that the ideal Jsc for the 1 mm thick boro-aluminosilicate superstrate is 28.3 mA/cm^2, which compared to that of SLG (Jsc: 26.6 mA/cm^2) allows for a potential gain of 1.7 mA/cm^2, mostly due to a higher transmittance in the NIR-IR region (Fig 6.3 (d)). To have a more precise comparison between the glass superstrates however a boro-aluminosilicate glass with comparable thickness of SLG should be used. Since this type of glass was not available, for this purpose a stack of 4 x 1 mm boro-aluminosilicate glass slides was analysed. This setup does not yield a direct measurement of the transmittance of a single 4 mm thick boro-aluminosilicate glass since the addition

of each 1 mm thick boro-aluminosilicate glass adds a reflection plane due to a non-perfect contact between the glass slides and the air trapped between them. This is shown in Fig. 6.3 (b), where it can be seen that the addition of each glass slide caused a drop in the total transmittance and a corresponding increase in the reflectance. To simulate the optical behaviour of a single 4 mm thick boro-aluminosilicate glass two steps were required; firstly the reflectance spectrum of the boro-aluminosilicate glass slides stack was added to its transmittance spectrum. This served to eliminate the effect of the multiple internal reflections happening at the interface between each glass slide; secondly the reflectance of a single glass slide was subtracted from the resulting spectrum. This assumes that the reflectance is not affected by the thickness of the glass. Results are presented in Fig. 6.3 (c), indicating that a 4 mm boro-aluminosilicate glass has a slightly increased absorption in the NIR region compared to a 1 mm glass slide, with an absorption peak at around 1400 nm. Within the wavelength range 250 nm - 855 nm however the transparency of the 4 mm and 1 mm superstrates are almost identical (modelled Jsc: 28.3 mA/cm^2). The study presented in this section emphasises the importance of having a low absorption (and low iron) glass to maximise the current output of CdTe solar cells. The same applies for other technologies, and is arguably even more important for those using a lower band gap absorber layer. For example this applies for CIS and CIGS technologies which, although usually fabricated with a substrate structure, when scaled up to modules are typically squeezed between two glass sheets for sealing purposes. Another solution would be to use thinner glass, however this could be at increased risk of breakage.

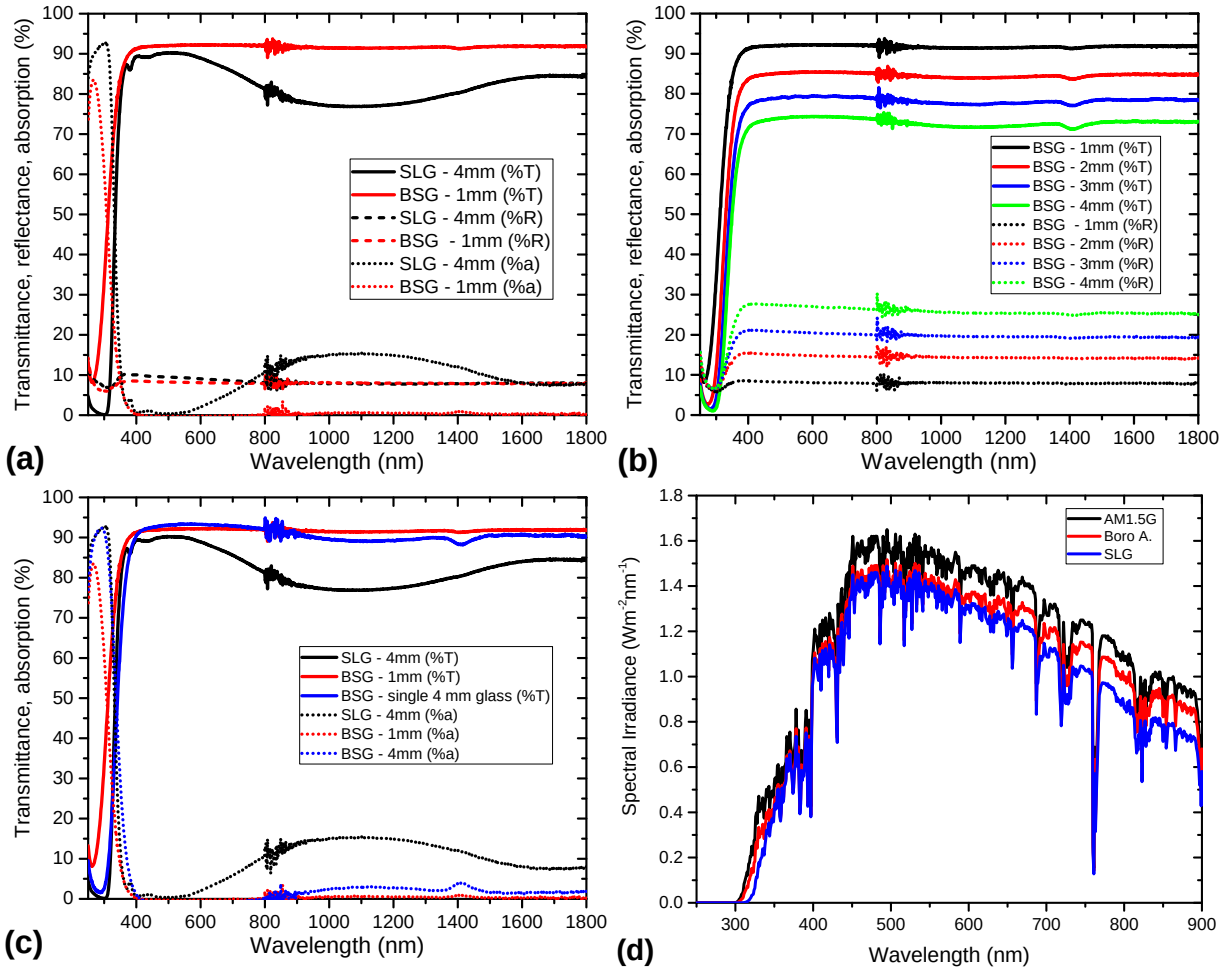

Figure 6.3: Diagram (a) compares the optical properties of 4 mm SLG and 1 mm boro-aluminosilicate glass. (b) shows the transmittance and reflectance of a stack of boro-aluminosilicate glass slides: 1 mm is one single glass slide while 4 mm corresponds to four equivalent glass slides. The reflectance increases every time a slide is added. (c) shows an estimation of what the optical properties of a single 4mm boro-aluminosilicate glass slide would be in comparison with the 4 mm SLG and the 1 mm boro-aluminosilicate glass. Finally (d) shows the AM1.5G spectrum before and after being filtered with the transmittance characteristic of each material.

6.5 AZO and ITiO on boro-aluminosilicate glass superstrates

This section presents an investigation of AZO and ITiO TCOs deposited on 1 mm thick boro-aluminosilicate glass with low absorption in the NIR. Both TCOs can be fabricated

with low carrier concentrations and high mobility, hence with low free carrier absorption within the spectral range over which CdTe is photo-active [110, 111, 112, 113]. The electrical properties of the two semiconductors were analysed using both 4-point probe and Hall effect methods (Table 6.2). The two TCOs have similar carrier concentrations; ITiO shows a higher mobility and thus a lower resistivity while the AZO film, when compared to its equivalent on SLG, has a higher mobility and consequently a lower resistivity. As a result a thinner AZO film was sufficient to obtain the same sheet resistance as AZO on SLG.

Table 6.2: The table summarises the thickness of ITiO and AZO films on boro-aluminosilicate glass and their sheet resistance (R_{sheet}), carrier concentration (N), mobility (μ) and resistivity (ρ).

Material	Thickness [nm]	R_{sheet} [Ω/□]	Carrier concentration (N) [cm^{-3}]	Mobility (μ) [cm^2/V·s]	Resistivity (ρ) Ω·cm
ITiO	230	8	-3.90 x 10^{20}	89	1.8 x 10^{-4}
AZO	700	10	-3.6 x 10^{20}	26	6.75 x 10^{-4}

The optical properties of the AZO films vary depending on the glass superstrate they are deposited on. The transparency of AZO deposited on boro-aluminosilicate glass is higher than that of AZO on SLG over the entire visible and NIR range (Fig. 6.4 (a)). The wavelength range where the improvement is greatest coincides with the SLG high absorption wavelength range. The potential Jsc gained by depositing AZO on boro-aluminosilicate glass rather than SLG was estimated to be 2.2 mA/cm^2 (Jsc: 25.4 mA/cm^2). This is higher than the modelled gain resulting from the new glass superstrate. As can be seen in Fig. 6.4 (d) the photon gain is primarily in the NIR region of the spectrum.

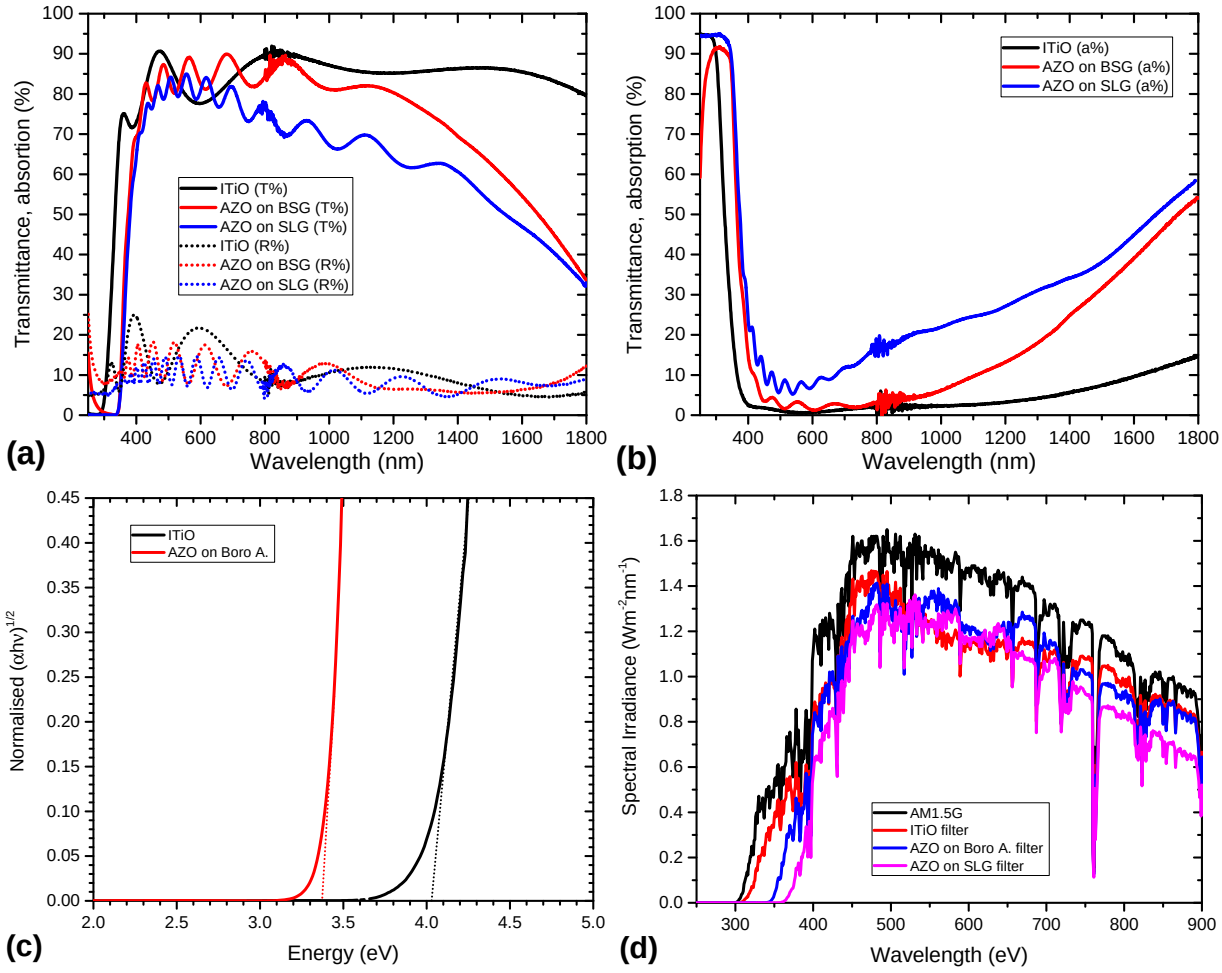

Figure 6.4: Diagram (a) shows the transmittance and the reflectance of ITO, AZO and FTO films. The absorption is shown in (b) while in (c) the Tauc plot showing the calculation of each material band gap is presented. Diagram (d) shows the AM1.5G spectrum before and after filtering by using the transmittance characteristic of each material and serves to compare visually the impact of material transparency on the spectrum.

The optical properties of ITiO on boro-aluminosilicate glass were also tested, highlighting the highest transparency among all TCOs taken analysed so far. ITiO has a 4 eV band gap ensuring high transmission in the UV (Fig. 6.4 (c)). Furthermore little absorption is present in the NIR range (Fig. 6.4 (a) and (b)). It is also very transparent in the visible region, although there is a significant transmission dip around 600 nm due to interference effects that might change once the MZO buffer and CdTe layer are added on top. The potential Jsc gain due to the use of ITiO on boro-aluminosilicate glass superstrates (Jsc = 25.7 mA/cm^2) was estimated to be 0.8 mA/cm^2 compared with FTO on

SLG and 0.3 mA/cm^2 compared with AZO on an identical glass superstrate; the higher photon transmittance is due to the ITiO higher transparency in the NIR wavelength range (Fig 6.4 (d)).

6.6 TCO testing in thin film CdTe solar cells

The TCOs deposited on SLG and boro-aluminosilicate glass analysed in the previous sections were incorporated into thin film CdTe solar cells, the main performance parameters of which are presented in Fig. 6.5. The best mean efficiency was achieved by using AZO TCOs on a boro-aluminosilicate glass superstrate (12.6 %) although relatively high performance was also obtained with the AZO deposited on SLG (12.3 %) . The main difference when using the more transparent superstrate is a significantly higher mean Jsc output (25.1 mA/cm^2 against 23.7 mA/cm^2) which is partially counterbalanced by a lower mean FF (63 % VS 65 %), while the Voc is equivalent (801 mV). The gain in current density is significant but less than that estimated in previous sections, however there are other non-optical loss mechanisms like interface and bulk recombination that were not taken into account. CdTe solar cells incorporating FTO were the second best performing, yielding 12.5 % mean efficiency and the best Voc (818 mV) overall, with a mean Jsc of 24.2 mA/cm^2. CdTe solar cells with ITiO and ITO TCOs yielded the lower efficiencies (10.4 % and 10.5 % respectively), both negatively affected by low FF (ITiO: 56 %, ITO: 55%). Solar cells incorporating ITO are characterised also by a relatively high mean Voc (807 mV), however they showed a low mean current density output (22.9 mA/cm^2). ITiO-based solar cells showed a significantly lower Voc (756 mV) compared to all the other devices while giving a high Jsc (24.6 mA/cm^2).

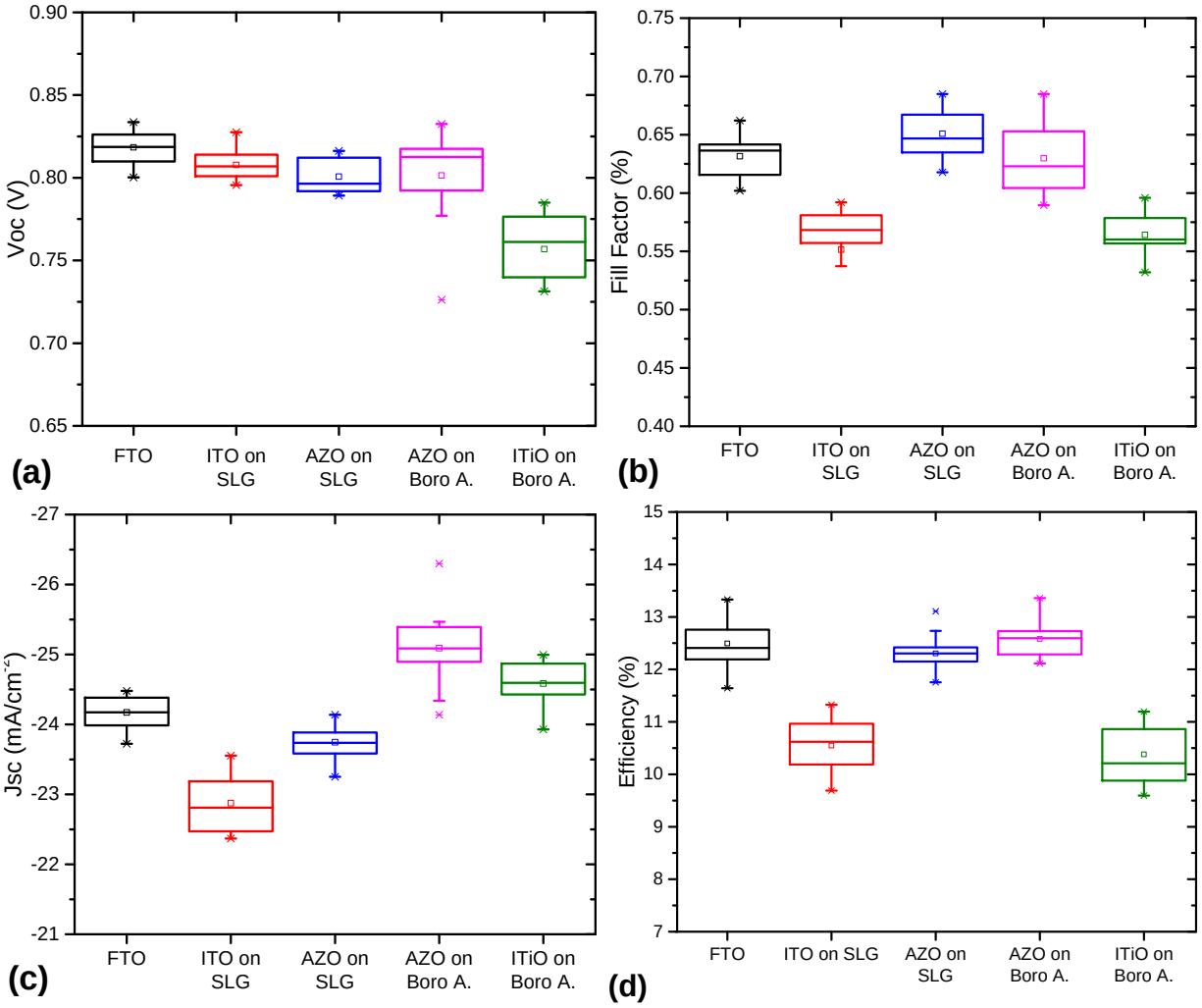

Figure 6.5: The figure shows box plots of the Voc (a), the FF (b), the Jsc (c) and the efficiency (d) of CdTe thin film solar cells incorporating different TCO materials.

6.6.1 EQE measurements

EQE results are presented in Fig. 6.6. It is noticeable that the UV absorption edge of solar cells incorporating the high band gap TCOs (ITO,FTO, ITiO) is shifted to longer wavelengths, presumably by the band gap of the MZO layer.

Table 6.3: Table summarising the AZO, FTO, ITO, ITiO and MZO band gaps.

Material	AZO	FTO	ITO	ITiO	MZO
Eg (eV)	3.4	3.9	3.8	4	3.7

In most cases the transmittance spectrum gives lower values than the EQE spectrum,

meaning that there are more photons reaching the absorber layer than implied by transmission curves. The measurement setup used for spectrophotometry in fact does not accurately simulate a solar cell, since the deposition of the MZO and CdTe layer on top of the TCO is likely to affect the transmittance and the reflectance of the layers stack, due to a difference in refractive index matching when subsequent layers are deposited on top. The film absorption spectrum can also provide useful information about film quality, being a characteristic of the film not dependent on other materials in the structure. For this reason a 100 % - absorption curve has been added to each graph, providing the percentage of photons that would be available if no reflection occurred. 100 % - absorption can be also seen as an ideal limit, and reducing the gap between this limit and the values calculated from EQE measurements would translate into an improved photo-generation and extraction efficiency. This gap can be visualised in Fig. 6.6 as the red area between the 100 % - absorption plot and the EQE plot. Following this approach it is clear that the CdTe solar cells fabricated on AZO/SLG superstrates are the least effective. This difference might be reduced by further optimisation of the fabrication process, although it is also possible that mechanisms related to the ITiO/MZO bilayer, might limit the performance of the solar cell. Each diagram in Fig. 6.6 shows the current density estimated from the area below the EQE curve. These values follow the trend of those measured by J-V characterization but are increased (with a 2% margin of difference). This is lickely due to a non-perfect calibration of the solar simulator used of J-V charaterisation;

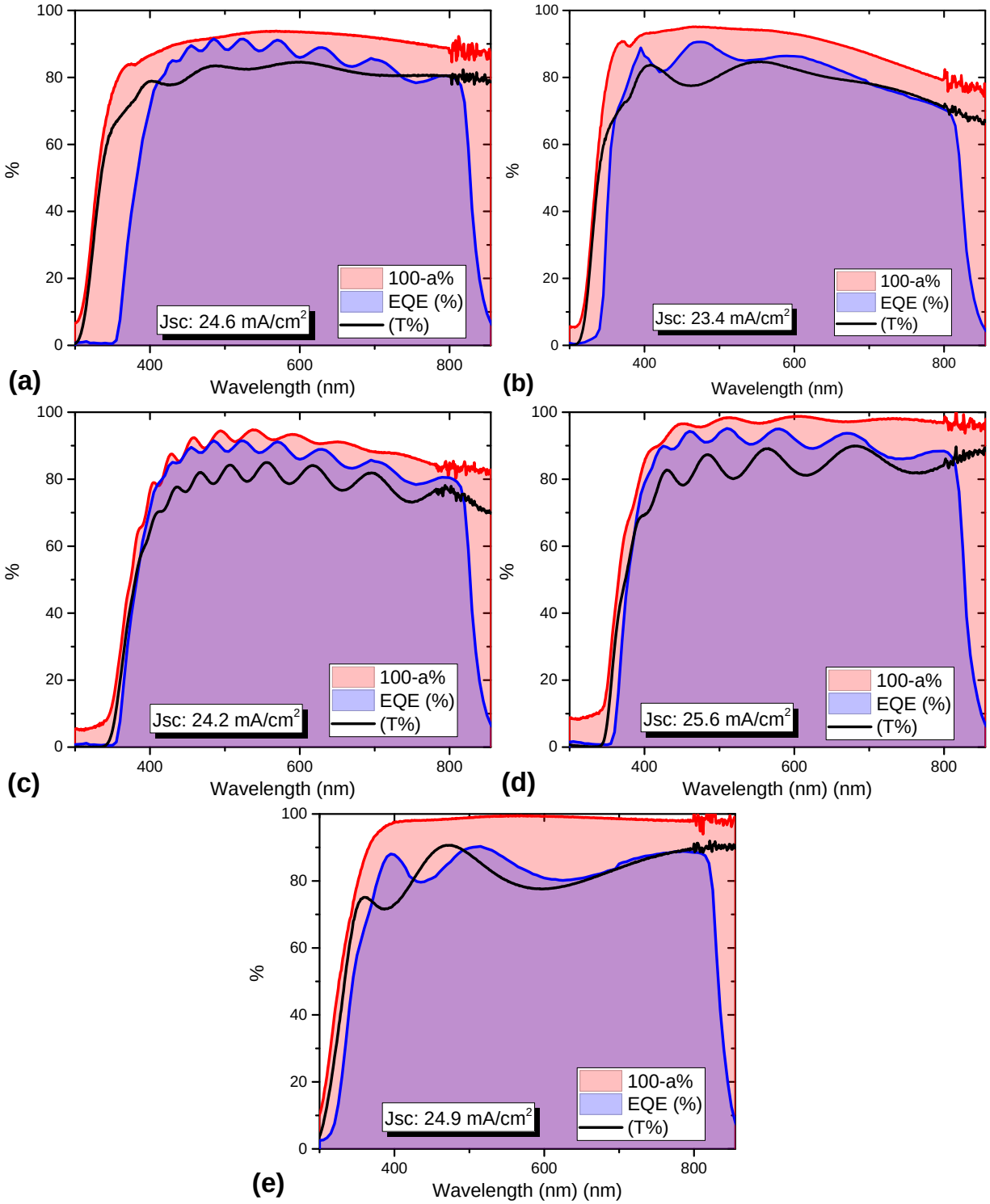

Figure 6.6: The EQE spectra of thin film CdTe solar cells deposited on FTO on SLG (a), ITO on SLG (b), AZO on SLG (c), AZO on boro-aluminosilicate glass (d) and ITiO on boro-aluminosilicate glass (e). For comparison the 100 % - absorption and transmittance spectrum of the incorporated TCO is displayed on each plot. The Jsc values calculatedfrom the EQE are shown for each device.

6.7 Conclusions

This study analysed the performance of different TCO/MZO combinations deposited on SLG and on low-absorbing boro-aluminosilicate glass as window layers for thin film CdTe solar cells. Results have been summarised in Table 6.4. The aim of the study was to find TCO/MZO bilayers which improved upon the performance the performance of thin film CdTe solar cells obtained with SLG/FTO/MZO superstrates.

Table 6.4: The table summarises the Jsc values modelled with Matlab, those measured by J-V characterisation and those calculated from the EQE data for each TCO/superstrate combination studied. The ratio between each current density output and that of FTO is given in parentheses, next to each Jsc value. This value was selected as the reference for comparison. The modelled Jsc values for the glass superstrates were calculated using the respective glass transmission and added to the table.

Superstrate	TCO	Jsc (mA/cm^2)		
		Modelled	J-V	EQE
SLG (Jsc: 26.6 mA/cm^2)	**FTO**	**25.0 (1.00)**	**24.2 (1.00)**	**24.6 (1.00)**
	ITO	23.9 (0.96)	22.9 (0.95)	23.4 (0.95)
	AZO	23.2 (0.93)	23.7 (0.98)	24.2 (0.98)
Boro-aluminosilicate (Jsc: 28.3 mA/cm^2)	AZO	25.4 (1.02)	25.1 (1.04)	25.6 (1.04)
	ITiO	25.7 (1.03)	24.6 (1.02)	24.9 (1.01)

The TCO films were deposited to achieve $R_{sheet} < 10\ \Omega/\square$, and the optical properties were used to modelled Jsc values based on their transmission characteristics. Model values imply that ITO and AZO deposited on SLG do not provide any optical benefit as compared to FTO, since ITO has higher absorption in the NIR spectrum region and AZO has a NIR absorption comparable to that of FTO with the additional disadvantage of a lower band gap. Optical losses due to the glass, which are related to the high iron content of the SLG superstrates, were significantly decreased by using more transparent boro-aluminosilicate superstrates in combination with AZO and ITiO TCOs. In particular ITiO, due to its high mobility and lower carrier concentration and resistivity, allowed for the deposition of very thin and transparent films over the full VIS-NIR spectrum

range up to 855 nm. Films were incorporated into thin film CdTe solar cells for practical comparison. Results indicated that ITO/MZO and ITiO/MZO seem not to be ideal window layer combinations for TCO/MZO/CdTe based solar cells, resulting in a reduced FF. ITiO resulted also in a reduced cell voltage and ITO in a reduced current density output. The performance of CdTe devices including ITiO and ITO might be improved by further variations/optimisations of the fabrication process. The AZO/MZO bilayer however yielded generally very good performance. SLG/AZO superstrates achieved good efficiencies thanks to a particularly high FF and relatively high Jsc despite being the least transparent glass/TCO combination among those analysed. AZO/MZO window layers on boro-aluminosilicate glass yielded the best efficiencies and Jsc overall as well as high FF. ITiO TCOs provided the lowest efficiencies as a result of reduced FF and Voc. Performance of CdTe solar cells incorporating this TCO might be improved by further optimisation, but the mechanism hindering device efficiency is at present unknown. EQE spectra of fabricated devices generally show that ITO, FTO, and AZO on SLG show optical losses due to an absorption increase at around 600 nm. This is decreased by using boro-aluminosilicate superstrates, in particular in combination with AZO and ITiO.

Chapter 7

Future Work

Device efficiencies presented in this work are lower than the record efficiency achieved by First Solar. The CdTe solar cell record efficiency is 21 %, with Jsc: 30.3 mA/cm^2 , Voc: 876 mV and FF: 79.4 %. Efficiencies presented in this thesis are mean values, not best performance. A best efficiency of 13.4 % with Jsc: 24 mA/cm$_2$, Voc: 816 mV and FF: 68 % was obtained by an AZO/MZO/CdTe/Au solar cell. This efficiency is the result of the buffer layer optimisation and the consequent reduction of optical losses occurring in the window layer. It is known that one of the most important aspects of this technology is the back contact formation. As explained in chapter 2, it is challenging to form a ohmic or quasi-ohmic back contact with the CdTe layer. In this work the CdTe solar cells were fabricated with an Au back contact, which is not optimal. Device efficiency is being limited by the non-ideal back contact formation, as highlighted by the J-V characterisation which presents the roll-over effect typical of a contact with a energy barrier (Fig. 7.1). The back contact formation should be the next focus of this research. Improvement of this fabrication step can allow a significant efficiency increase. A preliminary test was carried out by evaporating 5 nm of Cu on the CdTe surface prior to the Au deposition. A consequent annealing of the sample at 200 degC for 20 minutes was also performed. The device J-V is presented in Fig. 7.1 in comparison with an equal sample with no Cu and with the First Solar record efficiency J-V. The FF of the the Cu-free sample is significantly lower than that of First Solar and the one of the record sample made at CREST, due to a problem in the fabrication process that it is not yet being solved.

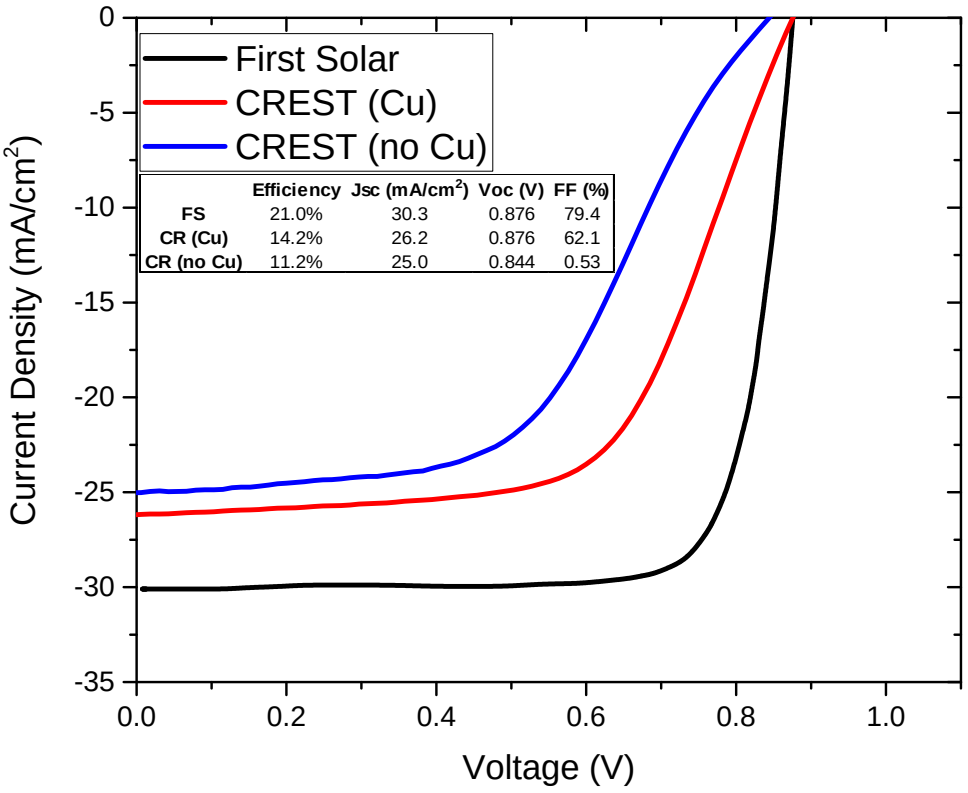

Figure 7.1: Presented in figure, the J-V plot of the record efficiency solar cell by First solar, the J-V of the record efficiency solar cell with by CREST, achieved with a solar cell with a Cu-based back contact and finally the J-V of an Cu-free device.

It is noticeable that all performance parameters improve with Cu. This confirms that a better back contact is crucial for device performance. The solar cell with Cu has lower efficiency than the record device from First Solar, due to a lower Jsc and FF. The Jsc is probably still negatively affected by the poor solar cell back contact. Also, First Solar used Se to decrease the absorber band gap and anti-reflecting coatings were utilised. Both these strategies lead to a further increase the Jsc. The FF is significantly lower than that of First Solar. This is attributable to the high device series resistance, highlighted by the slope of the J-V characteristics above 0.6 V [61]. Summarising, the priority for future work seem the back contact improvement, with the main aim to maximise FF. Different strategies can bring to a better back contact. To date, the most effective methods seem either the deposition of a Te layer on top of the CdTe layer [114, 115] or the deposition of an electron reflector [53, 52]. Both these techniques aim to form a quasi-ohmic contact with the CdTe. Cu is required in combination with either of these two materials, although

efforts are being made to make use of as little as possible Cu for a more stable device. The improvement of the device Jsc is also an important aspect. The window materials of the solar cell are highly transparent and it seems difficult to achieve further significant optical gains in this region of the solar cell. The grading of the CdTe band gap by adding a dopant, like Selenium, is necessary to achieve Jscs comparable with the one of first solar. Alternative ways to include Se (or another dopant) in the CdTe layer to form a ternary compound with a lower band gap than CdTe should be inspected.

Chapter 8

Conclusion

CdTe thin film solar cells are a promising PV technology capable of providing low-cost and high efficiency modules. The improvement of the power conversion efficiency is one of the main reasons for further reductions of the LCOE provided by any PV technology (CdTe included). The PV module performance improvement is a result of a growing understanding of the technology and experiments which researchers carry out on smaller scale solar cells made in laboratories. The work presented in this thesis focused on the optimization of window layers of a CdTe solar cell, which is one of the most controversial (and interesting) areas of research of this technology. Increasing the transparency of the stack of window materials which precede the CdTe absorber is a necessary condition to maximise the efficiency of these devices. However some materials work better than others independently to their optical properties, because of the way materials interface. The standard superstrate structure used to achieve highest performance includes a TCO layer as a front conductive terminal, a buffer layer to create the primary p-n junction with CdTe and finally an intermediate layer (often referred to as HRT layer), sandwiched between the TCO and the buffer which provides an efficiency improvement by allowing a thinner CdS and higher Jsc, limiting Voc and FF degradation. The mechanisms at the base of the HRT utilization are not completely clear; the main theory referred to in literature states that HRT layers serve to avoid shunt currents flowing between CdTe and TCO through weak diodes, in areas of the solar cell where the CdS is thinner or interrupted.

The first chapter of the thesis presents an investigation on ZnO as a HRT material for CdTe solar cells. A number ZnO films have been sputtered with a range of different

optical, structural and electrical properties. The film characteristic variation was a result of the different deposition conditions used to deposit the films. The effect of ZnO film resistivity on device performance was one of the main focus of this study since there are multiple studies suggesting that a HRT layer should be resistive enough to oppose shunting currents. Interestingly in this study no clear relation could be found between film resistivity and device performance. It was found that using a sputtering pressure higher than 5 mTorr leads to more transparent ZnO films and higher Jsc in CdTe thin film solar cells. It was also noticed that by increasing the ZnO film deposition temperature the FF of CdTe devices could be improved. The FF improvement followed an improvement of the crystal structure and might be related to it. The addition of oxygen during ZnO sputtering was also beneficial for the FF, Jsc and efficiency of CdTe solar cells. ZnO films have been thoroughly characterised before being incorporated in actual devices with the aim to highlight relationships between efficiency with any of the bulk properties (structural and electrical), however no clear evidence was extracted. The focus then shifted to interface properties. Firstly SCAPS simulations were run highlighting that interface defects at the HRT/buffer interface can affect the Voc and FF of CdTe devices.

In chapter 2 the study dealt with the HRT/buffer band alignment, which is another interface property. By adding Mg to ZnO and by raising the deposition temperature of MZO films the conduction band minimum was increasingly shifted upwards in energy. This mechanism allowed tuning the conduction band alignment of MZO HRTs with CdS to optimum. CdTe solar cell efficiency was greatly affected by the conduction band position of MZO film relatively to CdS and 0.3 eV was found to be an optimum conduction band offset. It was also found evidence that a positive conduction band offset results in a lower interface recombination. Results of work carried out on ZnO and MZO HRTs strongly emphasise the importance of interface properties. Further confirmation was found when MZO was successfully used as a replacement CdS buffer layer. Again the conduction band offset was a key parameter to optimise device efficiency. The replacement of CdS with a larger band gap semiconductor (MZO) significantly increased the CdTe solar cells Jsc and simplified the window structure for CdTe solar cell to two layers (TCO and MZO).

To complete the window layers optimisation, different TCO/MZO combinations were analysed. FTO was used as a reference TCO since it was the first one being used in

combination with MZO. From an optical point of view, it was found that it is important to deposit the TCO layer on a low iron content glass because too high Fe_2O_3 concentrations cause NIR photon absorption. AZO performed well in combination with MZO and the best efficiencies overall (12.6%, compared with 12.5% achieved with FTO) were achieved when deposited on low-iron content glass, thanks especially to a higher transparency in the NIR compared with FTO and higher Jsc. On the other hand Indium-based TCOs (ITO and ITiO) did not perform as well as expected. In particular ITiO, which is the most transparent TCO overall over the full UV-VIS-NIR spectrum range, yielded lower efficiencies resulting from low Vocs and FFs.

More in general, the results presented in this thesis indicate that interface formation between the different materials composing thin film CdTe solar cells is an important aspect to understand the device behaviour. The interface between the CdTe absorber and the back contact is the only one in CdTe devices which has been investigated with a certain depth in the last decades. The band alignment between the CdTe absorber and adjacent layers, however, has not been given as much attention yet. One of the probable reasons of this it is that it is difficult to obtain a precise estimation of the band alignment between two semiconductors. Moreover the band alignment can also change depending on the technique used to deposit the film. However, the buffer/CdTe and the HRT/buffer band alignment have been proven to be important factors in the studies presented in this thesis. Similarly, it is likely that knowing and understanding interface chemistry and interface defects type and density would also significantly help understanding the device behaviour and should receive greater attention to further optimise device performance.

Bibliography

[1] WEC, "World Energy Resources: 2013 Survey," 2013.

[2] Marc Perez & Richard Perez, "A Fundamental Look At Supply Side Energy Reserves For The Planet (Update)," *SHC Solar Update*, 2015.

[3] C. Riordan and R. Hulstron, "What is an air mass 1.5 spectrum? (solar cell performance calculations)," in *IEEE Conference on Photovoltaic Specialists*, pp. 1085–1088, IEEE, 1990.

[4] ASTM, "ASTM G173-03 Reference Spectra," 2012.

[5] Fraunhofer Institute for Solar and I. Systems, "Photovoltaics Report," tech. rep., Freiburg, 2017.

[6] "Big Data for Big Solar Article," 2017.

[7] I. Amit Kumar Mittal (First Solar, Inc.), Sanjay Singh (First Solar, "Solar Edge," 2017.

[8] W. Shockley and H. J. Queisser, "Detailed Balance Limit of Efficiency of p-n Junction Solar Cells," *Journal of Applied Physics*, vol. 32, pp. 510–519, mar 1961.

[9] H.-W. S. Roland Scheer, "Design Rules for Heterostructure Solar Cells and Modules," in *Chalcogenide Photovoltaics*, pp. 129–174, Weinheim, Germany: Wiley-VCH Verlag GmbH & Co. KGaA, feb 2011.

[10] J. Nelson, "Electrons and Holes in Semiconductors," in *The Physics of Solar Cells*, pp. 41–78, Published by Imperial College press and distributed by World Scientific Publishing CO., may 2003.

[11] J. Nelson, "Generation and Recombination," in *The Physics of Solar Cells*, pp. 79–117, Published by Imperial College press and distributed by World Scientific Publishing CO., may 2003.

[12] M. O. Reese, C. L. Perkins, J. M. Burst, S. Farrell, T. M. Barnes, S. W. Johnston, D. Kuciauskas, T. A. Gessert, and W. K. Metzger, "Intrinsic surface passivation of CdTe," *Journal of Applied Physics*, vol. 118, p. 155305, oct 2015.

[13] J. Nelson, "Analysis of the p-n Junction," in *The Physics of Solar Cells*, pp. 145–176, Published by Imperial College press and distributed by World Scientific Publishing CO., may 2003.

[14] B. E. McCandless and J. R. Sites, "Cadmium Telluride Solar Cells," in *Handbook of Photovoltaic Science and Engineering*, pp. 617–662, Chichester, UK: John Wiley & Sons, Ltd, jan 2005.

[15] D. Bonnet and H. Rabenhorst, "New results on the development of a thin-film p-cdte-n-cds heterojunction solar cell," in *Photovoltaic Specialists Conference, 9 th, Silver Spring, Md*, pp. 129–132, 1972.

[16] W. Beyer, J. Hüpkes, and H. Stiebig, "Transparent conducting oxide films for thin film silicon photovoltaics," *Thin Solid Films*, vol. 516, pp. 147–154, dec 2007.

[17] Z. Su, W. Li, G. Asim, T. Y. Fan, and L. H. Wong, "Cation substitution of CZTS solar cell with $>$ 10% efficiency," in *2016 IEEE 43rd Photovoltaic Specialists Conference (PVSC)*, pp. 0534–0538, IEEE, jun 2016.

[18] C. Ferekides, R. Mamazza, U. Balasubramanian, and D. Morel, "Transparent conductors and buffer layers for CdTe solar cells," *Thin Solid Films*, vol. 480-481, pp. 224–229, jun 2005.

[19] R. Bernal-Correa, A. Morales-Acevedo, J. Montes-Monsalve, and A. Pulzara-Mora, "Design of the TCO (ZnO:Al) thickness for glass/TCO/CdS/CIGS/Mo solar cells," *Journal of Physics D: Applied Physics*, vol. 49, p. 125601, mar 2016.

[20] J. W. Bowers, H. M. Upadhyaya, S. Calnan, R. Hashimoto, T. Nakada, and A. N. Tiwari, "Development of Nano-TiO 2 dye sensitised solar cells on high mobility transparent conducting oxide thin films," *Progress in Photovoltaics: Research and Applications*, vol. 17, pp. 265–272, jun 2009.

[21] M. Willander, O. Nur, Q. X. Zhao, L. L. Yang, M. Lorenz, B. Q. Cao, J. Zúñiga Pérez, C. Czekalla, G. Zimmermann, M. Grundmann, A. Bakin, A. Behrends, M. Al-Suleiman, A. El-Shaer, A. Che Mofor, B. Postels, A. Waag, N. Boukos, A. Travlos, H. S. Kwack, J. Guinard, and D. Le Si Dang, "Zinc oxide nanorod based photonic devices: recent progress in growth, light emitting diodes and lasers," *Nanotechnology*, vol. 20, p. 332001, aug 2009.

[22] Y. Liu, Y. Li, and H. Zeng, "ZnO-Based Transparent Conductive Thin Films: Doping, Performance, and Processing," *Journal of Nanomaterials*, vol. 2013, no. Cvd, pp. 1–9, 2013.

[23] S. Calnan and A. Tiwari, "High mobility transparent conducting oxides for thin film solar cells," *Thin Solid Films*, vol. 518, pp. 1839–1849, jan 2010.

[24] J. Perrenoud, L. Kranz, S. Buecheler, F. Pianezzi, and A. Tiwari, "The use of aluminium doped ZnO as transparent conductive oxide for CdS/CdTe solar cells," *Thin Solid Films*, vol. 519, pp. 7444–7448, aug 2011.

[25] U. Rau and M. Schmidt, "Electronic properties of ZnO/CdS/Cu(In,Ga)Se2 solar cells — aspects of heterojunction formation," *Thin Solid Films*, vol. 387, pp. 141–146, may 2001.

[26] J. M. Kephart, R. M. Geisthardt, Z. Ma, J. McCamy, and W. S. Sampath, "Reduction of window layer optical losses in CdS/CdTe solar cells using a float-line manufacturable HRT layer," in *2013 IEEE 39th Photovoltaic Specialists Conference (PVSC)*, pp. 1653–1657, IEEE, jun 2013.

[27] J. Fritsche, S. Gunst, A. Thiβen, R. Gegenwart, A. Klein, and W. Jaegermann, "CdTe Thin Film Solar Cells: The CdS/SnO2 Front Contact," *MRS Proceedings*, vol. 668, p. H5.1, jan 2001.

[28] T. Liu, X. He, J. Zhang, L. Feng, L. Wu, W. Li, G. Zeng, and B. Li, "Effect of ZnO films on CdTe solar cells," *Journal of Semiconductors*, vol. 33, p. 093003, sep 2012.

[29] S. N. Alamri and A. W. Brinkman, "The effect of the transparent conductive oxide on the performance of thin film CdS/CdTe solar cells," *Journal of Physics D: Applied Physics*, vol. 33, pp. L1–L4, jan 2000.

[30] C. Ferekides, D. Marinskiy, V. Viswanathan, B. Tetali, V. Palekis, P. Selvaraj, and D. Morel, "High efficiency CSS CdTe solar cells," *Thin Solid Films*, vol. 361-362, pp. 520–526, feb 2000.

[31] F. S. Hasoon, H. A. Al-Thani, X. Li, A. Kanevce, C. Perkins, and S. Asher, "Investigation of the effect of I-ZnO window layer on the device performance of the Cd-free CIGS based solar cells," in *2008 33rd IEEE Photovolatic Specialists Conference*, pp. 1–5, IEEE, may 2008.

[32] R. Mamazza, S. Yu, D. Morel, and C. Ferekides, "Co-sputtered Cd2SnO4 films as front contacts for CdTe solar cells," in *Conference Record of the Twenty-Ninth IEEE Photovoltaic Specialists Conference, 2002.*, pp. 612–615, IEEE, 2002.

[33] P. Kaminski, F. Lisco, A. Abbas, J. W. Bowers, G. Claudio, and J. Walls, "Oxygenated CdS window layers for thin film CdTe photovoltaics by pulsed DC magnetron sputtering," in *2014 IEEE 40th Photovoltaic Specialist Conference (PVSC)*, pp. 1626–1631, IEEE, jun 2014.

[34] H. Ohyama, T. Aramoto, S. Kumazawa, H. Higuchi, T. Arita, S. Shibutani, T. Nishio, J. Nakajima, M. Tsuji, A. Hanafusa, T. Hibino, K. Omura, and M. Murozono, "16.0% efficient thin-film CdS/CdTe solar cells," in *Conference Record of the Twenty Sixth IEEE Photovoltaic Specialists Conference - 1997*, pp. 343–346, IEEE, 1997.

[35] A. Munshi, A. Abbas, J. Raguse, K. Barth, W. Sampath, and J. Walls, "Effect of varying process parameters on CdTe thin film device performance and its relationship to film microstructure," in *2014 IEEE 40th Photovoltaic Specialist Conference (PVSC)*, pp. 1643–1648, IEEE, jun 2014.

[36] X. Wu, R. Ribelin, R. Dhere, D. Albin, T. Gessert, S. Asher, D. Levi, A. Mason, H. Moutinho, and P. Sheldon, "High-efficiency Cd2SnO4/Zn2SnO4/ZnxCd1-xS/CdS/CdTe polycrystalline thin-film solar cells," in *Conference Record of the Twenty-Eighth IEEE Photovoltaic Specialists Conference - 2000 (Cat. No.00CH37036)*, pp. 470–474, IEEE, 2000.

[37] I. Rimmaudo, A. Salavei, E. Artegiani, D. Menossi, M. Giarola, G. Mariotto, A. Gasparotto, and A. Romeo, "Improved stability of CdTe solar cells by absorber surface etching," *Solar Energy Materials and Solar Cells*, vol. 162, pp. 127–133, apr 2017.

[38] J. D. Major, M. Al Turkestani, L. Bowen, M. Brossard, C. Li, P. Lagoudakis, S. J. Pennycook, L. J. Phillips, R. E. Treharne, and K. Durose, "In-depth analysis of chloride treatments for thin-film CdTe solar cells," *Nature Communications*, vol. 7, p. 13231, oct 2016.

[39] I. Visoly-Fisher, S. R. Cohen, and D. Cahen, "Direct evidence for grain-boundary depletion in polycrystalline CdTe from nanoscale-resolved measurements," *Applied Physics Letters*, vol. 82, pp. 556–558, jan 2003.

[40] L. Zhang, J. L. F. Da Silva, J. Li, Y. Yan, T. A. Gessert, and S.-H. Wei, "Effect of Copassivation of Cl and Cu on CdTe Grain Boundaries," *Physical Review Letters*, vol. 101, p. 155501, oct 2008.

[41] C. Li, Y. Wu, J. Poplawsky, T. J. Pennycook, N. Paudel, W. Yin, S. J. Haigh, M. P. Oxley, A. R. Lupini, M. Al-Jassim, S. J. Pennycook, and Y. Yan, "Grain-Boundary-Enhanced Carrier Collection in CdTe Solar Cells," *Physical Review Letters*, vol. 112, p. 156103, apr 2014.

[42] U. Jahn, T. Okamoto, A. Yamada, and M. Konagai, "Doping and intermixing in CdS/CdTe solar cells fabricated under different conditions," *Journal of Applied Physics*, vol. 90, pp. 2553–2558, sep 2001.

[43] S. Demtsu and J. Sites, "Effect of back-contact barrier on thin-film CdTe solar cells," *Thin Solid Films*, vol. 510, pp. 320–324, jul 2006.

[44] A. Niemegeers and M. Burgelman, "Effects of the Au/CdTe back contact on IV and CV characteristics of Au/CdTe/CdS/TCO solar cells," *Journal of Applied Physics*, vol. 81, pp. 2881–2886, mar 1997.

[45] J. N. Duenow, R. G. Dhere, J. V. Li, M. R. Young, and T. a. Gessert, "Effects of back-contacting method and temperature on CdTe/CdS solar cells," in *2010 35th IEEE Photovoltaic Specialists Conference*, pp. 001001–001005, IEEE, jun 2010.

[46] C. Corwine, "Copper inclusion and migration from the back contact in CdTe solar cells," *Solar Energy Materials and Solar Cells*, vol. 82, pp. 481–489, mar 2004.

[47] M. Hädrich, C. Heisler, U. Reislöhner, C. Kraft, and H. Metzner, "Back contact formation in thin cadmium telluride solar cells," *Thin Solid Films*, vol. 519, pp. 7156–7159, aug 2011.

[48] C. Ferekides, V. Viswanathan, and D. Morel, "RF sputtered back contacts for CdTe/CdS thin film solar cells," in *Conference Record of the Twenty Sixth IEEE Photovoltaic Specialists Conference - 1997*, pp. 423–426, IEEE, 1997.

[49] L. Kranz, C. Gretener, J. Perrenoud, R. Schmitt, F. Pianezzi, F. La Mattina, P. Blösch, E. Cheah, A. Chirilă, C. M. Fella, H. Hagendorfer, T. Jäger, S. Nishiwaki, A. R. Uhl, S. Buecheler, and A. N. Tiwari, "Doping of polycrystalline CdTe for high-efficiency solar cells on flexible metal foil," *Nature Communications*, vol. 4, aug 2013.

[50] J. Perrenoud, L. Kranz, C. Gretener, F. Pianezzi, S. Nishiwaki, S. Buecheler, and A. N. Tiwari, "A comprehensive picture of Cu doping in CdTe solar cells," *Journal of Applied Physics*, vol. 114, p. 174505, nov 2013.

[51] D. Bätzner, A. Romeo, H. Zogg, R. Wendt, and A. Tiwari, "Development of efficient and stable back contacts on CdTe/CdS solar cells," *Thin Solid Films*, vol. 387, pp. 151–154, may 2001.

[52] J. Li, D. R. Diercks, T. R. Ohno, C. W. Warren, M. C. Lonergan, J. D. Beach, and C. A. Wolden, "Controlled activation of ZnTe:Cu contacted CdTe solar cells

using rapid thermal processing," *Solar Energy Materials and Solar Cells*, vol. 133, pp. 208–215, feb 2015.

[53] C. A. Wolden, A. Abbas, J. Li, D. R. Diercks, D. M. Meysing, T. R. Ohno, J. D. Beach, T. M. Barnes, and J. M. Walls, "The roles of ZnTe buffer layers on CdTe solar cell performance," *Solar Energy Materials and Solar Cells*, vol. 147, pp. 203–210, apr 2016.

[54] R. Sheer and H. W. Shock, "Thin Film Heterostructures," in *Chalcogenide Photovoltaics*, pp. 9–127, Weinheim, Germany: Wiley-VCH Verlag GmbH & Co. KGaA, feb 2011.

[55] T. Song, A. Kanevce, and J. R. Sites, "Emitter/absorber interface of CdTe solar cells," *Journal of Applied Physics*, vol. 119, p. 233104, jun 2016.

[56] S. Sharbati and J. R. Sites, "Impact of the Band Offset for n-Zn(O,S)/p-Cu(In,Ga)Se2 Solar Cells," *IEEE Journal of Photovoltaics*, vol. 4, pp. 697–702, mar 2014.

[57] R. Klenk, "Characterisation and modelling of chalcopyrite solar cells," *Thin Solid Films*, vol. 387, pp. 135–140, may 2001.

[58] T. Song, J. Tyler McGoffin, and J. R. Sites, "Interface-Barrier-Induced J–V Distortion of CIGS Cells With Sputtered-Deposited Zn(S,O) Window Layers," *IEEE Journal of Photovoltaics*, vol. 4, pp. 942–947, may 2014.

[59] a. O. Pudov, A. Kanevce, H. a. Al-Thani, J. R. Sites, and F. S. Hasoon, "Secondary barriers in CdS–CuIn1−xGaxSe2 solar cells," *Journal of Applied Physics*, vol. 97, p. 064901, mar 2005.

[60] J. Tauc, "Optical properties and electronic structure of amorphous Ge and Si," *Materials Research Bulletin*, vol. 3, pp. 37–46, jan 1968.

[61] C. Zhang, J. Zhang, Y. Hao, Z. Lin, and C. Zhu, "A simple and efficient solar cell parameter extraction method from a single current-voltage curve," *Journal of Applied Physics*, vol. 110, p. 064504, sep 2011.

[62] S. Chaisitsak, T. Sugiyama, A. Yamada, and M. Konagai, "Cu(InGa)Se 2 Thin-film Solar Cells with High Resistivity ZnO Buffer Layers Deposited by Atomic Layer Deposition," *Japanese Journal of Applied Physics*, vol. 38, pp. 4989–4992, sep 1999.

[63] L. Olsen, H. Aguilar, F. Addis, Wenhua Lei, and Jun Li, "CIS solar cells with ZnO buffer layers," in *Conference Record of the Twenty Fifth IEEE Photovoltaic Specialists Conference - 1996*, pp. 997–1000, IEEE, 1996.

[64] A. Hultqvist, C. Platzer Bjorkman, T. Torndahl, M. Ruth, and M. Edoff, "Optimization of i-ZnO window layers for Cu(In,Ga)Se2 solar cells with ALD buffers," in *Proceedings of the 22nd European Photovoltaic Solar Energy Conference*, (Milano), pp. 2381–2384, 2007.

[65] K. Lee, E.-A. Ok, J.-K. Park, W. M. Kim, Y.-J. Baik, D. Kim, and J.-h. Jeong, "The impact of oxygen incorporation during intrinsic ZnO sputtering on the performance of Cu(In,Ga)Se 2 thin film solar cells," *Applied Physics Letters*, vol. 105, p. 083906, aug 2014.

[66] K. Ellmer and A. Klein, "ZnO and Its Applications," in *Transparent Conductive Zinc Oxide*, pp. 1–33, Springer, 2008.

[67] Ü. Özgür, Y. I. Alivov, C. Liu, A. Teke, M. A. Reshchikov, S. Doğan, V. Avrutin, S.-J. Cho, and H. Morkoç, "A comprehensive review of ZnO materials and devices," *Journal of Applied Physics*, vol. 98, p. 041301, aug 2005.

[68] P. S. Kobyakov, J. M. Kephart, and W. S. Sampath, "Sublimation of Mg onto CdS/CdTe films fabricated by advanced deposition system," in *2011 37th IEEE Photovoltaic Specialists Conference*, no. August, pp. 002740–002745, IEEE, jun 2011.

[69] S. Mridha and D. Basak, "Effect of thickness on the structural, electrical and optical properties of ZnO films," *Materials Research Bulletin*, vol. 42, pp. 875–882, may 2007.

[70] W. Water and S.-Y. Chu, "Physical and structural properties of ZnO sputtered films," *Materials Letters*, vol. 55, pp. 67–72, jul 2002.

[71] G. A. Kumar, M. V. R. Reddy, and K. N. Reddy, "Structural and Optical properties of ZnO thin films grown on various substrates by RF magnetron sputtering," *IOP Conference Series: Materials Science and Engineering*, vol. 73, p. 012133, feb 2015.

[72] I. C. Noyan, T. C. Huang, and B. R. York, "Residual stress/strain analysis in thin films by X-ray diffraction," *Critical Reviews in Solid State and Materials Sciences*, vol. 20, pp. 125–177, jan 1995.

[73] J. H. Park, D. J. Byun, and J. K. Lee, "Electrical and optical properties of fluorine-doped tin oxide (SnOx:F) thin films deposited on PET by using ECR–MOCVD," *Journal of Electroceramics*, vol. 23, pp. 506–511, oct 2009.

[74] H. Mahabaduge, K. Wieland, C. Carter, V. Plotnikov, and D. Giolando, "Sputtered HRT layers for CdTe solar cells," in *2011 37th IEEE Photovoltaic Specialists Conference*, pp. 001302–001304, IEEE, jun 2011.

[75] M. Gloeckler, A. L. Fahrenbruch, and J. R. Sites, "Numerical modeling of cigs and cdte solar cells: setting the baseline," in *3rd World Conference onPhotovoltaic Energy Conversion, 2003. Proceedings of*, vol. 1, pp. 491–494 Vol.1, May 2003.

[76] J. Kephart, J. McCamy, Z. Ma, A. Ganjoo, F. Alamgir, and W. Sampath, "Band alignment of front contact layers for high-efficiency CdTe solar cells," *Solar Energy Materials and Solar Cells*, vol. 157, pp. 266–275, dec 2016.

[77] J. Sites and J. Pan, "Strategies to increase CdTe solar-cell voltage," *Thin Solid Films*, vol. 515, pp. 6099–6102, may 2007.

[78] M. Gloeckler and J. Sites, "Efficiency limitations for wide-band-gap chalcopyrite solar cells," *Thin Solid Films*, vol. 480-481, pp. 241–245, jun 2005.

[79] M. Ruckh, D. Schmid, and H. W. Schock, "Photoemission studies of the ZnO/CdS interface," *Journal of Applied Physics*, vol. 76, pp. 5945–5948, nov 1994.

[80] G. V. Rao, F. Säuberlich, and A. Klein, "Influence of Mg content on the band alignment at CdS/(Zn,Mg)O interfaces," *Applied Physics Letters*, vol. 87, p. 032101, jul 2005.

[81] R. Ondo-Ndong, G. Ferblantier, M. Al Kalfioui, A. Boyer, and A. Foucaran, "Properties of RF magnetron sputtered zinc oxide thin films," *Journal of Crystal Growth*, vol. 255, pp. 130–135, jul 2003.

[82] X. Zhang, H. Ma, Q. Wang, J. Ma, F. Zong, H. Xiao, F. Ji, and S. Hou, "Structural and optical properties of MgxZn1−xO thin films deposited by magnetron sputtering," *Physica B: Condensed Matter*, vol. 364, pp. 157–161, jul 2005.

[83] J.-H. Huang and C.-P. Liu, "The influence of magnesium and hydrogen introduction in sputtered zinc oxide thin films," *Thin Solid Films*, vol. 498, pp. 152–157, mar 2006.

[84] T. Minemoto, T. Negami, S. Nishiwaki, H. Takakura, and Y. Hamakawa, "Preparation of Zn1−xMgxO films by radio frequency magnetron sputtering," *Thin Solid Films*, vol. 372, pp. 173–176, sep 2000.

[85] A. Ohtomo, M. Kawasaki, I. Ohkubo, H. Koinuma, T. Yasuda, and Y. Segawa, "Structure and optical properties of ZnO/Mg0.2Zn0.8O superlattices," *Applied Physics Letters*, vol. 75, pp. 980–982, aug 1999.

[86] L. Cao, J. Jiang, and L. Zhu, "Realization of band-gap engineering of ZnO thin films via Ca alloying," *Materials Letters*, vol. 100, pp. 201–203, jun 2013.

[87] K. P. Misra, K. C. Dubey, R. K. Shukla, and A. Srivastava, "Reduction in carrier concentration by calcium doping in ZnO thin films," in *2009 International Conference on Emerging Trends in Electronic and Photonic Devices & Systems*, pp. 495–496, IEEE, dec 2009.

[88] T. Minemoto, Y. Hashimoto, T. Satoh, T. Negami, H. Takakura, and Y. Hamakawa, "Cu(In,Ga)Se2 solar cells with controlled conduction band offset of window/Cu(In,Ga)Se2 layers," *Journal of Applied Physics*, vol. 89, pp. 8327–8330, jun 2001.

[89] T. Minemoto, Y. Hashimoto, W. Shamskolahi, T. Satoh, T. Negami, H. Takakura, and Y. Hamakawa, "Control of conduction band offset in wide-gap Cu(In,Ga)Se solar cells," *Solar Energy Materials and Solar Cells*, vol. 75, pp. 121–126, jan 2003.

[90] G.-R. Uhm, S. Y. Jang, Y. H. Jeon, H. K. Yoon, and H. Seo, "Optimized electronic structure of a Cu(In,Ga)Se2 solar cell with atomic layer deposited Zn(O,S) buffer layer for high power conversion efficiency," *RSC Advances*, vol. 4, no. 53, p. 28111, 2014.

[91] N. Naghavi, D. Abou-Ras, N. Allsop, N. Barreau, S. Bücheler, A. Ennaoui, C.-H. Fischer, C. Guillen, D. Hariskos, J. Herrero, R. Klenk, K. Kushiya, D. Lincot, R. Menner, T. Nakada, C. Platzer-Björkman, S. Spiering, A. Tiwari, and T. Törndahl, "Buffer layers and transparent conducting oxides for chalcopyrite Cu(In,Ga)(S,Se)2 based thin film photovoltaics: present status and current developments," *Progress in Photovoltaics: Research and Applications*, vol. 18, pp. 411–433, sep 2010.

[92] T. Törndahl, C. Platzer-Björkman, J. Kessler, and M. Edoff, "Atomic layer deposition of Zn1−xMgxO buffer layers for Cu(In,Ga)Se2 solar cells," *Progress in Photovoltaics: Research and Applications*, vol. 15, pp. 225–235, may 2007.

[93] X. Li, A. Kanevce, J. V. Li, I. Repins, B. Egaas, and R. Noufi, "Impact of Zn1-xMnxO on Cu(In,Ga)Se2 Thin-Film Solar Cells," in *2009 34th IEEE Photovoltaic Specialists Conference (PVSC)*, pp. 000305–000308, IEEE, jun 2009.

[94] J. V. Li, X. Li, Y. Yan, C.-S. Jiang, W. K. Metzger, I. L. Repins, M. A. Contreras, and D. H. Levi, "Influence of sputtering a ZnMgO window layer on the interface and bulk properties of Cu(In,Ga)Se[sub 2] solar cells," *Journal of Vacuum Science & Technology B: Microelectronics and Nanometer Structures*, vol. 27, no. 6, p. 2384, 2009.

[95] J. V. Li, X. Li, A. Kanevce, Y. Yan, and I. Repins, "The effect of ZnO replacement by ZnMgO ON ZnO/CdS/Cu(In,Ga)Se2 solar cells," in *2009 34th IEEE Photovoltaic Specialists Conference (PVSC)*, pp. 000127–000130, IEEE, jun 2009.

[96] J. Perrenoud, S. Buecheler, L. Kranz, C. Fella, J. Skarp, and A. Tiwari, "Application Of ZnO1-xSx as Window Layer in Cadmium Telluride Solar Cells," in *2010 35th IEEE Photovoltaic Specialists Conference*, vol. 2, pp. 000995–001000, IEEE, jun 2010.

[97] D. M. Meysing, C. A. Wolden, M. M. Griffith, H. Mahabaduge, J. Pankow, M. O. Reese, J. M. Burst, W. L. Rance, and T. M. Barnes, "Properties of reactively sputtered oxygenated cadmium sulfide (CdS:O) and their impact on CdTe solar cell performance," *Journal of Vacuum Science & Technology A: Vacuum, Surfaces, and Films*, vol. 33, p. 021203, mar 2015.

[98] D. E. Swanson, S. R. Hafner, W. S. Sampath, and J. D. Williams, "Development of plasma enhanced closed space sublimation for the deposition of CdS:O in CdTe solar cells," in *2013 IEEE 39th Photovoltaic Specialists Conference (PVSC)*, pp. 0434–0437, IEEE, jun 2013.

[99] J. M. Kephart, R. Geisthardt, and W. Sampath, "Sputtered, oxygenated CdS window layers for higher current in CdS/CdTe thin film solar cells," in *2012 38th IEEE Photovoltaic Specialists Conference*, pp. 000854–000858, IEEE, jun 2012.

[100] D.-K. Hwang, M.-C. Jeong, and J.-M. Myoung, "Effects of deposition temperature on the properties of Zn1−xMgxO thin films," *Applied Surface Science*, vol. 225, pp. 217–222, mar 2004.

[101] R. E. Honig, "Vapor pressure data for the solid and liquid elements," *RCA Review*, vol. 23, no. 4, pp. 567–586, 1962.

[102] T. Makino, Y. Segawa, M. Kawasaki, A. Ohtomo, R. Shiroki, K. Tamura, T. Yasuda, and H. Koinuma, "Band gap engineering based on MgxZn1−xO and CdyZn1−yO ternary alloy films," *Applied Physics Letters*, vol. 78, pp. 1237–1239, feb 2001.

[103] F. Bittau, A. Abbas, K. Barth, J. Bowers, and J. Walls, "The effect of temperature on resistive ZnO layers and the performance of thin film CdTe solar cells," *Thin Solid Films*, vol. 633, pp. 92–96, jul 2017.

[104] T. Kirchartz, K. Ding, and U. Rau, "Fundamental Electrical Characterization of Thin-Film Solar Cells," in *Advanced Characterization Techniques for Thin Film Solar Cells*, pp. 33–60, Weinheim, Germany: Wiley-VCH Verlag GmbH & Co. KGaA, apr 2011.

[105] S. S. Hegedus and W. N. Shafarman, "Thin-film solar cells: device measurements and analysis," *Progress in Photovoltaics: Research and Applications*, vol. 12, pp. 155–176, mar 2004.

[106] "Thin Film Heterostructures," in *Chalcogenide Photovoltaics*, pp. 9–127, Weinheim, Germany: Wiley-VCH Verlag GmbH & Co. KGaA, feb 2011.

[107] S. Calnan, S. Neubert, C. Nock, O. Gabriel, M. Rohde, F. Ruske, B. Stannowski, and R. Schlatmann, "Detailed comparison of transparent front contacts for thin film silicon solar cells," in *2011 37th IEEE Photovoltaic Specialists Conference*, pp. 000579–000584, IEEE, jun 2011.

[108] J. H. Shi, S. M. Huang, J. B. Chu, H. B. Zhu, Z. a. Wang, X. D. Li, D. W. Zhang, Z. Sun, W. J. Cheng, F. Q. Huang, and X. J. Yin, "Effect of ZnO buffer layer on AZO film properties and photovoltaic applications," *Journal of Materials Science: Materials in Electronics*, vol. 21, pp. 1005–1013, dec 2009.

[109] M. Rubin, "Optical properties of soda lime silica glasses," *Solar Energy Materials*, vol. 12, pp. 275–288, sep 1985.

[110] S. Cornelius, M. Vinnichenko, N. Shevchenko, A. Rogozin, A. Kolitsch, and W. Möller, "Achieving high free electron mobility in ZnO:Al thin films grown by reactive pulsed magnetron sputtering," *Applied Physics Letters*, vol. 94, p. 042103, jan 2009.

[111] Z. Zhan, J. Zhang, Q. Zheng, D. Pan, J. Huang, F. Huang, and Z. Lin, "Strategy for Preparing Al-Doped ZnO Thin Film with High Mobility and High Stability," *Crystal Growth & Design*, vol. 11, pp. 21–25, jan 2011.

[112] J. Bowers, H. Upadhyaya, T. Nakada, and A. Tiwari, "Effects of surface treatments on high mobility ITiO coated glass substrates for dye sensitized solar cells and their tandem solar cell applications," *Solar Energy Materials and Solar Cells*, vol. 94, pp. 691–696, apr 2010.

[113] M. F. A. M. van Hest, M. S. Dabney, J. D. Perkins, D. S. Ginley, and M. P. Taylor, "Titanium-doped indium oxide: A high-mobility transparent conductor," *Applied Physics Letters*, vol. 87, p. 032111, jul 2005.

[114] W. Xia, H. Lin, H. N. Wu, C. W. Tang, I. Irfan, C. Wang, and Y. Gao, "Te/Cu bi-layer: A low-resistance back contact buffer for thin film CdS/CdTe solar cells," *Solar Energy Materials and Solar Cells*, vol. 128, pp. 411–420, sep 2014.

[115] T. Song, A. Moore, and J. R. Sites, "Te Layer to Reduce the CdTe Back-Contact Barrier," *IEEE Journal of Photovoltaics*, vol. 8, pp. 293–298, jan 2018.